

DESIGN AND IMPLEMENTATION OF AN INTERFACE CIRCUIT FOR
PIEZOELECTRIC ENERGY HARVESTERS

A THESIS SUBMITTED TO
THE GRADUATE SCHOOL OF NATURAL AND APPLIED SCIENCES
OF
MIDDLE EAST TECHNICAL UNIVERSITY

BY

SALAR CHAMANIAN

IN PARTIAL FULFILLMENT OF THE REQUIREMENTS
FOR
THE DEGREE OF DOCTOR OF PHILOSOPHY
IN
ELECTRICAL AND ELECTRONICS ENGINEERING

OCTOBER 2018

Approval of the thesis:

**DESIGN AND IMPLEMENTATION OF AN INTERFACE CIRCUIT FOR
PIEZOELECTRIC ENERGY HARVESTERS**

Submitted by **SALAR CHAMANIAN** in partial fulfillment of the requirements for the degree
of **Doctor of Philosophy in the Department of Electrical and Electronics Engineering,**
Middle East Technical University by,

Prof. Dr. Halil Kalıpçılar

Dean, Graduate School of **Natural and Applied Sciences**

Prof. Dr. Tolga Çiloğlu

Head of Department, **Electrical and Electronics Engineering**

Prof. Dr. Haluk Külâh

Supervisor, **Electrical and Electronics Eng. Dept., METU**

Assoc. Prof. Dr. Ali Muhtaroglu

Co-Supervisor, **Electrical and Electronics Eng. Dept., METU NCC**

Examining Committee Members:

Prof. Dr. Tayfun Akın

Electrical and Electronics Engineering Dept., METU

Prof. Dr. Haluk Külâh

Electrical and Electronics Engineering Dept., METU

Prof. Dr. Ali Ziya Alkar

Electrical and Electronics Engineering Dept., Hacettepe University

Dr. Öğr. Üyesi Serdar Kocaman

Electrical and Electronics Engineering Dept., METU

Dr. Öğr. üyesi Dinçer Gökçen

Electrical and Electronics Engineering Dept., Hacettepe University

Date: 31.10.2018

I hereby declare that all information in this document has been obtained and presented in accordance with academic rules and ethical conduct. I also declare that, as required by these rules and conduct, I have fully cited and referenced all material and results that are not original to this work.

Name, Last name : Salar Chamanian

Signature :

ABSTRACT

DESIGN AND IMPLEMENTATION OF AN INTERFACE CIRCUIT FOR PIEZOELECTRIC ENERGY HARVESTERS

Chamanian, Salar

Ph.D, Department of Electrical and Electronics Engineering

Supervisor: Prof. Dr. Haluk K lah

Co-Supervisor: Assoc. Prof. Dr. Ali Muhtarog lu

October 2018, 112 pages

Micro-fabricated piezoelectric transducer is a prominent harvesting method due to its small size and relatively high energy density. However, the available interface circuits (IC) in the literature for piezoelectric energy harvesters (PEH) are generally designed for macro-scaled versions having a power output in the range of hundreds μW . The efficiency of such systems is significantly diminished when input power drops to tens of μW s or less, which is the pertinent power output range for micro-fabricated devices. Therefore, it is necessary to develop efficient electronics to extract energy from low output power levels of Microelectromechanical systems (MEMS) piezoelectric energy harvesters. The main aim of this thesis is to develop ICs that can efficiently extract energy from the MEMS piezoelectric energy harvesters and charge storage element for powering up micro-electronic devices.

In the first IC, a novel multi-stage energy extraction method is proposed to optimize the implementation of the synchronous electrical charge extraction (SECE) converter. This optimization allows downsizing of the external inductor without affecting the power-conversion efficiency. Then, a charge management approach is presented to speed up the charging of the large storage element. The advantage of this method is that it accelerates the transition from passive mode to active mode. Several circuit techniques are introduced to enhance practicability of the energy harvesting IC. An autonomous system is achieved through a start-up circuit with power management

circuit that initiates the circuit from no primary charge. Implementations of active negative voltage converter and new ultra-low-power peak detector expand operating frequency range of the IC from 100 Hz to 4 kHz. Finally, self-adapting multi-stage energy extraction (MSEE) enhances power conversion efficiency for a wide input-power range. Maximum charging efficiency of 84 % is achieved with a 1 mH external inductor, while MEMS PEH is excited at 390 Hz.

Second IC introduces a novel nonlinear switching technique aiming to boost extracted energy from low coupling factor PEHs and provide load-independent energy extraction with a single inductor. The idea is to enhance effective damping force of the PEH by processing piezoelectric voltage through a set of switches and an inductor. A novel maximum power point (MPP) sensing approach is proposed to achieve the optimal operation point of the proposed circuit regardless of input excitation level, for the first time in literature. The IC can efficiently harvest energy from shock vibrations, as MPP circuit adjusts optimal point regardless of the variation in the available energy on PEH.

In the end, an efficient hybrid energy-harvesting interface is presented to simultaneously scavenge power from electromagnetic and piezoelectric sources, while driving a single load. The total simultaneously extracted power from both harvesters is more than the power obtained from each independently. The hybrid IC reaches up to 90% conversion efficiency with output power level of 100 μ W. A wearable harvesting prototype consisting of custom-made electromagnetic harvester, off-the-shelf PEH, and the proposed interface circuit is built and tested to harvest energy from body movement.

Keywords: Interface circuit, Piezoelectric energy harvester, MEMS, Self-adapting, Maximum power point, Hybrid IC.

ÖZ

PIEZOELEKTRİK ENERJİ ÜRETEÇLERİ İÇİN ARAYÜZ DEVRESİ TASARIMI VE UYGULAMASI

Chamanian, Salar
Doktora, Elektrik ve Elektronik Mühendisliği Bölümü
Tez Yöneticisi: Prof. Dr. Haluk Külah
Ortak Tez Yöneticisi: Doç. Dr. Ali Muhtaroglu

Ekim 2018, 112 sayfa

Mikro düzeyde üretilmiş piezoelektrik enerji üreteçleri, küçük boyutlu olmaları ve yüksek enerji yoğunluğuna sahip olmalarından dolayı enerji üreteçleri arasında ön plana çıkmaktadır. Fakat piezoelektrik üreteçler için literatürde bulunan mevcut ara yüz devreleri genellikle çıkış güçleri yüzlerce μW civarlarında olan büyük ölçekli modelleri için dizayn edilmiştir. Bu tarz sistemlerin verimlilikleri girişlerindeki güç seviyesi onlarca μW ve daha az olduğu zaman önemli ölçüde etkilenirler ki bu durum mikro düzeydeki cihazlarda çoğunlukla gözlemlenmektedir. Bu nedenle, düşük güç girişlerinden enerji sağlayan sistemler için yüksek verimli ara yüz devreleri geliştirilmelidir. Bu tezin amacı, biyolojik mikro elektronik devreler için, MEMS enerji üreteçlerinden enerji sağlayan ve regüle edilmiş DC voltaj sağlayan bir ara yüz devresi geliştirmektir.

Birinci arayüz devresinde (IC), SECE çeviricilerin optimum uygulaması için yeni bir çok-aşamalı enerji çıkarım yöntemi önerilmiştir. Bu optimizasyon güç verimliliğini etkilemeden harici bobinin değerinin düşürülmesini almaktadır. Sonrasında, yüksek kapasiteli depolama elemanını daha hızlı şarj etmek için yeni bir yük yönetim yaklaşımı sunulmuştur. Bu metodu avantajı pasif şarjdan aktif şarja hızlı bir geçiş sağlamasıdır. Devrenin enerji üreteçlerindeki pratik kullanımını artırmak için farklı devre teknikleri uygulanmıştır. Sonuç olarak başlangıç (start-up) devresi ve PMC ile başlangıçta hiç yük olmadığı durumda da çalışabilen otonom bir devre elde edilmiştir.

Aktif NVC ve yeni ultra-düşük güçlü tepe noktası belirleyici devre ile devrenin çalışma frekansının 100 Hz ile 4 kHz arasında gibi geniş bir bantta olması sağlanmıştır. Son olarak, kendinden adaptif MSEE tekniği geniş aralıktaki giriş gücü seviyeleri için güç verimliliğini artırmıştır. 1 mH harici bobin ve 390 Hz’te uyarılan MEMS PEH için %84 maksimum şarj verimliliği elde edilmiştir.

Tasarlanan ikinci arayüz devresi düşük kuplaj faktörlü PEH’lerden enerji çıkarımını artıracak yeni bir doğrusal olmayan anahtarlama tekniği önermektedir. Ayrıca, bu devre tek bobin ile yükten bağımsız enerji çıkarımı sağlamaktadır. Bu tekniğin arkasında yatan temel fikir, piezoelektrik voltajı birtakım anahtarlar ve bobin ile işleyerek PEH üzerindeki efektif sönümleme kuvvetini yükseltmektir. Literatürde ilk kez, giriş uyarım seviyesinden bağımsız olarak çalışan ve maksimum güç noktası (MPP) belirleme yöntemini kullanan yeni bir devre önerilmiştir. Arayüz devresi MPP sayesinde optimum noktayı bulabilmesi sayesinde şok titreşimlerde de verimli bir şekilde enerji üretebilmektedir.

Son olarak, elektromanyetik ve piezoelektrik kaynaklardan aynı anda güç çekip tek bir yüke iletebilen verimli bir hibrit enerji üretici devresi sunulmuştur. Hibrit sistemden çıkan toplan güç, ayrı ayrı enerji üretici kaynaklarının toplamından çıkan güçten daha fazladır. Hibrit arayüz devresi çıkış güç seviyesi 100 μ W seviyesinde iken %90 güç verimliliğine ulaşmaktadır. İnsan vücudu hareketlerinden enerji üretmek için hibrit elektromanyetik ve piezoelektrik enerji üreticileri ve arayüz elektroniğinden oluşan giyilebilir bir prototip tasarlanmış ve test edilmiştir.

Anahtar Sözcükler: Arayüz devresi, Piezoelektrik enerji üreticileri, MEMS, Kendinden adaptif, maksimum güç noktası, Hibrit arayüz devresi.

To my mother, father, sisters and my wife

ACKNOWLEDGMENTS

I would first like to express my sincere gratitude to my advisor Prof. Dr. Haluk K lah for his endless support towards realizing my goal of becoming an innovative and capable research and development engineer. Without his limitless wisdom, sincere understanding and extensive guidance, I could not successfully accomplish my academic journey.

I would like to thank my Co-Supervisor, Assoc. Prof. Dr. Ali Muhtarog lu for his invaluable help and support during this project. His comments and guidelines during the IC design phase were important in realizing this work.

I would also like to thank to Hasan Ulu an to accompany me in our challenging studies. I would like to thank to Dr.  zge Zorlu who has never hesitated to offer a hand whenever I needed.

BioMEMS research group has provided me unique abilities to improve myself, but most importantly, it allowed me to be a part of a great family. For this reason and for many more, I would like to thank to Bedirhan  lik, Aziz Koyuncuo lu,  zgen La ın, Parinaz Ahsrafi, Mustafa Kangul, Kaan Sel, Metin D ndar  zkan, Eren Aydın, Furkan G k e, Beg m  en Do an, Ya mur Demircan, Taylan Berkin T ral, G rhan  zkayar, Berat Y ksel, Berkay  ift i, and Akin Mert Yilmaz.

It takes a multidisciplinary background, a diverse skill set and of course hard work in order to design and implement a state-of-the-art system. However, it would have been impossible, without the support from the ones who were always there for me. In this manner, I would like express my very profound gratitude to my parents Vida and Darioush Chamanian and my sisters Sevda and Sogand and my love & wife Pardis for keeping their unfailing support and continuous encouragement all the time.

TABLE OF CONTENTS

ABSTRACT.....	v
ÖZ	vii
ACKNOWLEDGMENTS.....	x
TABLE OF CONTENTS	xi
LIST OF TABLES	xiv
LIST OF FIGURES	xv
CHAPTERS	
1 INTRODUCTION	1
1.1 Energy Harvesting Foundation.....	2
1.2 Piezoelectric Energy Harvester	4
1.2.1 Applications	7
1.2.2 Piezoelectric Electrical Model	10
1.3 Overview of Interface Circuits for PEH.....	12
1.3.1 Standard Rectifiers	12
1.3.2 Nonlinear Switching Techniques	14
1.4 Aim of This Study and Thesis Organization	18
2 IC FOR PEHS DESIGN I: MULTISTAGE ENERGY EXTRACTION BASED ON SECE TECHNIQUE	21
2.1 Interface Circuit Design	22
2.2 Multi-stage Process	23
2.2.1 Power Analysis	25

2.2.2	Power Optimization.....	27
2.3	Power Managing Process.....	28
2.4	Implementation of the Proposed Circuit.....	30
2.4.1	Trigger Circuit.....	31
2.4.2	Control Unit.....	33
2.4.3	PMC	37
2.5	Experimental Results.....	39
2.5.2	External Inductor.....	45
2.5.3	PMC Performance	46
2.5.4	Frequency Limitation	48
2.5.5	Discussion	50
3	IC FOR PEHS DESIGN II: SELF-ADAPTING OPTIMAL DSSH.....	53
3.1	Self-adapting DSSH IC	53
3.1.1	Concept and Operation Principle	53
3.1.2	Optimal Energy Transfer with Constant Vibration Magnitude.....	57
3.2	Circuit Implementation.....	58
3.2.1	Peak Detectors.....	59
3.2.2	Charge Flipping Sensor	60
3.2.3	Extraction Time Generator.....	62
3.2.4	Charge Depletion Detector.....	62
3.2.5	MPPT Circuit	63
3.3	Design Validation	65
3.4	Performance Comparison with MEMS Harvester.....	72
3.5	Discussion.....	74
4	HYBRID IC FOR PEHS AND ELECTROMAGNETIC HARVESTERS	77

4.1	Hybrid System Architecture	78
4.1.1	Proposed System and Operation Principle	78
4.1.2	Electromagnetic Harvesting IC	79
4.1.3	Piezoelectric Harvesting IC and Investment Time Manager	81
4.2	Design Validation	84
4.3	Wearable Energy Harvesting System	88
4.4	Discussion	92
5	CONCLUSION AND FUTURE WORK	95
5.1	Overview and Major Achievements	95
5.1.1	MSEE IC	95
5.1.2	Optimal DSSH IC	96
5.1.3	Hybrid Energy Harvesting System	97
5.2	Future Work	98
	REFERENCES	101
	CURRICULUM VITAE	111

LIST OF TABLES

TABLES

Table 2.1. Features of the external inductors.	45
Table 2.2. Comparison of implemented IC with Other SECE Circuits.	51
Table 3.1 Comparison of DSSH IC with state-of-the-art.	75
Table 4.1 Comparison of hybrid IC with state-of-the-art.	93

LIST OF FIGURES

FIGURES

Figure 1.1. (a) Intrinsic piezoelectric effect in PZT and (b) polarized piezoelectric material.....	5
Figure 1.2. Piezoelectric energy harvester schematic; a fixed-free cantilever with tip mass.....	6
Figure 1.3. A vibration energy harvesting WSN for sensing ambient parameters.	7
Figure 1.4. Location of umbo and LDV measurement axes.	9
Figure 1.5. LDV (laser Doppler vibrometer) measurements of umbo acceleration vs. frequency before and after incus detachment at 80 SPL and 100 SPL [31]	9
Figure 1.6. Equivalent network model for piezoelectric energy harvester.	11
Figure 1.7. Simple piezoelectric electrical model used in circuit design simulations.	11
Figure 1.8. Standard full bridge rectifier.....	12
Figure 1.9. Cockroft-Walton Voltage doubler IC.	12
Figure 1.10. Circuit diagram of SECE converter implemented in (a) buck-boost and (b) fly-back topologies.	15
Figure 1.11. Circuit diagram of integrated implementation of SECE converter [43].	16
Figure 1.12. Equivalent circuit of series-SSHI converter.	16
Figure 1.13. Equivalent circuit of SSHI MR converter [49].....	17
Figure 1.14. Equivalent circuit of enhanced SSHI converter [50].....	18
Figure 2.1. The overview of proposed energy harvesting IC.....	22
Figure 2.2. (a) Switch network and (b) extraction phases with corresponding state of the switches.	23
Figure 2.3. Extraction phases and critical switching points of the SECE in time domain for single and two-stage transfers.	24
Figure 2.4. Total power losses vs. power switch sizes @ $V_{OC,pp}=1.5$ V simulated in MATLAB.....	28

Figure 2.5. Total power loss vs. number of stages @ $V_{OC,pp}=12$ V simulated in MATLAB.	28
Figure 2.6. (a) Schematic of proposed circuit for charge management circuit and (b) operation principle.....	29
Figure 2.7. Schematic of autonomous multi-stage energy extraction circuit.....	30
Figure 2.8. Circuit diagram of NVC and S_1 switch.....	31
Figure 2.9. Schematics of the trigger circuit.	32
Figure 2.10. Measured voltage waveforms of the Start-up circuit.	32
Figure 2.11. Schematic of the implemented Peak Detector.	34
Figure 2.12. Simulated Voltage and current waveforms of the peak detector.	34
Figure 2.13. (a) Implemented Multi-stage generator: (b) Operation principle and related signals.	36
Figure 2.14. Implementation of N generator.....	37
Figure 2.15. Charge depletion detector.	38
Figure 2.16. Power management circuit for directing energy flow.	38
Figure 2.17. Test setup for experiments, based on an IC, test board, and MEMS piezoelectric energy harvester.	39
Figure 2.18. Measured input-output waveforms during multi-stage extraction ($N=3$) with highlighted periods for passive and active charging.	41
Figure 2.19. Experimental piezoelectric voltage and inductor current waveforms using the multi-stage method: (a) Single stage, (b) two stages, (c) three stages, (d) four stages.	41
Figure 2.20. Experimental output power vs. output DC storage voltage for four values of V_{OC} with single stage extraction.	42
Figure 2.21. Experimental output power @ $V_{OC,pp} = 1.5$ V for four different staging configurations vs. output DC storage voltage.	43
Figure 2.22. Experimental output power @ $V_{OC,pp} = 3.5$ V for four different staging configurations vs. output DC storage voltage.	43
Figure 2.23. Experimental charging efficiency of the IC for four different staging configurations vs. peak-to-peak piezoelectric O.C. voltage.....	44

Figure 2.24. Experimental charging efficiency of the IC with automatic stage adjustment vs. peak-to-peak piezoelectric O.C. voltage.	44
Figure 2.25. Measured conversion efficiency of the MSEE IC and the SECE vs. inductance.	46
Figure 2.26. Measured storage and output voltages at $V_{OC,pp}=3.5$ V with PMC.	47
Figure 2.27. Experimentally comparison of charging of output capacitance $C_{OUT}=47$ μ F with PMC and standard SECE operation excited with $V_{OC,pp}=3.5$ V.	47
Figure 2.28. Measured input and output waveforms of the peak detector for (a) 500 Hz, (b) 1 kHz, and (c) 4 KHz input frequencies.	48
Figure 2.29. The measured accuracy of the peak detector vs. input excitation frequency with 1.5 V and 4.5 V input peak voltages.	49
Figure 2.30. Chip efficiency vs. excitation frequency at $V_{OC,pp}=4$ V.	50
Figure 3.1. (a) RLC resonant circuit established in charge flipping, (b) capacitor voltage	54
Figure 3.2. Schematic of proposed circuit.	55
Figure 3.3. (a) Representing voltage and current waveforms corresponding to (b) operation phases of the proposed switching circuits.	56
Figure 3.4. Implementation of proposed optimal SSHI-SE IC.	59
Figure 3.5. Schematic of the implemented Peak Detector.	60
Figure 3.6. Schematic of (a) negative charge flipping sensor, and (b) positive charge flipping sensor.	61
Figure 3.7. Simulated current and voltage waveforms of negative charge flipping sensor	62
Figure 3.8. Schematic of implemented extraction time generator.	63
Figure 3.9. (a) MPPT circuit and corresponding (b) digital and (c) simulated analog signal waveforms.	65
Figure 3.10. (a) Experimental setup, (b) evaluation board, and (c).die micrograph. .	66
Figure 3.11. Measured piezoelectric voltage and inductor current waveforms for (a) steady state operation of SA_SSH IC (b) close up of charge flipping instants, (c) close up of charge extraction and recycling instants.	67
Figure 3.12. Measured waveforms of Optimum power point detection.	68

Figure 3.13. Measured charge of storage capacitance with $V_{OC,pp}=2$ V across charge extraction time (a) $\tau_{ex}=4.54$ μ s (b) $\tau_{ex,opt}=5.47$ μ s (c) $\tau_{ex}=6.32$ μ s ($C_{stor}=1$ μ F, $R_L=10$ M Ω).	69
Figure 3.14. Measured output power vs. output DC storage voltage for $V_{OC,pp}=2.24$ V and $V_{OC,pp}=5.9$ V.	70
Figure 3.15. Measured end-to-end power conversion efficiency of proposed IC.	70
Figure 3.16. Measured harvested power by proposed IC compared from 103YB PEH to ideal full bridge rectifier at different excitation levels.	71
Figure 3.17. Measured waveforms of proposed IC in response to shock excitations.	72
Figure 3.18. Measured harvested power by proposed IC from MEMS PEH compared to ideal full bridge rectifier at different excitation levels.	73
Figure 3.19. Setup to measure extracted power by the DSSH chip, MSEE chip, and on-chip FWR from MEMS PEH.	73
Figure 3.20. Measured power comparison of DSSH, MSEE, and full-wave rectifier at different open-circuit piezoelectric voltage.	74
Figure 4.1. System architecture of the vibration-based hybrid harvester interface.	79
Figure 4.2. Self-powered electromagnetic harvesting IC for low frequency vibrations.	80
Figure 4.3. Schematic of PEH IC and investment time manager.	81
Figure 4.4. Schematic of (a) the proposed negative voltage converter (NVC), (b) the comparator utilized inside NVC structure.	82
Figure 4.5. Summary of operation phases for piezoelectric energy harvesting IC and investment time manager.	83
Figure 4.6. Schematic of the adjustable pulse generator.	84
Figure 4.7. Die micrograph of the implemented hybrid IC fabricated in 0.18 μ m HV CMOS technology.	85
Figure 4.8. Test setup for hybrid energy harvesting IC.	85
Figure 4.9. Measured waveforms of the hybrid harvesting interface operation with generated control signals PD, ZCD, and RCD.	86
Figure 4.10. Measured charge profile of a 1 μ F load capacitor for different outputs of electromagnetic harvesting IC.	87

Figure 4.11. Extracted power vs. peak-to-peak piezoelectric open circuit voltage for high frequency excitations.	87
Figure 4.12. Experimental power conversion efficiency vs. peak-to-peak piezoelectric open circuit voltage for high frequency excitations.	88
Figure 4.13. Schematic of hybrid energy harvester prototype consisting of a PEH (V22BL from MIDE Company) and custom-made EMH.	89
Figure 4.14. (a) Fabricated prototype of hybrid energy harvester, and (b) its protective shelf with flexible wristband adapted for daily usage of the system. (c) Hybrid energy harvester system placed on the wrist of a jogger.	90
Figure 4.15. Measured waveforms of V_{EM} and $V_{BUF,EM}$ with hybrid system operation during jogging.	91
Figure 4.16. Measured waveforms of V_{PZT} and V_{STOR} with hybrid system operation during jogging.	91
Figure 4.17. Experimental extracted power at various loading conditions for excitations during jogging.	92

CHAPTER 1

INTRODUCTION

Miniaturization in microelectronic systems, such as wireless and implantable sensors, demands increasingly stringent battery size provisions. Such systems contrarily require large energy sources for prolonged operation with low maintenance in order to achieve low cost. Although low-power design techniques prolong the operation of such microelectronics devices, size-limited batteries utilized to supply power to the transducers constrain their lifetimes. Battery volume does not diminish at the same rate as the transducer electronics, and thus form the bulk of the system [1]. Besides, replacement and maintenance of these batteries can be costly and practically unattainable due to the location of the transducer or increasingly large number of sensor nodes. Hence, microelectronics start making use of energy harvesting systems to achieve reliable operation over long periods, and reduce system costs. Micro-scaled devices have a remarkable contribution in the health industry recently. Heart rate monitors, pacemakers, and neural stimulators together represent a broad subset of bio-electronic devices that provide continuous diagnostics and therapy. One of the most trend topics is middle ear applications of microsystems. More than 120,000 patients worldwide are using cochlear implants [2] which are utilized for treatment of severe-to-profound hearing loss [3]. A large storage element is particularly required for powering up these devices to avoid frequent charging or replacement [4]. While the anatomy of both human and animals (for study cases) constrains the size of the battery. The issues associated with maintenance costs, limitations of battery capacity and recycling of batteries can be alleviated by extracting some portion or entire of the required electrical energy from ambient energy sources by means of energy harvesting techniques [5]. Most of implementable harvesting transducers can provide tens of nW up to tens of μ W of output power. The harvested energy requires not only converting to usable form but also needs an additional process that can extract maximum available energy from out of the harvesters. This is essential due to often low voltage and low

power output of the energy harvesting elements. The CI devices rely on some form of battery power for operation.

This thesis looks into interface circuits (ICs) specific to piezoelectric energy harvesters, which are potential solution to power microdevices. The IC is employed to process and extract alternating signal across the piezoelectric energy harvester and manage the harvested power. This chapter represents literature survey on vibration-based energy harvesting principles and interface electronics with focus on piezoelectric energy harvesting systems.

1.1 Energy Harvesting Foundation

A 1cm^3 non-rechargeable lithium battery with typical energy storage capacity of 2800J can supply $100\text{ }\mu\text{W}$ of power for 1 year [6]. However even this high energy density battery is not sufficient for long-term operation where battery replacement is not an easy option. One of the main challenges in designing portable electronic devices is the battery technology due to either size or cost. Large size of the batteries in comparison with micro-scale devices and battery maintenance are limiting factors due to device placement. Therefore, exploring ambient energy sources and power generation approaches become more important for portable electronic devices as an alternative power source.

Energy harvesters exploit environmental energy sources such as heat, sunlight, RF signals, or vibration, and convert them to electrical energy. Temperature gradients available in the neighborhood of a sensor can be used to harvest excess heat through thermoelectric (TE) conversion. However, the output of a thermoelectric generator has a low voltage range, up to a few hundreds of millivolts, and low power density of $10\text{ }\mu\text{W}/\text{cm}^3$ under 30°C gradients [7], which is far below energy requirements of the sensors. Solar energy harvesters are more interesting in outdoor applications due to the availability of sunlight [8]. However, the generated energy level scales with the size of the solar panel, and the efficiency is drastically affected if indoor operation is required [9]. In RF power harvesters, the challenge is the efficient design of the IC with the very limited RF power in the environment [10], [11]. Hence, RF energy

harvesting is mostly useful if there exists an RF power base station nearby or for powering ultra-low power wireless architectures where the node operates with a very low duty-cycle. Among the mentioned ambient energy sources, vibration is particularly attractive as it is easily available as in vehicle motions, human movements, acoustic noise and seismic vibrations that vary in frequency and amplitude. These vibrations are harvested by using different energy conversion methods such as electrostatic, electromagnetic and piezoelectric transduction.

- **The electrostatic conversion** is achieved through the capacitance variation of pre-charged variable capacitors in response to external vibration. Mechanical structure of the electrostatic harvesters includes usually inertial mass and supporting legs associated with comb fingers, which are used to obtain large capacitance value. Separate pre-charge source is required in this technique to initiate harvesting process as the conductors of the capacitor are displaced relative to each other. Sterken et al. [12] introduced electret-based electrostatic harvesters by use of an electret (permanently polarized dielectric) as a primary polarization that eliminated external charge source requirement. Experimental results show that harvesting power strongly depends on primary polarization source. The electrostatic energy harvesters are more suitable for small scaled devices due to full compatibility with MEMS technology and CMOS process. Displacement limitation, mechanical stop and initial polarization requirements and high impact of parasitic capacitances are the problems related with this harvesting technique. Moreover, high output impedance and relative low power density of this method restrict usage of this method.
- **Electromagnetic scavengers** employ electromagnetic induction, arising from the relative motion between a permanent magnet and a conductor. The Faraday's law of electromagnetic induction states that change of magnetic fields enclosed by coil wound induces an electrical current on the coil wound. The generated output power depends strongly on magnetic flux changes and input vibration frequency. The flux change is firmly relative with the size and magnet properties. Although electromagnetic harvesters show high efficiencies

in macro scale, low output voltage of micro-scaled electromagnetic harvester makes implementation of energy harvesting system more challenging. Furthermore, micro-scaled electromagnetic harvesters are difficult to integrate with MEMS technology and magnetic flux dramatically diminishes with miniaturizing magnet size.

- In **piezoelectric energy harvesters**, an electrical charge is produced across piezoelectric material when imposed to mechanical stress, which is so-called direct piezoelectric effect. This stress is generally generated through deformation of a base-structure that piezoelectric material is mounted on. Among these methods, piezoelectric conversion is advantageous to energy harvesting devices due to the relatively high energy density of piezoelectric materials, and ease of integration [13], [14]. Thus, the following sections are devoted to piezoelectric harvesters, related applications, modeling, and front-end interface circuits in more detail.

1.2 Piezoelectric Energy Harvester

The direct piezoelectric effect arise from asymmetry of the certain solid material like crystals and ceramics. The piezoelectric effect can be illustrated by means of Figure 1.1. Indeed, below Curie temperature, crystallite forms asymmetric charge arrangement leading to random orientation of electric dipoles. Polarization of the piezoelectric material under a strong electric field aligns the groups of dipoles, resulting in exhibition of piezoelectric characteristics. Lead zirconate titanate (PZT) is the most commonly used piezoelectric material, nowadays.

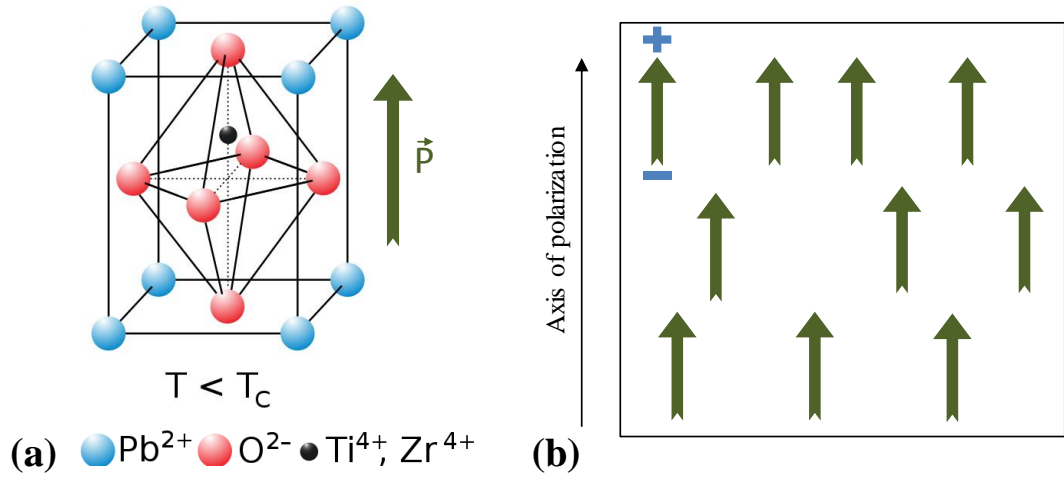


Figure 1.1. (a) Intrinsic piezoelectric effect in PZT and (b) polarized piezoelectric material.

The piezoelectric harvesters can be applied in different harvesting configurations and geometries [15], [16]. The most prevalent configuration is cantilever beam since it is very compliant structure that can be implemented with MEMS technology. Figure 1.2 shows a typical piezoelectric energy harvester structure. Piezoelectric energy harvesters use a cantilever beam with or without a proof mass to tune to lower resonance frequencies and higher resonance frequencies, respectively. Usually a piezoelectric layer is bonded around the fixed side of the beam. The harvester is generally mounted on vibrating sections and mechanical coupling transfers these vibrations to the harvester. Thus, base excitation forces the beam to vibrate. The bending of the beam results in alternating tensile and compressive stresses on the piezoelectric layer. Then, depending on the amplitude of the stress, an oscillating (AC) voltage output is generated across the piezoelectric layer.

An analytical analysis conducted by Roundy [17] has illustrated that the output power of piezoelectric generator depends on the system coupling coefficient (κ), the quality factor of the device (Q), the density of the generator, and transmission coefficient of the electrical load. At the end, the maximum power that can be extracted from piezoelectric energy harvester has been obtained as follow:

$$P_{\max} = \frac{\kappa^2 M (QA)^2}{4\omega} \quad (1.1)$$

where ω and A are exciting frequency and acceleration, respectively. It is necessary to maximize coupling coefficient, as well as the mass of the device to achieve higher power conversion. As a case in point, Aktakka [18] has developed a micro-scale piezoelectric energy harvester by using bulk piezoceramics. The advantage of bulk piezoceramics is its higher piezoelectric coupling coefficient with respect to other materials. However, the integration of bulk piezoceramics into standard MEMS fabrication processes is not trivial. The relationship between the power and resonance frequency depends on both excitation and device conditions. If the excitation is set to a level that at a resulting mass acceleration (QA) is constant, then, the power is inversely proportional to resonance frequency. If the excitation is set to a level that at a resulting mass displacement is constant, then the power is proportional to the third power of the resonance frequency.

Ultimately, the AC output power of piezoelectric harvesters depends on piezoelectric characteristics and the vibration level. The output impedance of piezoelectric energy harvesters is capacitive and is relatively high ($\sim 200 \text{ k}\Omega - 10 \text{ M}\Omega$) that impedes efficient power transfer with the conventional AC/DC conversion techniques. Therefore, there are significant challenges in designing efficient front-end interfaces or rectifying the output of the piezoelectric harvesters.

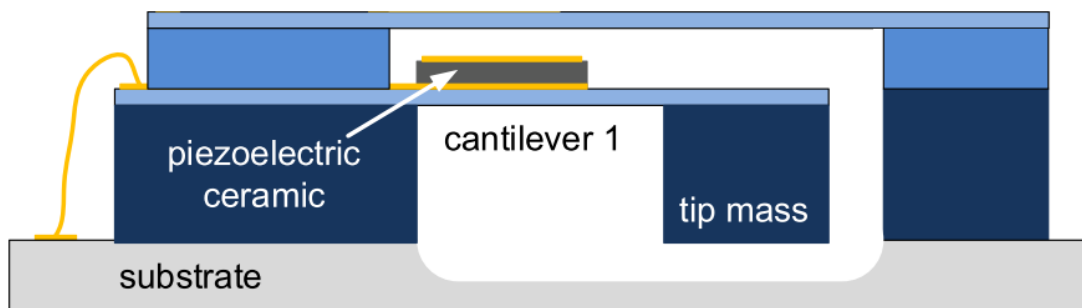


Figure 1.2. Piezoelectric energy harvester schematic; a fixed-free cantilever with tip mass.

1.2.1 Applications

1.2.1.1 Powering of Wireless Sensor Networks

A Wireless Sensor Network (WSN) is defined as a set of wireless communication units, which are equipped with various sensors organized into a cooperative network. Sensor networks are widely used in a range of different applications such as security, military, and environmental monitoring [19], [20]. These gadgets are also used in many civilian applications, such as habitat monitoring, healthcare applications, home automation and traffic control [21], [22], [23]. The development of WSN technologies enabled target detection, identification and tracking in a large scale of monitoring zones [24]. Managing the power consumption of a node in a WSN is an essential step to prop-up a reliable network. Energy is generally known as a main obstacle for battery-powered devices and embedded sensor nodes. In designing a battery-powered WSN, energy limitation has always been addressed as a crucial issue. Powering up the nodes of a WSN with energy harvesters is an evolving technology in such applications [25]. In this context, vibration is considered as a perpetual energy source for WSNs due to its affluence and availability [26]. A typical vibration energy harvesting WSN is depicted in Figure 1.3. The piezoelectric transducer is one of the most preferable harvesting method, considering its various types and the operating frequency range, to extract vibrational energy for providing whole or portion of the required energy of the WSN [13].

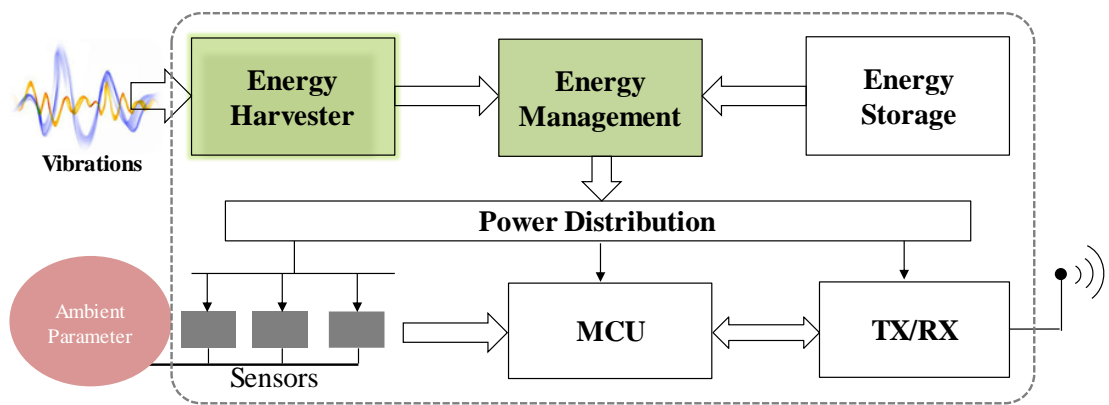


Figure 1.3. A vibration energy harvesting WSN for sensing ambient parameters.

1.2.1.2 Powering of Cochlear implant

Cochlear implants (CI) have been using for the treatment of sensorineural hearing loss. CIs use electronics to directly stimulate the auditory nerve fibers, thus bypassing the damaged hair cells in the cochlea. In recent decade, studies about the cochlear implants are mainly focused on making CIs fully implantable. A Fully implanted cochlear implant (FICI) has three main requirements that are distinct from a conventional CI. First, a FICI that is completely untethered (i.e., without a coil that continuously provides power) requires an implanted battery that is rechargeable because of the volume and power consumption constraints of the FICI, as well as the need to avoid future surgeries for battery replacement. The number of charges per day must also be limited to once or twice a day to minimize user impact.

Investigating various energy harvesting methods to power CIs have been elaborate with the lower power-requirements of the FICI systems. One recent study by Mercier et al. [27] has suggested using intra-cochlear potential for energy extraction for powering biological sensors. Maximum output power measured from a guinea pig was 1.12 nW during 5 hour experiment. Mukherjee et al [28] investigated the possible use of piezoelectric materials in the cochlea as the charge generating device. They conducted preliminary in vivo tests on guinea pigs with limited success. Inaoka et al [29] place small piezoelectric device on the basilar membrane in cochlea of a guinea pig as a transducer. The measured results illustrate that the output voltage is not enough for direct stimulation of the auditory nerves and requires amplification in the order of thousands. Placing the piezoelectric materials inside cochlea to generate voltage from the traveling wave inside the cochlear fluid has not been very successful for stimulating the auditory nerves. The vibration characteristics of the tympanic membrane have been investigated in [30], [31] to attach the transducer. Vibration of umbo has been measured by a laser doppler vibrometer (LDV) at different sound pressures and frequencies as shown in Figure 1.4. Figure 1.5 shows the acceleration results for 80 and 100 dB SPL from four cadaveric ears with and without incus (the second ossicles bone). In many cochlear implant operations, incus is removed to open space in the middle ear cavity. Removal of incus increased the tympanic membrane acceleration up to three times, depending on the vibration frequency.

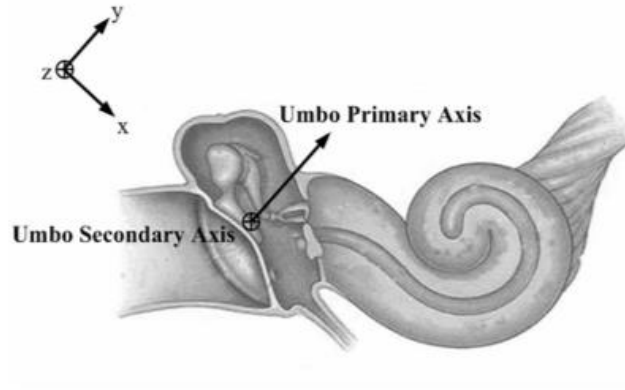


Figure 1.4. Location of umbo and LDV measurement axes.

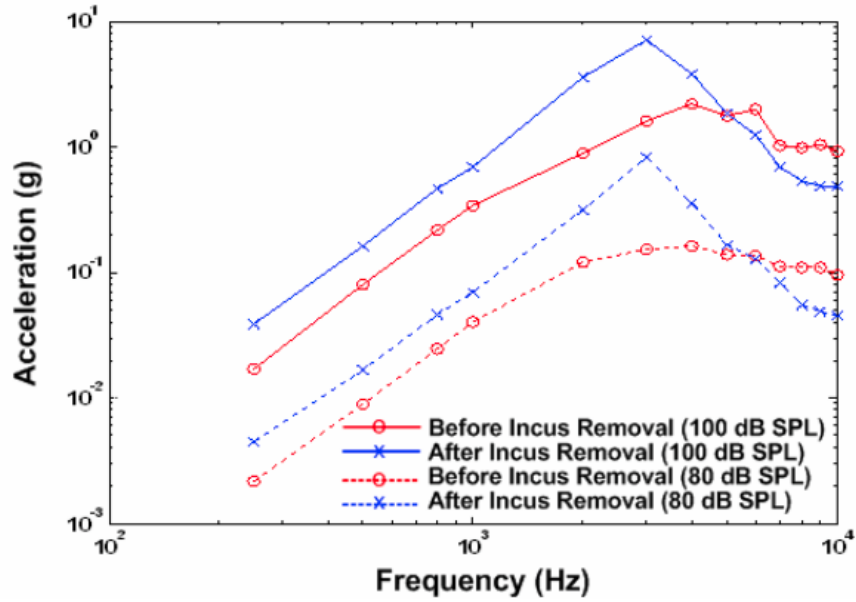


Figure 1.5. LDV (laser Doppler vibrometer) measurements of umbo acceleration vs. frequency before and after incus detachment at 80 SPL and 100 SPL [31] .

In a previous study of our group, an alternative energy harvesting method was suggested [32] using a unimorph cantilever piezoelectric energy harvesters placed on eardrum. The harvester was fabricated and tested on a shaker table. In this study, piezoelectric energy harvester is considered and investigated as a solution for CI power requirements under different acoustic signal strengths. The generated rms output power was measured for several excitation levels and the piezoelectric maximum power of around $1\mu\text{W}$ and $100\mu\text{W}$ are obtained under 0.1 g and 1.6g accelerations, respectively. The cochlear implant device presented by Yip et al. [33] dissipates 55

μW power for processing the sound and $226 \mu\text{W}$ for 4 electrodes stimulation where the total power dissipation is about $281 \mu\text{W}$ and lower than a typical presented cochlear implant power in literature. Comparing the power requirements of the CI electronics and nerve stimulating electrodes, it can be seen that the piezoelectric harvester output below 100 dB SPL is not sufficient. While, a specifically adjusted acoustic signal at the resonance frequency of the harvester with a high amplitude sound can be utilized to charge the CI battery.

1.2.2 Piezoelectric Electrical Model

In order to develop a model for piezoelectric structure as shown in Figure 1.2, the following assumptions are taken: (i) the frequency of the input vibration is close to main natural frequencies of the cantilever beam, (ii) the different modes of resonance of the structure do not interfere with each other, (iii) mechanical and electrical wave propagation phenomena can be ignored. These assumptions allow describing the system in terms of lumped elements. Lumped parameter modeling is simplification of the physical system into several lumped discrete elements, which are describing the behavior of the physical system. This modeling approach is widely used for electrical circuits, and is also applicable to piezoelectric energy harvesters. By using piezoelectric constitutive equations (1.2) in term of macroscopic variables, restoring force (F) and mass displacement (u) as the mechanical domain are coupled with outgoing voltage (V) and Current (I) of the piezoelectric as the electrical domain.

$$\begin{cases} F = K_{pc}u + \Gamma V_p \\ I = \Gamma \dot{u} - C_p \dot{V}_p \end{cases} \quad (1.2)$$

In equation (1.2) K_{pc} is the stiffness of the piezoelectric beam, C_p is the piezoelectric capacitance, and Γ denotes coupling factor.

In 2002, Flynn et al. modeled piezoelectric coupling as a transformer, where transformer relates stress to electric field [34]. Thus, a transformer relation between these domains and electromechanical model of the piezoelectric energy harvester can be obtained by using circuit elements. The equivalent model of piezoelectric bending beam is represented in the form of two ports electrical network as shown in Figure 1.6

[35]. The left side of the circuit corresponds to mechanical domain and the right to electrical properties of piezoelectric. In the mechanical domain, a capacitor $C_m=1/k_c$ is the reciprocal mechanical stiffness and the effective beam mass is represented by an inductance $L_m=m_{eff}$. The electromechanical conversion is virtualized by a perfect transformer Γ related with coupling factor. In this particular application, the piezoelectric energy harvesters are subjected to steady state vibrations. Therefore, the ac voltage source is connected to the mechanical ports of the network as a source of mechanical energy. It is assumed to be $F=m_{eff}a_0\sin(2\pi ft)$, where a_0 and f stand for the excitation acceleration amplitude and excitation frequency, respectively. On the other side, the electrical ports are connected to an electrical load in which energy is stored or dissipated in parallel with piezoelectric capacitance C_P . The voltage developed across the piezoelectric layer is denoted as V_P .

Piezoelectric harvesters can be modeled in a simple way by a current source in parallel with a capacitance of the piezoelectric material, C_P , as shown in Figure 1.7. The input vibration is modeled by a current source where \dot{u} is the velocity of the vibration. The coupling factor, Γ , determines the energy conversion of the piezoelectric from the vibration to the electric voltage

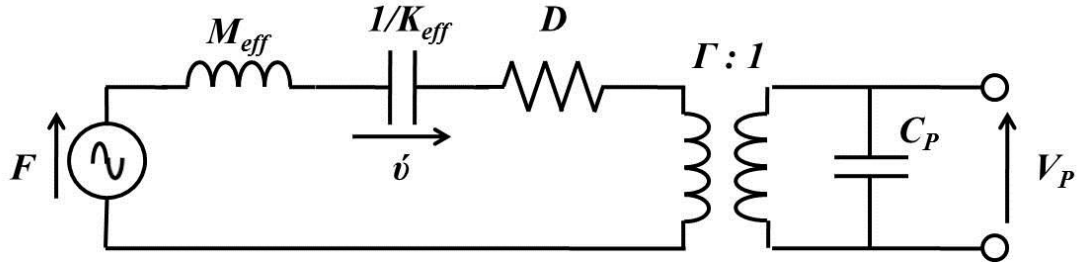


Figure 1.6. Equivalent network model for piezoelectric energy harvester.

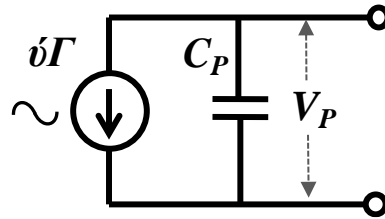


Figure 1.7. Simple piezoelectric electrical model used in circuit design simulations.

1.3 Overview of Interface Circuits for PEH

In this section, we discuss the most common and important techniques utilized to convert AC signal generated by vibration based piezoelectric transducers into the DC form. Piezoelectric harvesting IC can be divided into two main categories, namely standard rectifiers and nonlinear switching rectifiers.

1.3.1 Standard Rectifiers

Two standard rectifiers, full-bridge rectifier and voltage doubler are conventional AC-DC converters, which have been demonstrated in several works [36], [37]. As shown in Figure 1.8, the classic full-bridge rectifier includes a diode rectifier and a filter capacitor with terminal electrical load modeled by an equivalent resistor R . Figure 1.9 shows the other commonly used circuit, named as the Cockcroft-Walton voltage doubler. The circuit is quite practical for some applications when the electrical load with a high resistance needs higher power.

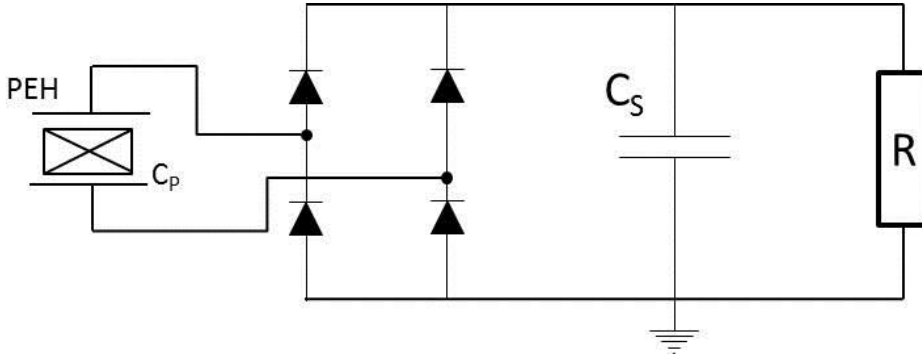


Figure 1.8. Standard full bridge rectifier.

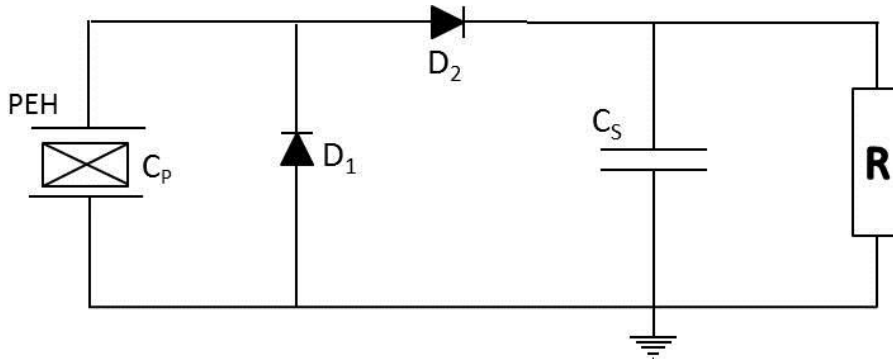


Figure 1.9. Cockcroft-Walton Voltage doubler IC.

These types of electronic interfaces and even active rectifiers suffer from low extraction efficiency due to significant power losses during intermittent vibrations. The main reason for the low extraction efficiency is that the rectifier has to charge and discharge the piezoelectric capacitor each cycle, which dissipates considerable power in the circuit. During charge transmitting to the output, effect of damping-force of the piezoelectric structure is limited, resulting in reduction of energy conversion factor. This leads to significant lower power extraction compared with the maximum available power.

Active rectifiers [38][39] were commonly employed to reduce power dissipation, which originates from the voltage drop in each diode of the rectifier circuit. Active rectifiers basically utilize monitoring comparators and switches instead of diodes to control power flow and minimize conduction loss. The main challenge is designing low power and accurate comparators to achieve higher power conversion efficiency. However, these circuits also suffer from reactive power dissipation due to capacitive impedance of the PEH.

Maximum power point tracking method is utilized to match load impedance of the full bridge rectifier to the real part of the source impedance, which enhances power efficiency. This achieves through adjusting duty-cycle of a DC-DC step-down converter [40]. The piezoelectric open-circuit voltage (V_{OC}) sensing method were implemented in [41] to keep output voltage of the full-bridge at half of V_{OC} . This approach improves significantly tracking time. Nevertheless, these methods focused on matching real part of the source impedance, and thus could not prevent wasting significant amount of transient charge at piezoelectric capacitance. Furthermore, the proposed methods are only effective for periodic vibrations.

Meantime, other researchers have looked into other circuit configurations for extracting more energy from the piezoelectric material [42]. These ICs utilize switching techniques based on non-linear processing of the voltage across the PEH and enable higher power extraction rates, by better matching of the circuit impedance with that of the piezoelectric element.

1.3.2 Nonlinear Switching Techniques

The piezoelectric generators' internal impedance is relatively high, which limits the delivered power to the traditional ICs with non-matching input impedance characteristics. Since the piezoelectric element has a large capacitance, a conjugate impedance matching circuit is required to maximize the generated power. It is known that an inductor can be added to compensate the contribution of the piezoelectric capacitor, but it cannot be adaptive to the energy-source variations. Moreover, the value of the inductance becomes too large for low frequency excitations. To overcome these drawbacks, switching-type charging circuits were proposed and have been popularly used in recent years. Several synchronized switching topologies and corresponding switching laws were proposed. These studies can be classified into two categories according to the placement of the rectifier and the inductor with active switches.

- I. Synchronous Electric Charge Extraction (SECE) [43],[44]: Inductor and switches are placed between the rectifier and output capacitance.
- II. Synchronous Switching Harvesting on Inductor (SSHI) [45], [42]: Inductor and switches are placed between the piezoelectric and the rectifier.

1.3.2.1 SECE

SECE ICs customizes the current flow to the output capacitance. This technique can be implemented both in fly-back [46] and buck-boost [47] topologies as shown in Figure 1.10. It is shown that harvested power can be increased up to 400% through the SECE topology, wherein the generated charge at peak displacement is transferred to the output capacitance through LC resonant circuits. SECE is an efficient approach among switching techniques for facilitating charge delivery and achieving matched load at the same time. The SECE converter was integrated within CMOS technology in [43]. Figure 1.11 shows implemented circuit that benefits from negative voltage converter (NVC) instead of full-bridge rectifier and can provide maximum efficiency of 70 %. However, the piezoelectric voltage level is limited to output voltage where higher piezoelectric voltage is clamped by bulk-drain diodes and thus remarkably constrained input power range. Furthermore, timing of switching instants is only set

for one voltage level that also limits operation range of the converter. Later, voltage limitation and timing problems were alleviated by enhanced structure [44] of integrated SECE circuit.

Energy extraction and transfer in several successive charge packages enables reduction in the size of off-chip electromagnetic components [48]. The fly-back SECE converter, implemented in [48], is efficient only for mechanical frequency range below 100Hz, and depends on digital inputs for establishing critical time constants related with piezoelectric and output storage capacitances, to regulate extraction and transfer durations. High input voltage level and low input frequency operation range are mapped to bulky piezoelectric harvesters, which are impractical for deployment in the implantable micro-devices.

In the SECE circuits, the switches should be operated synchronously with the vibration of the host structure in order to optimize the power flow; hence they require precise switching control circuitry. The performance of the switch control circuitry determines the efficiency of the whole system in exploiting harvested energy. The main drawbacks of the previously reported SECE implementations are their input voltage limitation and timing challenge [43]. Input limitation is related to minimum and maximum tolerable voltage of transistors and circuit implementation. The frequency and level of excitation range are befitting for macro-scale piezoelectric harvesters and making the circuit inefficient for lower power levels [44], [48], whereas for micro-scaled devices maximum extractable power by MEMS-based piezoelectric harvesters is even far below the required energy for properly operation of the switch control circuitry.

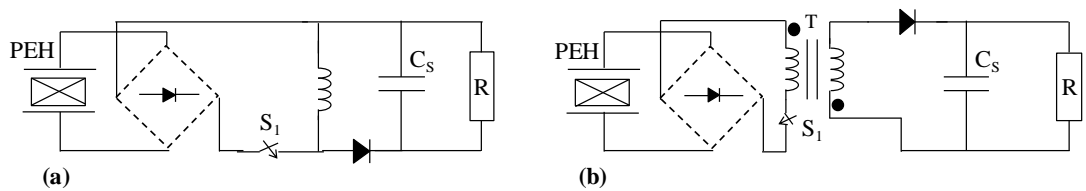


Figure 1.10. Circuit diagram of SECE converter implemented in (a) buck-boost and (b) fly-back topologies.

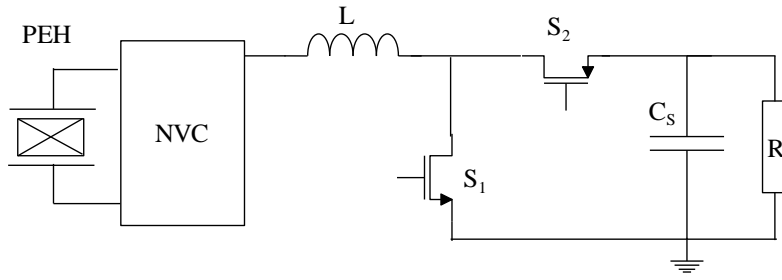


Figure 1.11. Circuit diagram of integrated implementation of SECE converter [43].

1.3.2.2 SSHI

SSHI technique was proposed in [45], shown in Figure 1.12, to transfer energy to the storage device with minimal charge dissipation at the rectifier through charge inversion on piezoelectric capacitance. At opposite displacement, charge generation is initiated close to conduction threshold of the rectifier by means of charge inversion at the end of previous conduction. It is shown that the electrical harvested power can be increased by as much as 900%, depending on load matching, over the standard technique. In this method, the power improvement strongly depends on the output load. Adjustment of charge inversion timing and startup are the other main challenges in designing of the SSHI converters

Garbuio [49] had proposed SSHI interface with Magnetic Rectifier as shown in Figure 1.13. It benefits from charge inversion on C_p through a transformer in each half-cycle instead of an inductor. Magnetic Rectifier allows decreasing power losses associated with diodes and reduces minimum input voltage level. The output power depends on output load at the higher resistance value with regard to the SSHI.

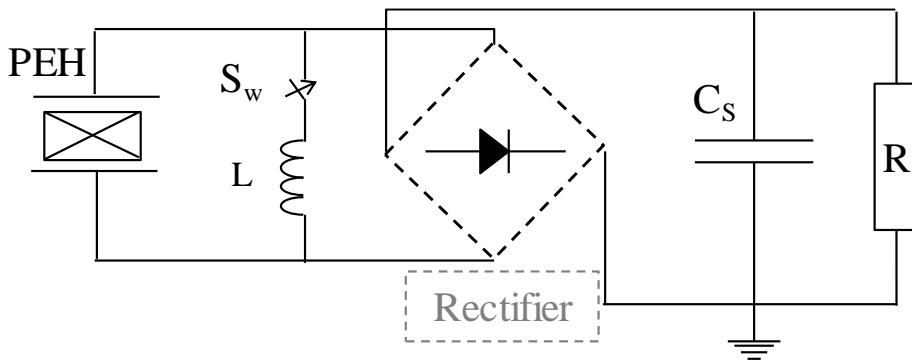


Figure 1.12. Equivalent circuit of series-SSHI converter.

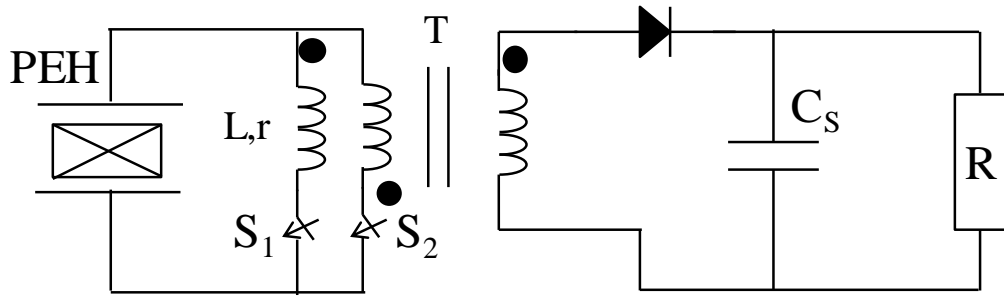


Figure 1.13. Equivalent circuit of SSHI MR converter [49].

Shen [50] aimed to optimize a series-SSHI with an intermediate switching stage, as presented in Figure 1.14. Two steps switching law was defined for extracting and transferring energy. This study optimized intermediate buffer capacitor to enhance extracted energy. Although, the dependence of output power to the load is reduced, the maximum extractable power is still dependent on preset voltage level, which is determined by the excitation level. Besides, a secondary piezoelectric harvester was utilized to start the harvesting circuit up.

On the contrary, Wu [51] used active diodes to secure optimal timing of charge flipping. However, the improvement of extraction power was not considerable compared to the ideal upper limit. Several adaptations [49][52] and on-chip implementations [53][54] were presented to enhance performance of the SSHI rectifier. However, high efficiency of SSHI can only be attained in limited range of excitation levels.

Aside from above methods, pre-biasing [55] and energy investment [56] methods have been presented to boost extracted power through investing portion of the stored energy into the piezoelectric capacitor to step up electrostatic force of the piezoelectric transducer. However, optimization of invested energy requires high battery voltage and cumbersome adjustments.

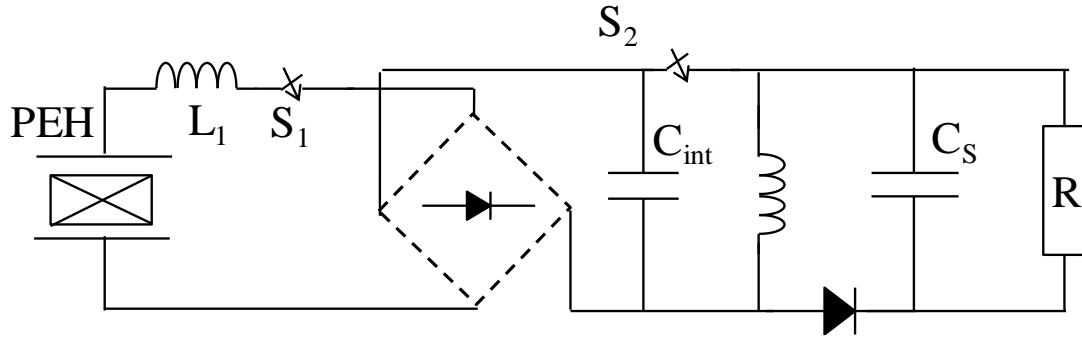


Figure 1.14. Equivalent circuit of enhanced SSHI converter [50].

1.4 Aim of This Study and Thesis Organization

Piezoelectric transducers provide higher power density than the electrostatic harvesters, and provide ease of integration, planarity and higher output voltage in comparison with electromagnetic counterparts. PEHs can supply power from μW to mW by extracting ambient vibrations. Besides, there has been tremendous development in micro-fabrication processes [57], [58] and power density of MEMS transducers [59]. The MEMS harvesters gain importance in volume and weight constrained applications such as bio-implantable devices [60], [2], and [61] where battery replacement is impractical and costly. Hence, development of an IC for PEHs gains significantly value.

The aim of this thesis is to realize practical harvesting ICs that are compatible with MEMS energy harvesters and can be used in real applications such as biomedical devices and WSNs. Design criteria for a practical IC can be listed as follows:

1. Power enhancement: The interface should harvest utmost extractable energy and outperform the standard rectifiers.
2. Independent extraction: The power extraction should be independent of the load and any design parameter.

3. Autonomous: The circuit should be self-powered and supply required power of control circuitry. It means that can capable of start up with no initial charge and operation without need to external supply voltage.
4. Synchrony: The circuit should adapt itself to variation of excitations and generate all necessary signals for proper operation.
5. High efficiency: Minimizing power consumptions containing quiescent current, conduction loss and switching loss allows the circuit to harvest any valuable energy and operate in wide range of excitation frequency

Low power and high mechanical frequency of MEMS PEH requires careful design of the AC/DC convertor to achieve high efficiency. SECE is an effective topology to interface piezoelectric harvesters operating at low voltages. Hence, the first main aim of this study **in chapter 2** is to present a circuit that fulfills all practical requirements for MEMS PEH. The proposed multi-stage energy extraction (MSEE) on buck-boost SECE architecture allows shrinking the external inductor without affecting power conversion efficiency. Although the core configuration of the circuit in this chapter is similar to SECE integrated circuits in [62], [63], a comprehensive power analysis is presented that leads to minimize power losses with the help of the multi-stage technique. In the previously reported multistage circuits, timing is calculated by multiplying digital inputs set by user and predefined coefficients, which requires measurements and hand-calculations. Moreover, compromises between mechanical frequency and power consumption cannot be avoided. The implementation of the multistage generator with energy sensing method eliminates efficiency and cost limitations arising from high mechanical frequency, additional digital inputs and timing problems. The several circuit enhancements including a high accuracy peak detector and ultra-low power control are implemented to extract maximum power for a wide input power and frequency range. The ultimate goal is to charge rechargeable energy storage element, hence a power management circuit is presented to fasten charge speed of high value storage capacitance.

As discussed in previous section, high efficiency of SSHI can only be achieved in higher excitation levels in limited range. On the other hand, SECE provide load independent power extraction with lower power gain. **In the chapter 3**, a novel double synchronized switch harvesting (DSSH) circuit is presented to bridge the gap between SSHI and SECE techniques. The aim of this work is to integrate a self-adapting DSSH IC to boost extracted power from micro-watt piezoelectric energy harvesters. A novel MPP sensing approach is proposed to achieve optimal point of operation for the proposed circuit regardless of input excitation level, for the first time in literature. The one of main challenges in this nonlinear switching is adjusting exact time of charge inversion for variable vibrations. In this respect, a sensing circuit is designed to secure optimum charge inversion time for wide range of the input vibration. The implementation of an enhanced switching technique and MPP circuit aims to simultaneously provide high power extraction gain and load independence with a single inductor.

Harvesting energy from both low and high frequencies are beneficial in terms of increased power capacity, which in turns improves lifetime and system reliability. In the literature, there are numerous electronic systems for harvesting low frequency vibrations through electromagnetic harvesters [64], and high frequency vibrations through piezoelectric harvesters [65], [51], however few studies exist for a hybrid system. **Chapter 4** presents an efficient hybrid energy harvesting interface to simultaneously scavenge power from electromagnetic (EM) and piezoelectric sources, and drive a single load. The EM harvester output is rectified through a self-powered active doubler structure, and stored on a buffer capacitor and a SECE converter is utilized to interface PEH. A novel power management circuit is designed to extract energy from two energy sources at the same time with high conversion efficiency. The total simultaneously extracted power from both harvesters is more than the power obtained from each independently. A wearable energy harvesting system is fabricated to validate hybrid operation. The hybrid system is carried on a human wrist to collect energy from body movements.

CHAPTER 2

IC FOR PEHS DESIGN I: MULTISTAGE ENERGY EXTRACTION BASED ON SECE TECHNIQUE

The aim of this work is to realize an autonomous harvesting circuit that is compatible with MEMS energy harvesters used to power-up biomedical devices. As discussed in chapter 1, SECE is an efficient approach among switching techniques for facilitating charge delivery and achieving load matching at the same time. The main challenge in this approach is extracting maximum power for a wide input power and frequency range. On the other hand, the SECE requires large size of off-chip electromagnetic components to achieve high power-conversion efficiency. The previously implementations of the SECE are efficient only for high input voltages [44], mechanical frequency range below 100Hz [48], and depends on external adjustments for establishing critical time constants [43], [48] associated with piezoelectric and output storage capacitances. High input voltage and low input frequency operation necessitates a large harvester, which is impractical for deployment in implantable micro-devices. This chapter presents a power optimized SECE IC that improves the minimum required input power and frequency range of MEMS PEHs with low voltage output. In particular, an original multistage energy extraction technique has been implemented through a unique energy-based multistage generator circuit in an integrated SECE converter system to simultaneously achieve low cost and high power conversion efficiency. IC is optimized, prototyped and evaluated in this study. The principle of circuit operation, power optimization approach, and power management method are presented in the following section. Proposed circuit and implementation details are illustrated in Section 3 summarizes test setup and experimental results. Finally, the study is discussed in Section 4.

2.1 Interface Circuit Design

The proposed circuit comprises four processing stages including negative voltage conversion, start-up, active extraction, and power management. A negative voltage converter (NVC) provides positive voltage by converting the negative part of the AC voltage generated. Figure 2.1 depicts the block diagram of the proposed circuit. The rectified voltage from NVC charges the storage capacitor, C_{stor} , at wake-up, through start-up circuit. The active power extraction is realized through a set of power switches and an external inductor. At the final stage, a power management circuit (PMC) is used to fasten charge of supercapacitance or rechargeable battery. In practical, the IC's load is the battery voltage level that varies during charging process.

The active extraction is designed based on the SECE technique. The power extraction is realized through three phases managed by control unit as shown in Figure 2.2. In the first phase, all switches in Figure 2.2 (a) are turned OFF to bias the PEH at open circuit condition until its output peaks. After peak detection, energy stored on the PEH capacitor is transferred to the inductor through C_p -L resonant circuit by turning S_1 and S_3 ON. The third phase is entered when PEH voltage reaches zero. At this point, S_1 and S_3 are turned OFF, S_2 and S_4 switches are turned ON, and the stored energy on the inductor is transferred to the storage capacitor, C_{stor} . Charging of the capacitor continues until the inductor current reaches zero.

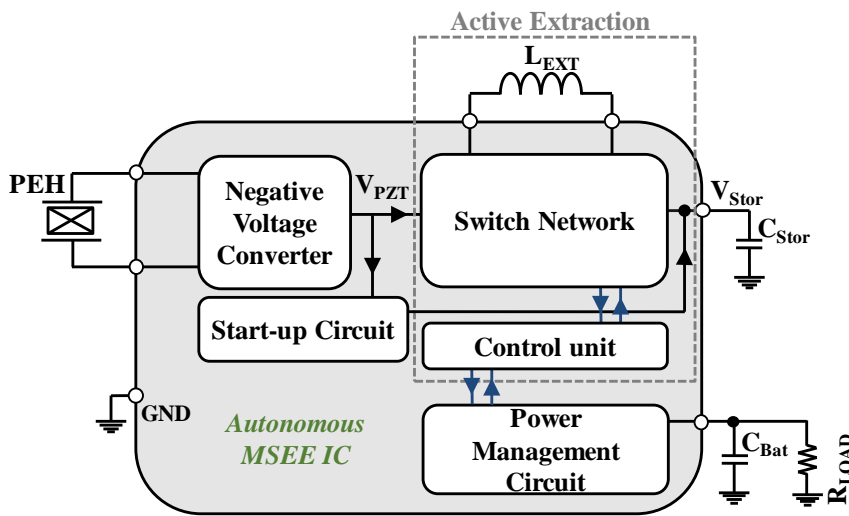


Figure 2.1. The overview of proposed energy harvesting IC.

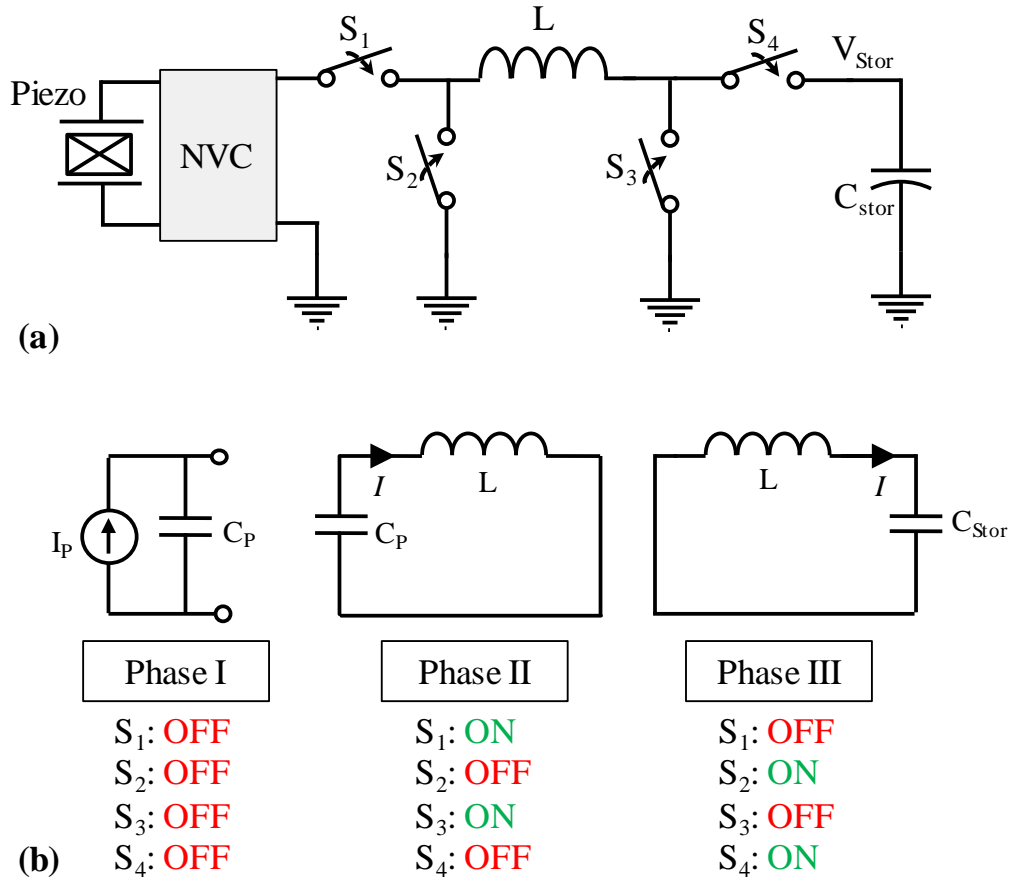


Figure 2.2. (a) Switch network and (b) extraction phases with corresponding state of the switches.

2.2 Multi-stage Process

MEMS piezoelectric harvesters have been utilized to generate rms output power range from μW up to hundred's μW under different vibration levels. Power optimization to improve the minimum required input power and frequency range of MEMS PEHs with low voltage output is of essential necessity for the SECE IC. In highly charged cases, the power extraction stage has to use large inductive component to avoid huge losses in the circuit. Therefore, a multistage process has been proposed to maintain the control of the higher input power levels over low-volume inductor ($100\ \mu\text{H}$ - $3.3\ \text{mH}$). In this configuration, the discharge of the piezoelectric harvester will be performed at the same moment as that of SECE, however, the second and third phases are repeated in sequence according to the defined stage number, N , as shown in Figure 2.3.

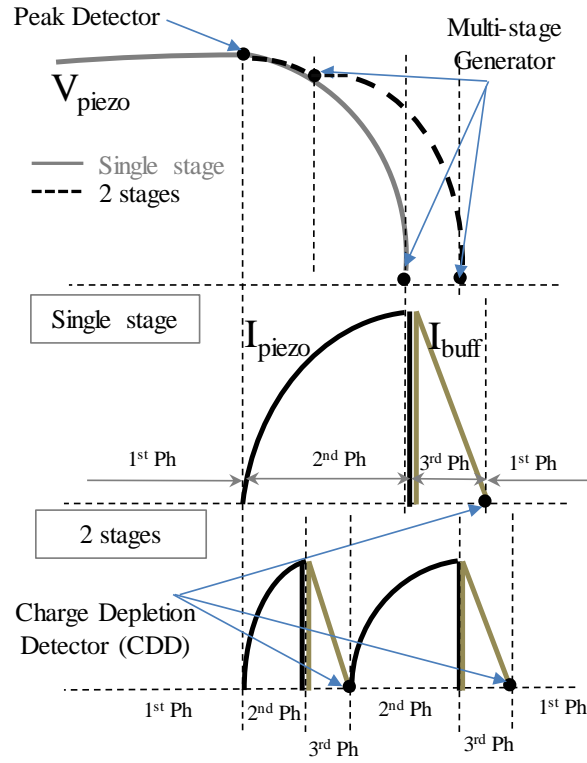


Figure 2.3. Extraction phases and critical switching points of the SECE in time domain for single and two-stage transfers.

The IC extracts generated energy in N successive packets. The energy transferred at each stage, n , through inductor is equal to $\frac{1}{2}C_p V_{OC}^2/N$, where V_{OC} is the generated open circuit voltage at piezoelectric capacitor, C_p . Thus, the magnitude of the oscillation current depends on the total stage number N through the following relationship:

$$i_{peak,n} = V_{oc} \sqrt{\frac{C_p}{L \times N}}. \quad (2.1)$$

The extraction time duration, $T_{p,n}$, is worked through energy conservation to derive the same quantity of energy at the inductor in each stage:

$$T_{p,n} = \frac{1}{\omega_p} \cos^{-1} \sqrt{\frac{N-n}{N-n+1}} \quad (2.2)$$

During $T_{s,n}$, the energy of the inductor is transferred to the buffer capacitor. This period can be obtained by solving LC resonant circuit with initial the capacitor and the inductor values. $T_{s,n}$ is approximated as follows by assuming $C_{stor} \gg C_p$:

$$T_{s,n} = L \frac{i_{peak,n}}{V_{stor}} \quad (2.3)$$

In our proposed approach, energy packet size is determined with energy sensing method that does not require explicit calculation of extraction time duration. The generated energy in the first phase is sensed through a downscaling circuit, and is divided by N with the help of a capacitor network. It is then compared with the energy extracted in the second phase, which is measured through a current sensing and energy converting circuit to determine the magnitude of the energy packet.

Eventually, the current magnitude in each stage is reduced by $\sqrt{1/N}$. Therefore, the conduction loss of the power switches and the inductor is decreased in proportion to the current reduction passed through inductor-switch network. In addition, this approach allows utilizing a low volume inductor with small series resistance, which is desired for reduced system footprint and cost. Power analysis is discussed in next part.

2.2.1 Power Analysis

The energy generated on piezoelectric capacitor, C_p , as the beam vibrates, due to mechanical excitation of the harvester, is obtained as:

$$E_{Coupled} = \frac{1}{2} C_p V_{OC}^2. \quad (2.4)$$

The coupled energy is extracted through discharging the piezoelectric capacitor and transferred to output buffer capacitance. The e pure energy harvested, E_{Harv} , are calculated as:

$$E_{Harv} = E_{Coupled} - E_{loss} \quad (2.5)$$

There are four sources of power dissipation in the switching circuit: Resistive conduction losses in the inductors and MOSFET switches (P_{cond}); charge redistribution losses at MOSFET parasitic capacitances during phase changes (P_{sw}), capacitive

switching losses at the gates of power switches (P_{driv}), and leakage current associated with any MOSFET in OFF state (P_{leak}).

$$P_{\text{loss}} = P_{\text{cond}} + P_{\text{sw}} + P_{\text{driv}} + P_{\text{leak}} \quad (2.6)$$

With regard to circuit configuration and stage number, four dynamic power losses are expressed as follow:

$$P_{\text{cond}} = (R_{\text{ind}} + R_{\text{sw1\&sw3}}) \times \sum_N \int_0^{T_{p,n}} i_{p,n}^2 dt + (R_{\text{ind}} + R_{\text{sw2\&sw4}}) \times \sum_N \int_0^{T_{s,n}} i_{s,n}^2 dt \quad (2.7)$$

$$P_{\text{driv}} = (Q_{g,\text{sw2,3,4}} V_{\text{stor}} + Q_{g,\text{sw1}} V_{\text{oc}}) f_{\text{exc}} \quad (2.8)$$

$$P_{\text{sw}} = C_{\text{ds,sw2}} V_{\text{pz,n}}^2 f_{\text{exc}} + C_{\text{ds,sw3}} V_{\text{stor}}^2 f_{\text{exc}} \quad (2.9)$$

$$P_{\text{leak}} = i_{\text{leak}} w_{\text{sw1}} V_{\text{oc}} + i_{\text{leak}} w_{\text{sw4}} V_{\text{stor}} \quad (2.10)$$

I_{leak} is leakage current per width specified in the technology datasheet.

In the above equations, on-resistance R_{ON} , gate charge Q_g , drain-source capacitance and C_{ds} are approximated by following equations:

$$R_{\text{on}} = 1/\mu C_{\text{ox}} \frac{W}{L} (V_{\text{gs}} - V_{\text{th}}) \quad (2.11)$$

$$Q_g = 2C_{\text{ov}} W V_{\text{gs}} + C_{\text{ox}} W L (V_{\text{gs}} - V_{\text{th}}) + C_{\text{ov}} W V_{\text{ds}}, \quad (2.12)$$

$$C_{\text{ds}} = W L_D C_j (1 - \frac{V_{\text{ds}}}{P_B})^{-M_j} + (W + L_D) C_{j\text{sw}} (1 - \frac{V_{\text{ds}}}{P_{B\text{sw}}})^{-M_{j\text{sw}}}, \quad (2.13)$$

where μ is mobility of electron or hole, C_{ox} is gate oxide capacitance per unit area, C_{ov} , is gate overlap capacitance per unit length, C_j is drain bottom junction capacitance per unit area at zero bias, $C_{j\text{sw}}$ is drain sidewall junction capacitance per unit length at zero bias, P_B is drain bottom junction built-in voltage, $P_{B\text{sw}}$ is drain sidewall junction built-in voltage, M_j is drain bottom junction grading coefficient, L_D is lateral diffusion length, and $M_{j\text{sw}}$ is drain sidewall junction grading coefficient.

2.2.2 Power Optimization

The above equations indicate that on-resistance and gate-charge of the switch S_2 vary with input piezoelectric voltage, while the same parameters are sensitive to the storage voltage for the other switches. The substitution of equations (2.12-2.14) into equations (2.8-2.11) shows that all four power-dissipation sources depend on power switch size, input piezoelectric voltage, and storage voltage (V_{stor}).

In implemented technology, 180nm HV CMOS, N-MOSFET and P-MOSFET power switches tolerate up to 12 V and 17 V at their terminals, respectively. The MSEE chip requires minimum supply voltage of 1.1 V to drive power switches and achieve proper operation of the MSEE. The maximum storage voltage is limited to 3.3 V, which is defined by 3.3 V MOSFETs utilized in control unit. After thorough investigation of losses, within 180nm HV CMOS, the total power loss is obtained as a function of N-MOSFET power switch sizes and corresponding aspect ratio of the P-MOSFET switches, as shown in Figure 2.4. Since efficient extraction in low-power outputs of the MEMS PEHs are intended, minimum input voltage is set to 1.5 V and storage voltage is set to maximum allowable value, $V_{stor}=3.3$ V. The power switch (S_1 - S_4) sizes have been optimized, as $W=4$ μ m for a minimum power loss of 0.86 μ W at just above the lowest allowable PEH voltage, $V_{OC,pp}=1.5$ V. This optimization improves power efficiency for the low input power scenario, while maintaining the control of the higher input power levels through MSEE.

Stage number is adapted to achieve maximum charging efficiency for higher input power levels at optimized power switch sizes. Minimum total power loss corresponds to the stage number provides a balance between conduction power losses and switching power losses. Figure 2.5 shows calculated total power loss at maximum allowable piezoelectric voltage as a function of number of the stages. Minimum power loss at $V_{OC,pp}=12$ V is determined for number of stages four. Therefore, MSEE is implemented up to four stages and number of stages is automatically controlled by multi-stage generator.

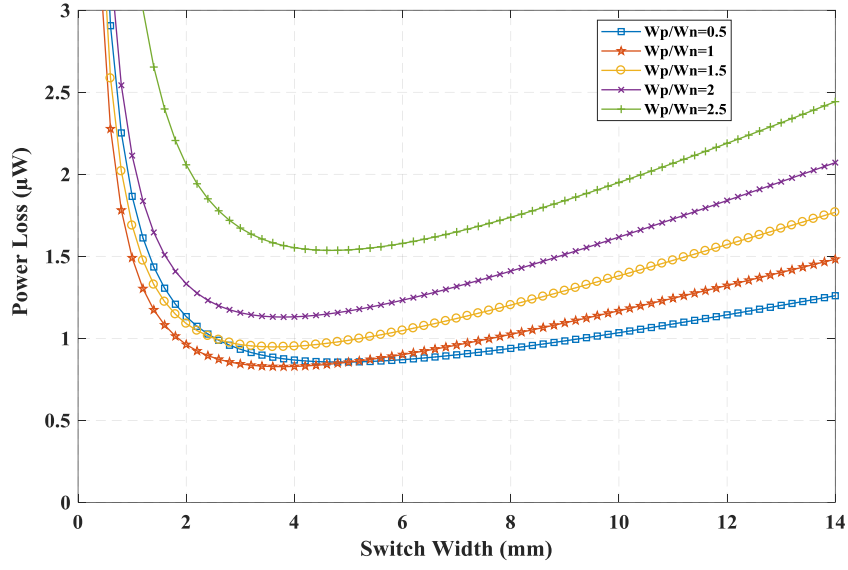


Figure 2.4. Total power losses vs. power switch sizes @ $V_{OC,pp}=1.5$ V simulated in MATLAB.

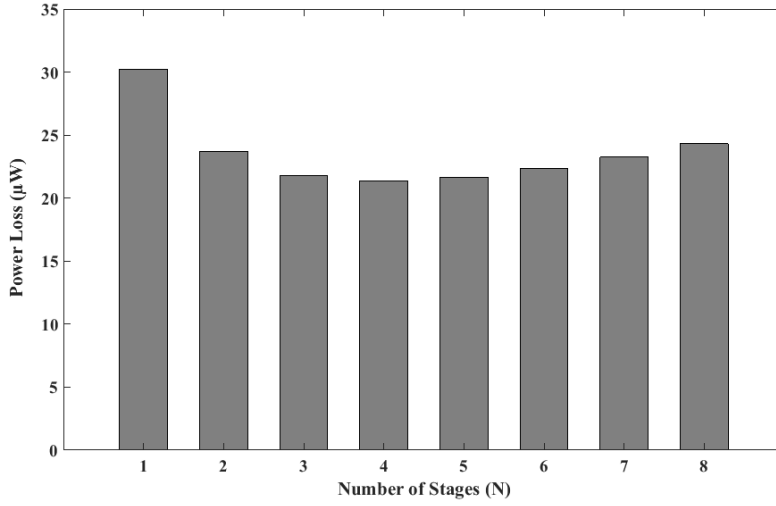


Figure 2.5. Total power loss vs. number of stages @ $V_{OC,pp}=12$ V simulated in MATLAB.

2.3 Power Managing Process

The power management approach aims to fasten charging time of large-capacity storage element with reducing transition time from passive mode to active mode. The architecture of the system contains two charge paths with a small value storage capacitor and the large-capacity storage element such as rechargeable battery or super-capacitor as depicted in Figure 2.6 (a). C_{stor} feeds the control unit whereas the C_{OUT}

powers up the load. This leads to decrease considerably charging-time for supplying active extraction compared with single large-capacity storage.

Initially, C_{stor} is passively charged via NVC and a diode while it is controlled with a start-up circuit to activate SECE operation. During Active mode, the PMC controls energy flow to C_{stor} and C_{OUT} as shown in Figure 2.6 (b). The lower threshold voltage secures the safe operation of the SECE circuit and the upper threshold voltage provide back-up energy to redirect energy flow to C_{OUT} . As V_{stor} reaches to a certain threshold voltage, the PMC detect it and the signal changes state. By alternating these two paths, the system starts with no initial charge in either reservoirs and fastens charging huge energy storage element.

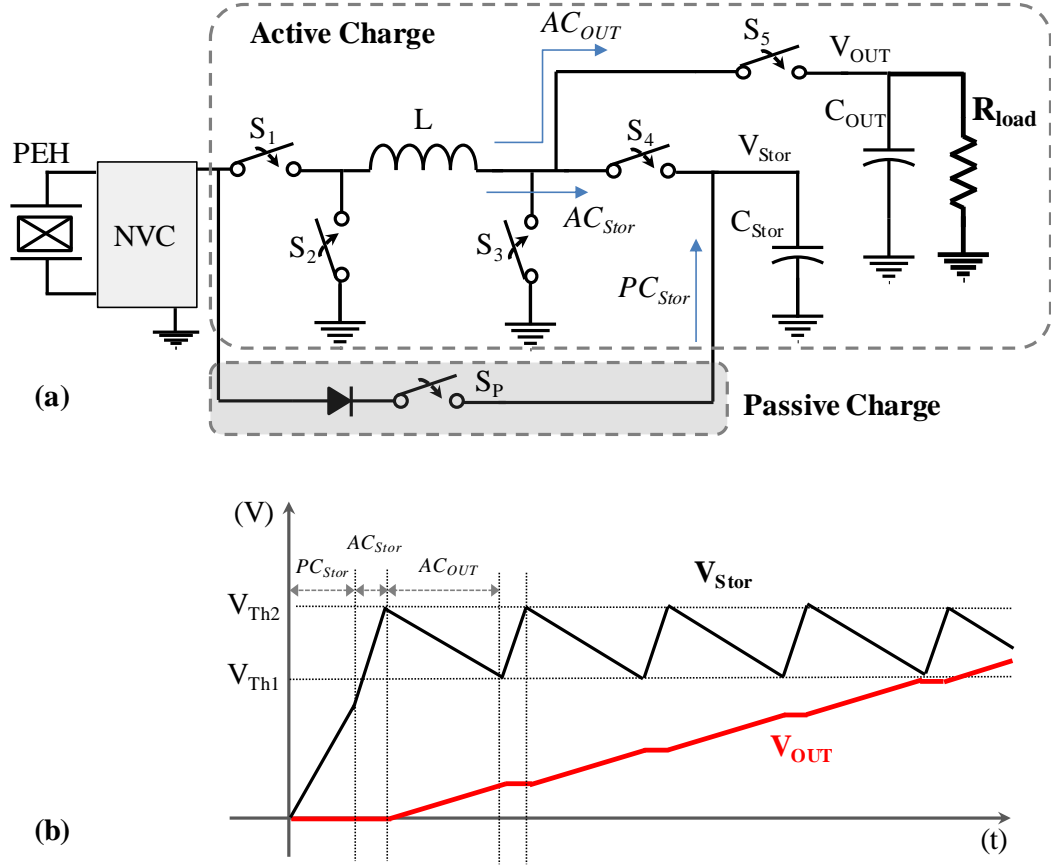


Figure 2.6. (a) Schematic of proposed circuit for charge management circuit and (b) operation principle.

2.4 Implementation of the Proposed Circuit

Figure 2.7 shows the schematic of the front-end multistage energy extraction (MSEE) circuit. NVC, shown in Figure 2.8, is implemented to provide only positive voltage so that peak-to-peak open circuit voltage is generated in each half cycle. Two switches controlled with two comparators and two cross-coupled PMOS switches, which are driven by piezoelectric harvester, determine the charge-flow path to provide positive voltage. At wake-up, The positive voltage, V_{piezo} , charges the storage capacitor, C_{stor} , through a diode and a control switch. The trigger circuit decouples the supply voltage of the control unit (V_{DD}) and storage voltage (V_{stor}) as long as $V_{\text{stor}} < V_{\text{trig}}$. The trigger circuit feeds the stored power into the control unit ($V_{\text{DD}}=V_{\text{stor}}$), and blocks the start-up path when $V_{\text{stor}} > V_{\text{trig}}$. In active mode, S_1 power switch is realized with two transmission-gates, as shown in Figure 2.8, which are redirected by NVC in each half-cycle according to piezoelectric displacement. In this way, cross-coupled PMOS switches of the NVC are bypassed and consequently related voltage drop and conduction loss are eliminated. NVC also provides positive voltage through cross-coupled PMOS switches for start-up circuit. These cross-coupled PMOS switches are blocked by start-up circuit in active mode. On the other side, PMC controls energy flow into C_{stor} and C_{BAT} through S_4 and S_5 according to predetermine voltage threshold levels defined previously.

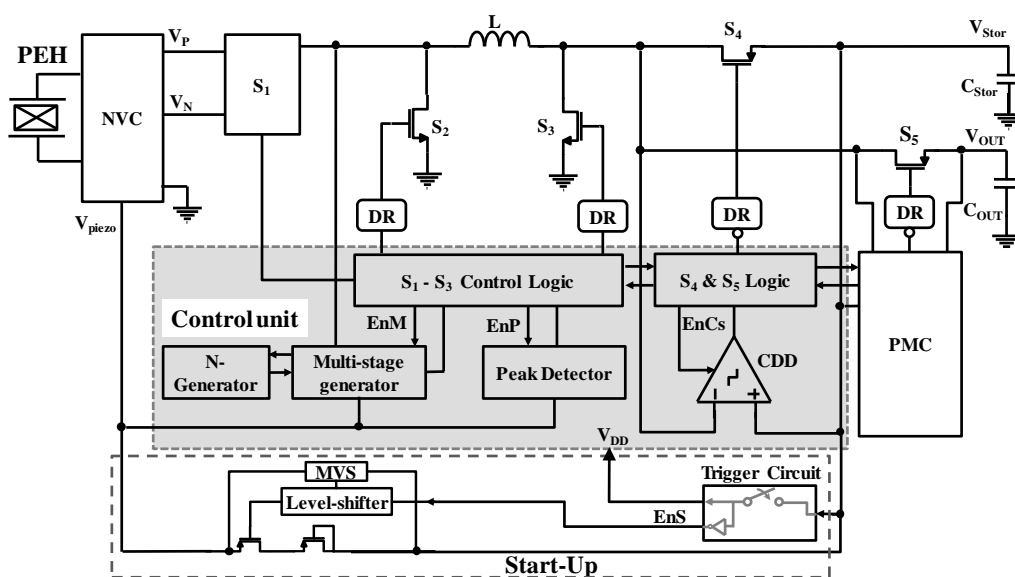


Figure 2.7. Schematic of autonomous multi-stage energy extraction circuit.

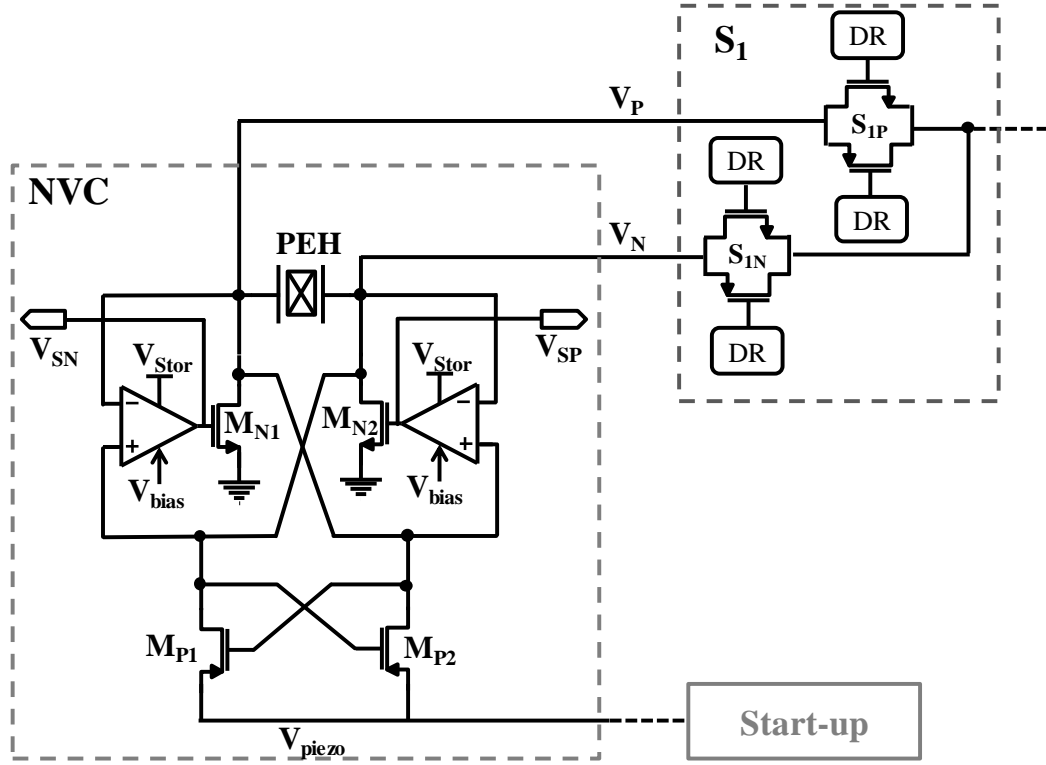


Figure 2.8. Circuit diagram of NVC and S_1 switch.

2.4.1 Trigger Circuit

Figure 2.9 shows schematic of the trigger circuit. When the input voltage increases from zero, the control signal, D_{trig} , follows the input voltage while the output voltage remains zero due to the fighting at node X. When M_{P0} gets stronger than M_{N0} and resistor combination, node X is pulled up by M_{P0} and the output terminal starts following the input voltage through the pass transistor, M_{Pass} , while D_{trig} is shorted to ground. The measured output waveforms of the circuit in response to triangle input voltage is shown in Figure 2.10.

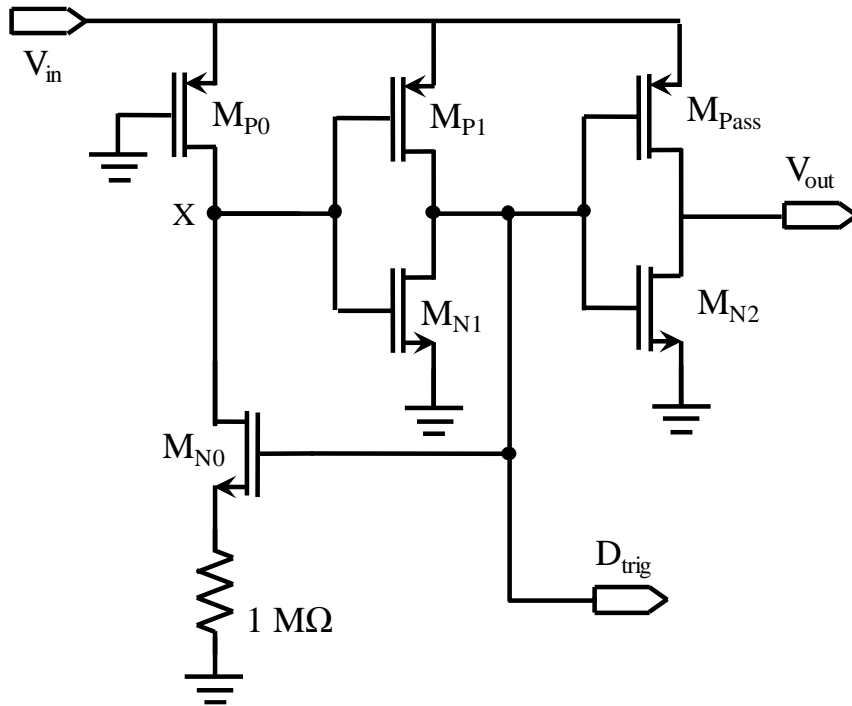


Figure 2.9. Schematics of the trigger circuit.

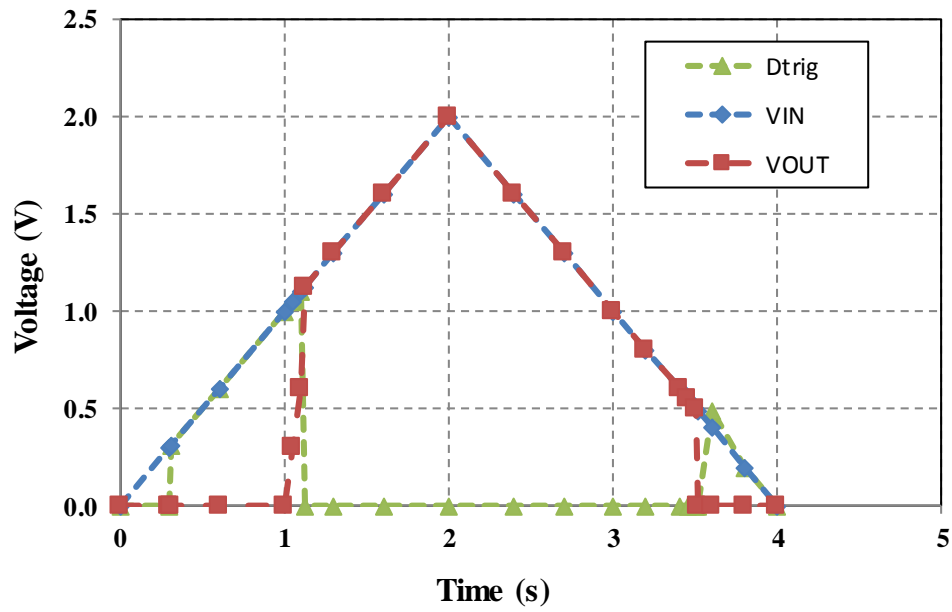


Figure 2.10. Measured voltage waveforms of the Start-up circuit.

2.4.2 Control Unit

The control unit consists of detectors and logic circuits to process the detectors' signals and control operation of the detectors. Peak detector, multi-stage generator, and charge depletion detector (CDD) sequence the switch drivers according to the phases described in the previous section, in order to realize the multi-stage synchronous charge extraction.

2.4.2.1 Novel Peak Detector:

The proposed peak detector, shown in Figure 2.11, is designed to operate at PEH voltage levels higher than supply voltage, V_{DD} . The circuit operates in current mode with internal negative feed-back. A series capacitor, C_{PK} , converts piezoelectric voltage to current, I_S , where Node V_X is reset to the ground, previously. Negative feed-back action on M_{N0} and M_{P0} forces Node V_X to be charged just around the threshold voltage of the M_{N0} MOSFET. As PEH voltage peaks, I_S crosses zero, and voltage drop of the node V_X over M_{P0} turns M_{N0} OFF. As M_{N0} turns OFF, the node V_Y is pulled up by mirroring reference current through the node. Common source amplifier and digital inverters in the output stage deliver a high edge rate. Figure 2.12 illustrates the operation of the peak detector through the voltage and current simulation waveforms. The accuracy of the peak detector is critical in viewpoint of power conversion efficiency. The previous current-mode peak detectors [62], [56], [48] suffer from offsets due to reference-current level and device mismatch of the current comparator. The proposed circuit resolves above issues using an active switch (M_{N0}) instead of the current comparator. With increasing piezoelectric voltage, switch M_{N0} turns ON, and consequently M_{P0} starts conducting to regulate voltage at node V_X due to feedback between V_X and V_Y . When I_S reaches zero, M_{P0} dissipates accumulated charge at node V_X , turning off M_{N0} . The applied method alleviates the sensitivity of the circuit to process variation and mismatches in MOSFETs. The proposed circuit pulls up node V_Y through $I_{pull-up}$ without contending with peak I_S , which results in significant improvement in response time. The upper limit of the input frequency determines the reference current value, while the minimum detectable amplitude determines the value of the series capacitor, C_{PK} . D_{rst} goes high to connect node V_X to ground as the extraction phase is entered. This suppresses I_S oscillation that is caused by the resonant

switching in the second phase. The aforementioned techniques and features with experimentally proven performance (Section 2.5.4) indicate superiority of proposed circuit over detectors.

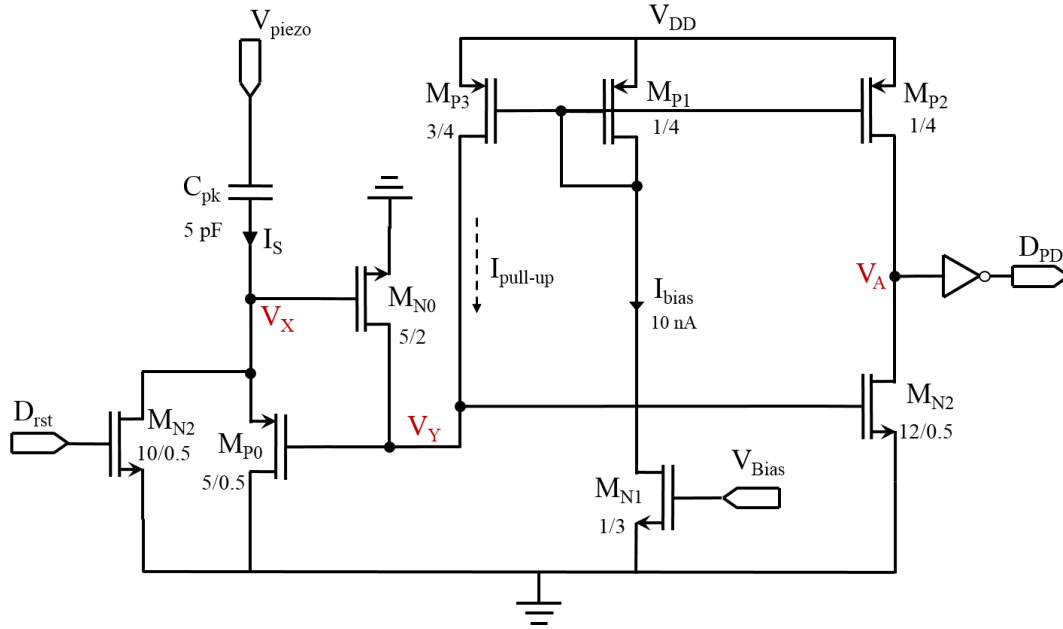


Figure 2.11. Schematic of the implemented Peak Detector.

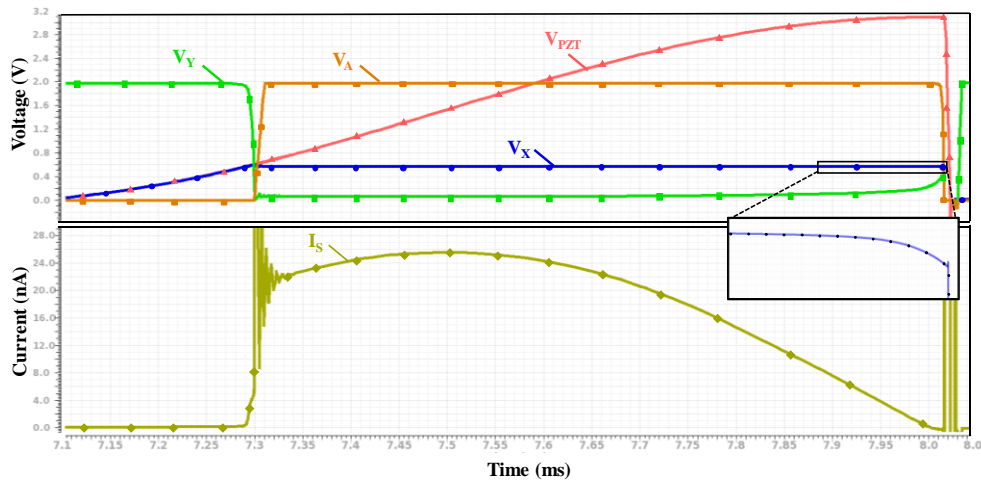


Figure 2.12. Simulated Voltage and current waveforms of the peak detector.

2.4.2.2 Multi-stage Generator Circuit

The multi-stage generator, depicted in Figure 2.13(a), relies on energy drain without any calibration requirement. This circuit comprises of two energy sensing circuits and a comparator. The energy generated on piezoelectric capacitor is sensed by the energy sensing circuit called energy stored in piezoelectric (ESP) in the first phase. The ESP utilizes a capacitor to convert piezoelectric voltage to current with the help of Flipped Voltage Follower (FVF). The FVF provides almost constant voltage on negative terminal of the capacitor through feedback connection of two cascoded transistors. Through two current mirrors, the sensed voltage is regenerated over sensing capacitors with minimum voltage downscaling of C_S/C_{OP} . When PEH voltage peaks, ESP circuit switches to hold state by lowering enable signal in order to save the measured voltage. During the second phase, energy transferred to the inductor is sensed through energy transferred on inductor (ETI) circuit based on the same principle, and the same size of sensing capacitance, $C_{SI}=C_{SP}$. The number of extraction steps (N) determines the capacitors connected in parallel to divide sensed energy by N. Four equally sized capacitors, $4 \times C_{OI}=C_{OP}$, are controlled to obtain desired value, $C_{T,OI}=C_{OI} \times M_1 + C_{OI} \times M_2 + C_{OI} \times M_3 + C_{OI} \times M_4$. Finally, N-division of sensed energy with ETI through V_{ETI} is compared with generated energy, determined through V_{ESP} , using hysteresis comparator to determine energy packet size transferred to the inductor. This guarantees constant energy extraction at each stage as shown in Figure 2.13(b). Multi-stage output signal initiates the third phase to harvest the generated energy, and C_{OI} is reset for next extraction. The operation principle and related signals are illustrated in Figure 2.13(b). The number of extraction stages is controlled through M_{1-4} , generated from 2 digital bits (labeled N in Fig. 1) and a decoder.

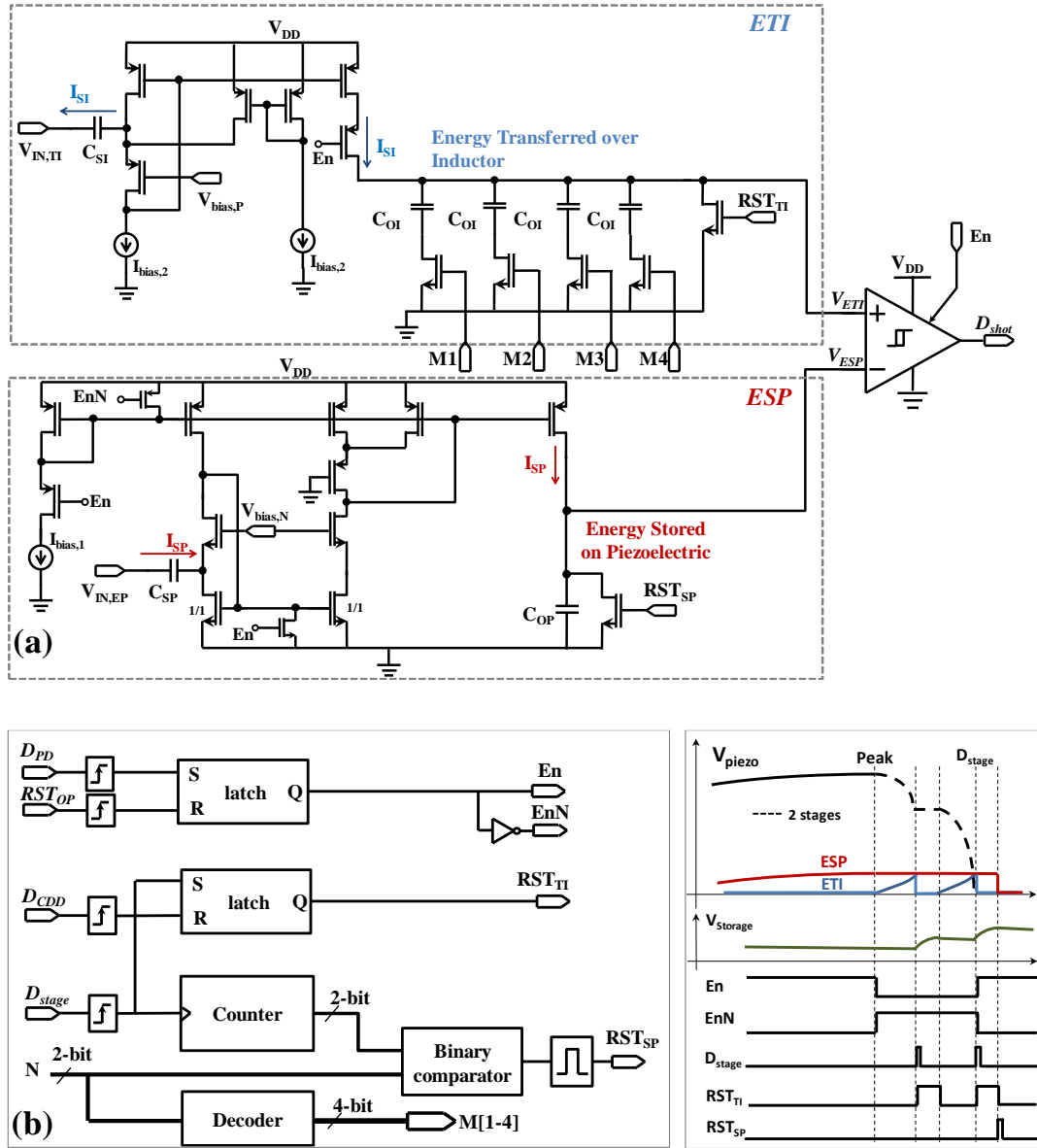


Figure 2.13. (a) Implemented Multi-stage generator: (b) Operation principle and related signals.

2.4.2.3 N Generator

Optimum number of stages is determined through quantization of the piezoelectric open circuit voltage, V_{OC} , as shown in Figure 2.14. The downscaled piezoelectric voltage, V_{ESP} , generated through multi-stage generator in the first phase is converted to current with a modified load device, where the drain of the NMOS device connects to its bulk. This configuration provides a finite and controllable resistance in subthreshold region. The sensed current is quantized through current comparison with

reference current. After digital processing, 2-bit digital output is used as an input for the Multi-stage generator circuit. The circuit is tuned with the results obtained through optimization in section 3.2 and further adjustment can be done by tuning $V_{bias,R}$.

2.4.2.4 Charge Depletion Detector (CDD):

Depletion of stored energy in the inductor to storage capacitance is controlled by a charge-depletion comparator as shown in Figure 2.15, with a relatively high bandwidth. The comparator monitors the voltage across S_4 switch to detect the end of inductor discharging. The CDD is only activated in the fourth phase to save power.

2.4.3 PMC

PMC controls energy flow into C_{Stor} and C_{BAT} according to predetermine voltage threshold levels (V_{Th1} , V_{Th2}). PMC consists resistors with a total value of $20.5\text{ M}\Omega$ in series and hysteresis comparator and a SR latch. Resistive fractions of V_{Stor} are compared with a stable reference voltage to signal exceeding threshold levels and SR latch ordinates changing path as shown in Figure 2.6. The comparators are designed in subthreshold region to reduce the power consumption.

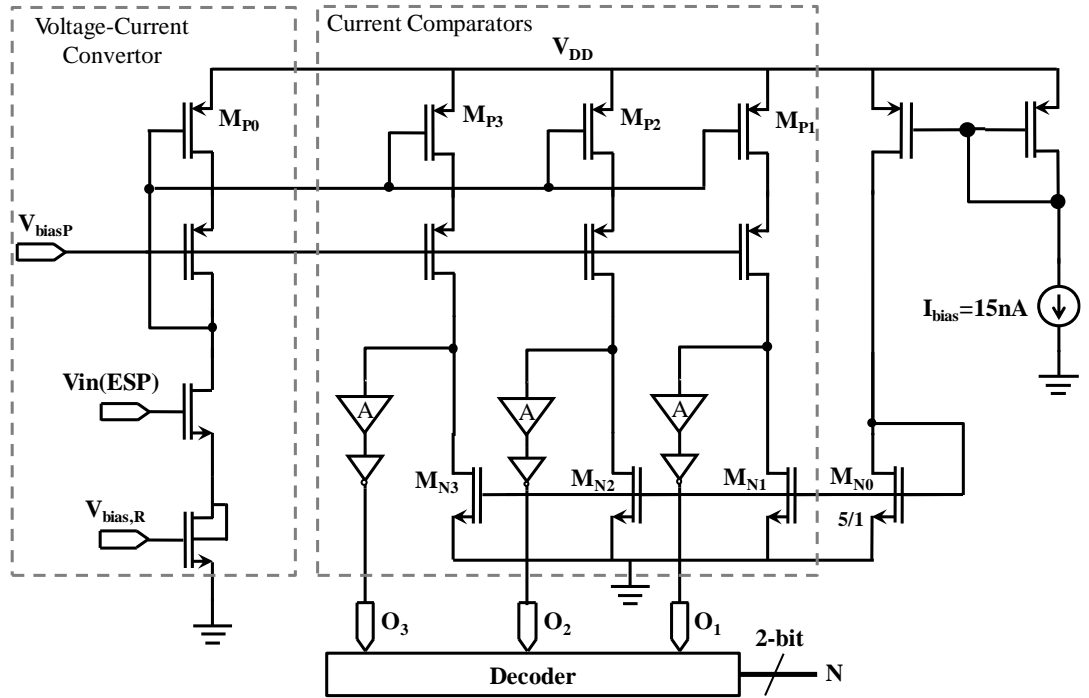


Figure 2.14. Implementation of N generator.

2.5 Experimental Results

The IC is designed in 180 nm HV CMOS technology from X-FAB Company. The IC is implemented in an active area of 2 mm^2 within $1.5 \text{ mm} \times 1.5 \text{ mm}$ die. The setup for experimental measurements is shown in Figure 2.17 with micrograph of the chip. A custom MEMs piezoelectric harvester [66], fabricated in METU_MEMS center, is mounted on holding board. The MEMS harvester with footprint of $9 \text{ mm} \times 4 \text{ mm}$ has a capacitor of 4 nF . The MEMS harvester is excited at its resonance frequency with a shaker table consisting of a control unit, an amplifier, a feedback accelerometer, and an interface computer.

The performance of the IC has been measured using a MEMs piezoelectric harvester with $C_p=4 \text{ nF}$ attached to a shaker table. An inductor ($L=1 \text{ mH}/5.1 \text{ } \Omega$) is connected to the chip to charge a $1 \text{ } \mu\text{F}$ storage capacitance in parallel with a variable load resistance.

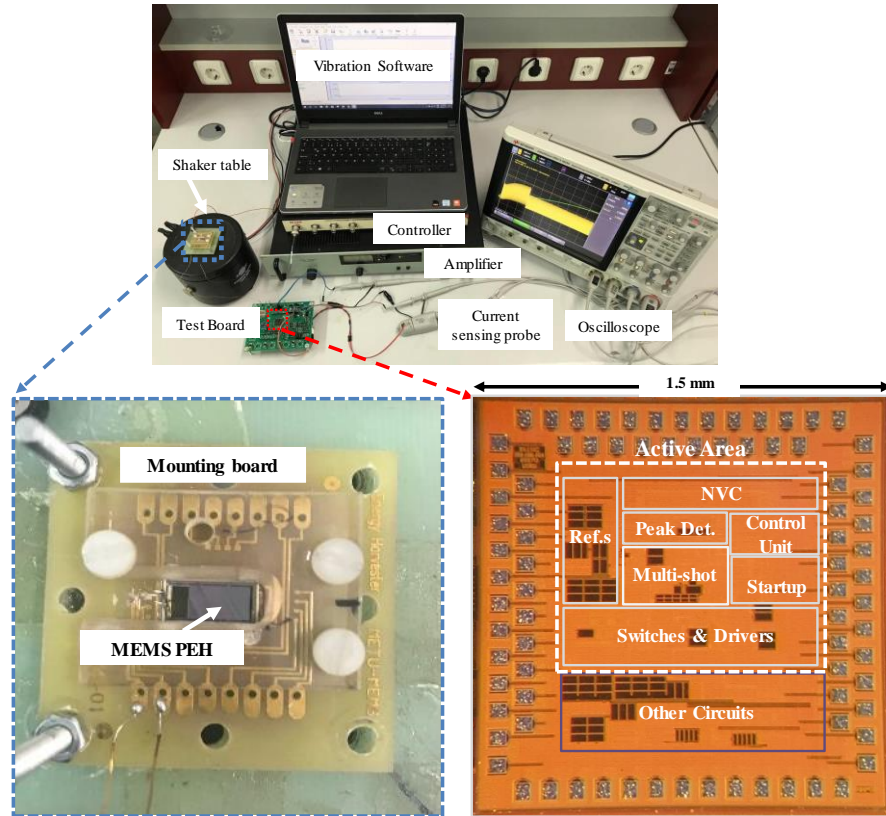


Figure 2.17. Test setup for experiments, based on an IC, test board, and MEMS piezoelectric energy harvester.

Minimum piezoelectric peak voltage of 700 mV is required for operating start-up of the circuit. Figure 2.18 depicts operation of the circuit for an excitation frequency of 390 Hz with 17 μ W input power, and 275 k Ω load resistance. The storage capacitance is initially charged through the start-up circuit. Then energy is extracted from PEH in three-stages ($N=3$). The voltage waveform during charging of the storage capacitor in three stages is shown in Figure 2.18. Figure 2.19 illustrates measured piezoelectric voltage and inductor current waveforms when different number of stages are used in the circuit. The magnitude of the current passing through inductor and switches is divided by the square-root of the number of stages. Consequently, conduction power loss is decreased with the current reduction. As seen in Figure 2.19, there is a harvesting time variation among different number of stages. This variation is partly related to the extraction time duration, $T_{p,n}$ that depends on the number of stages as in equation (2.2). Another variation comes from the difference in storage voltage V_{stor} , which makes charge transfer duration, $T_{s,n}=L \times i_{peak,n}/V_{stor}$, variant. Summing the extraction and transfer durations determines total time, which is distinct for different N .

2.5.1.1 MS-SECE Charge Performance and Power Conversion Efficiency

Initially, the output power extracted within a single stage has been measured as a function of the storage voltage. Figure 2.20 depicts the outcome for several values of V_{OC} . The dependence of the extracted output power on storage voltage is low, as expected, due to SECE technique. Ratio of V_{OC} to V_{stor} affects efficiency at lower storage voltage levels, as it takes longer to transfer energy to storage. Losses due to switching at higher storage voltage is more dominant for lower input power. For lower storage voltage as ratio of V_{OC} over V_{stor} increases, The output power dependence on the storage voltage, V_{stor} , is shown in Figure 2.21 and Figure 2.22 for $V_{oc,pp}=1.5$ V and $V_{oc,pp}=3.5$ V, respectively as the number of stages is varied. Single charge extraction shows the best performance for lower power limit, since excess switching dissipates dramatically higher power especially at higher output voltage. For higher input power, multi-stage extraction increases the output power due to the reduction of conduction losses on switches. Moreover, influence of the multi-stage extraction degrades with

increase of the output voltage due to high switching loss and increase of quiescent current.

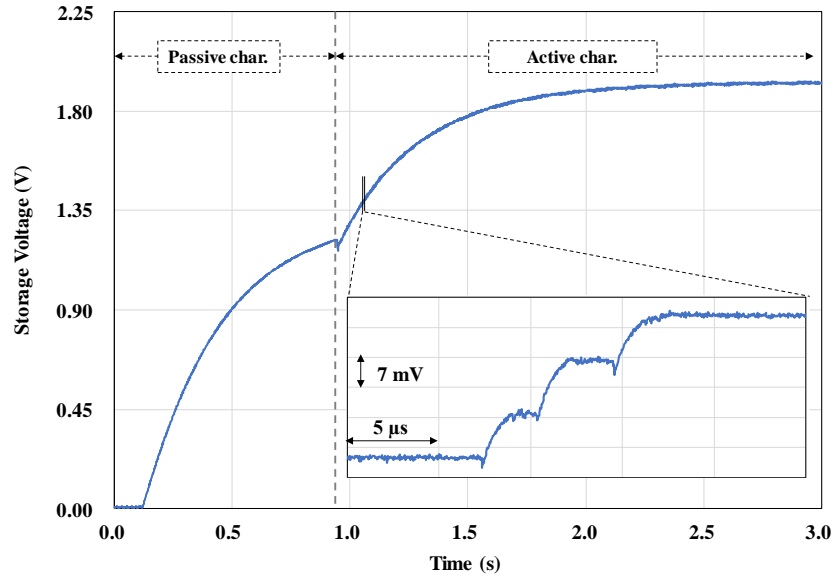


Figure 2.18. Measured input-output waveforms during multi-stage extraction ($N=3$) with highlighted periods for passive and active charging.

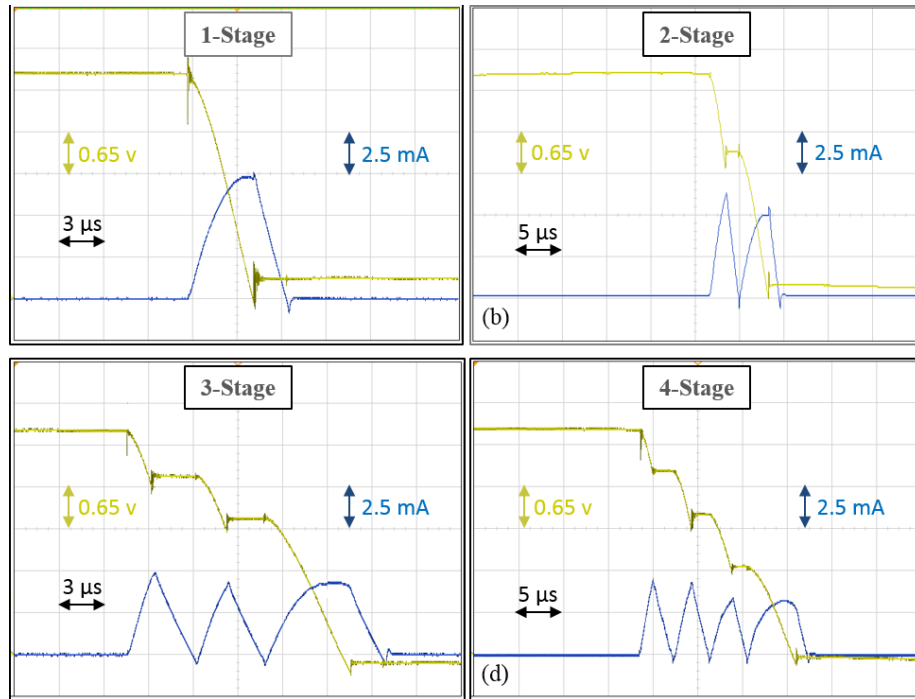


Figure 2.19. Experimental piezoelectric voltage and inductor current waveforms using the multi-stage method: (a) Single stage, (b) two stages, (c) three stages, (d) four stages.

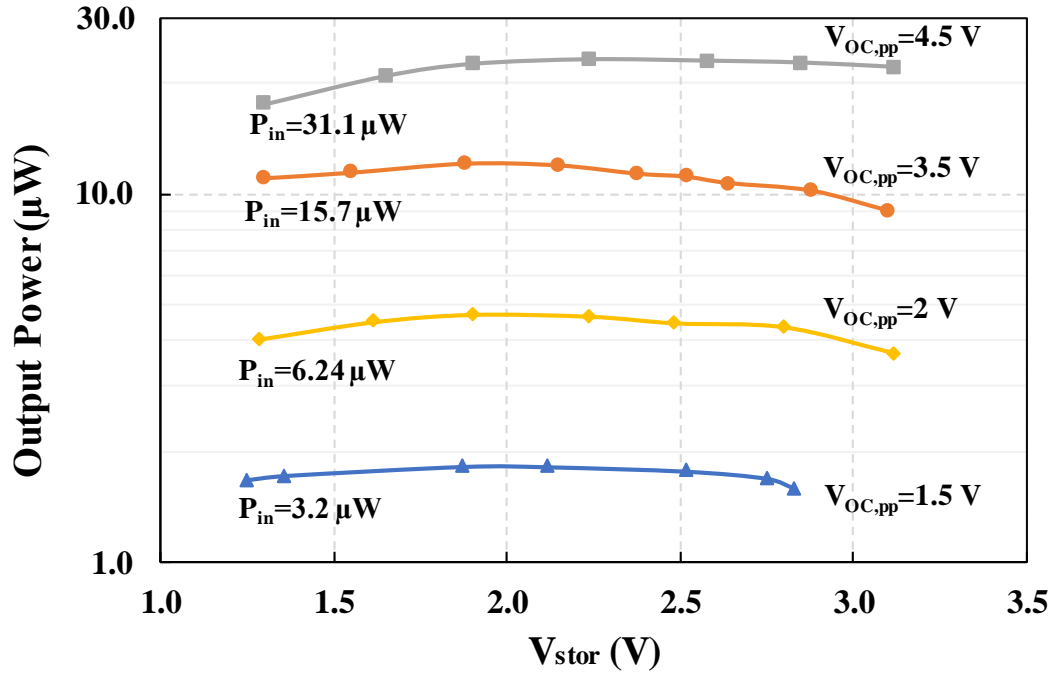


Figure 2.20. Experimental output power vs. output DC storage voltage for four values of V_{OC} with single stage extraction.

The charging efficiency, η , is obtained as ratio of the effective power delivered to the storage capacitance over the average input power. The effective power is calculated as energy increment on the storage capacitance over the charging time, $\frac{1}{2}C_{stor}(V_{Final}^2 - V_{trig}^2)/\Delta t$ where V_{Trig} is the voltage triggering the active extraction. V_{Final} is final stabilized voltage, 3.3 V at which extraction is deactivated. The input power is obtained through measured input voltage and current of the harvester connected to the proposed circuit. Figure 2.23 depicts charging efficiency of the circuit as a function of the piezoelectric open-circuit voltage.

$$\eta = \frac{P_{eff}}{P_{in}} = \frac{\frac{1}{2}C_{stor}(V_{Final}^2 - V_{trig}^2)}{\frac{1}{\Delta t} \int V_{pz} \cdot I_{piezo} \cdot dt} \quad (2.15)$$

It is expected that multi-stage power extraction will improve power efficiency with increasing input power. The maximum power efficiency was measured at 84.4%. As it stands, the optimum stage number can be determined through input power or corresponding open circuit piezoelectric voltage. The power efficiency is maximized for all input power levels when the circuit operates in autonomous manner as shown

in Figure 2.24. The stage number, N is adjusted automatically by N -generator circuit based on input power measurement at the end of the first phase of the extraction.

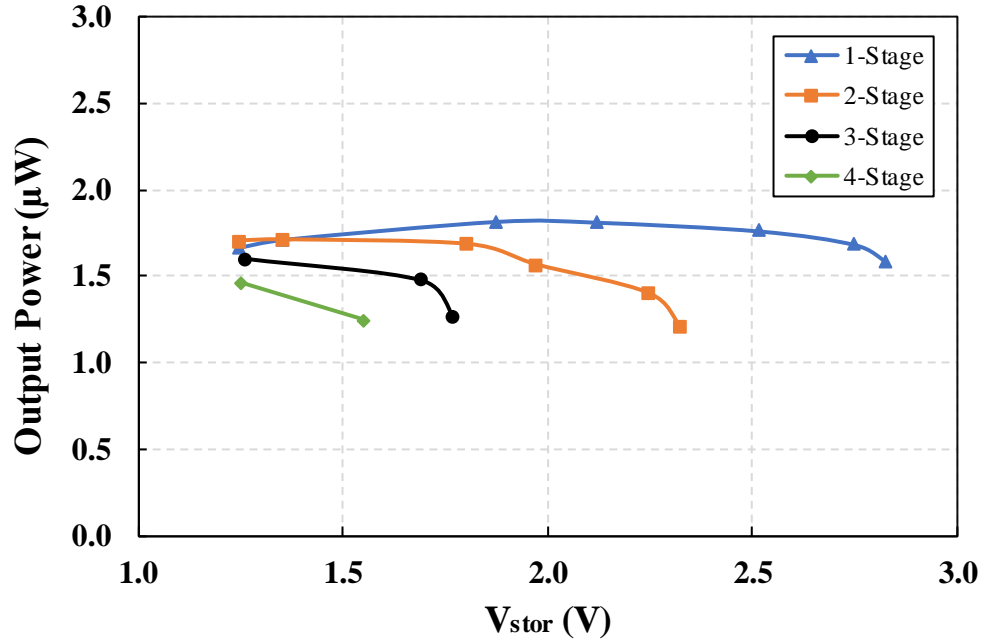


Figure 2.21. Experimental output power @ $V_{\text{OC,pp}} = 1.5$ V for four different staging configurations vs. output DC storage voltage.

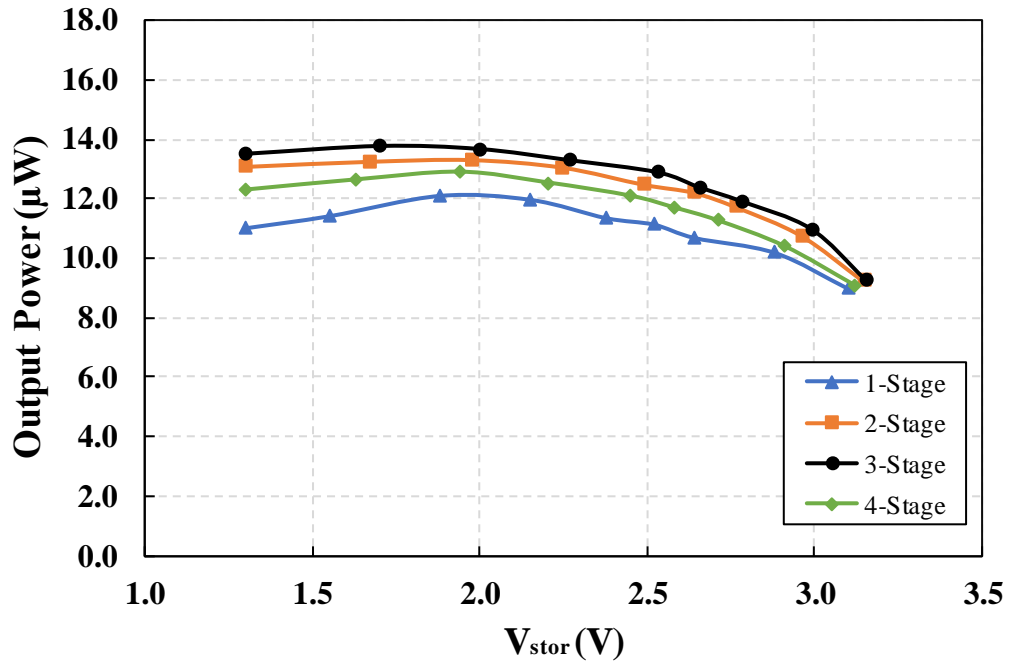


Figure 2.22. Experimental output power @ $V_{\text{OC,pp}} = 3.5$ V for four different staging configurations vs. output DC storage voltage.

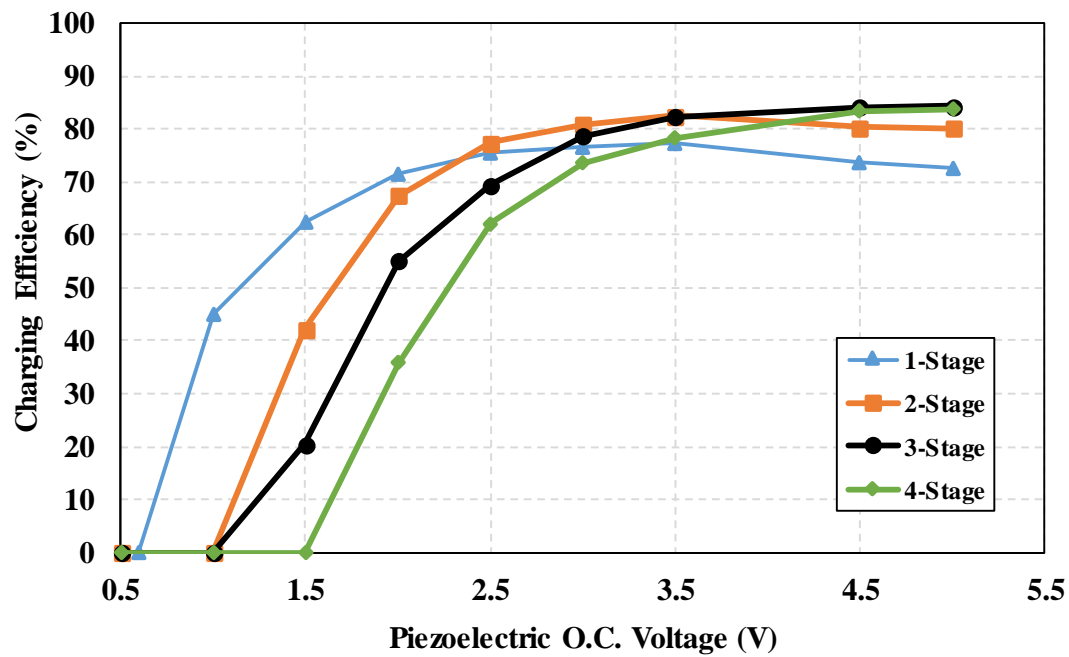


Figure 2.23. Experimental charging efficiency of the IC for four different staging configurations vs. peak-to-peak piezoelectric O.C. voltage.

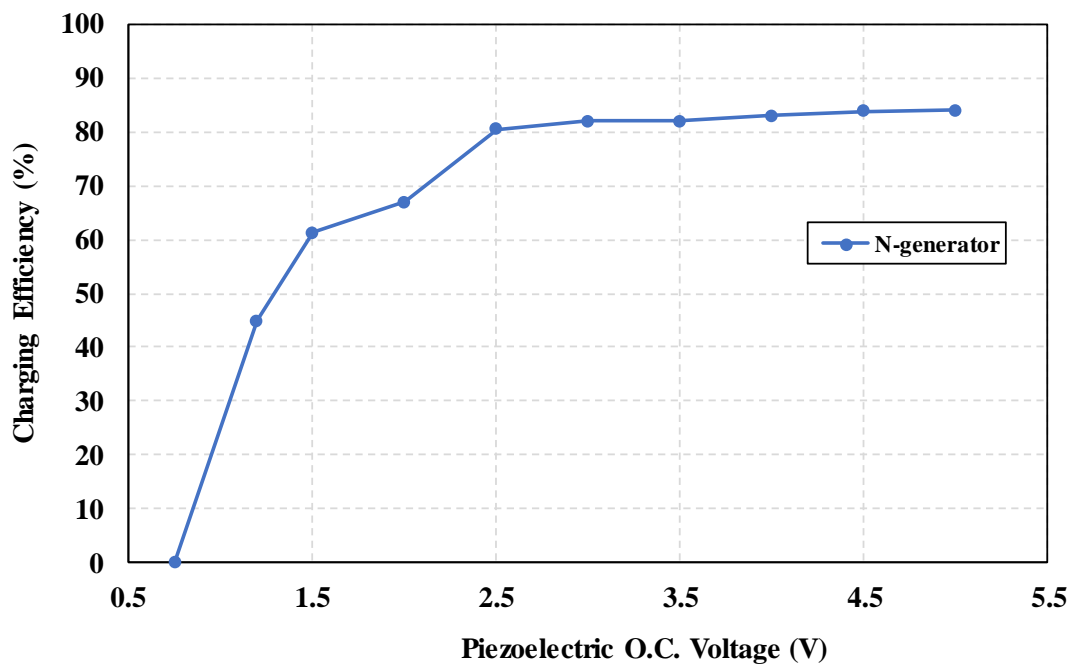


Figure 2.24. Experimental charging efficiency of the IC with automatic stage adjustment vs. peak-to-peak piezoelectric O.C. voltage.

2.5.2 External Inductor

The conversion efficiency of the MSEE circuit is analyzed for different external inductors. The measurements are conducted for available inductors in the market, while PEH is excited at $V_{OC,pp}=4.5$ V and resonance frequency. The features of the external inductors are detailed in Table 2.1. The parasitic resistance of the inductor depends on both inductance and the package size. The variation of the parasitic resistance has a slight effect on conversion efficiency. Figure 2.25 compares the conversion efficiency of the MSEE IC and the SECE as a function of the inductance. As discussed previously, power conversion efficiency increases with the inductor value due to decrease in the current flowing into switches during energy extraction process. MSEE IC can provide higher conversion efficiency using 1mH and 680 μ H inductances in comparison with SECE IC with 10 mH inductance. For inductances above 1 mH, energy extraction process is completed in much longer time as theoretically shown. This leads detecting circuits consume more power and limits conversion efficiency. For inductances lower 330 μ H, performance of multi-stage generator is decreasing due to short oscillation period of the resonance circuit. A compromise between the conversion efficiency and inductor volume points out 1mH inductance.

Table 2.1. Features of the external inductors.

Inductance	Parasitic Resistance	Volume
10 mH	3.9 Ω	12.5mm \times 6mm \times 6mm
3.3 mH	7.3 Ω	8mm \times 8mm \times 6.5mm
1 mH	5.1 Ω	4.8mm \times 4.8mm \times 2.9mm
680 μ H	3.8 Ω	4.8 mm \times 4.8 mm \times 2.9mm
330 μ H	1.8 Ω	4.8 mm \times 4.8 mm \times 2.9mm
100 μ H	12 Ω	3.2mm \times 2.54mm \times 2mm

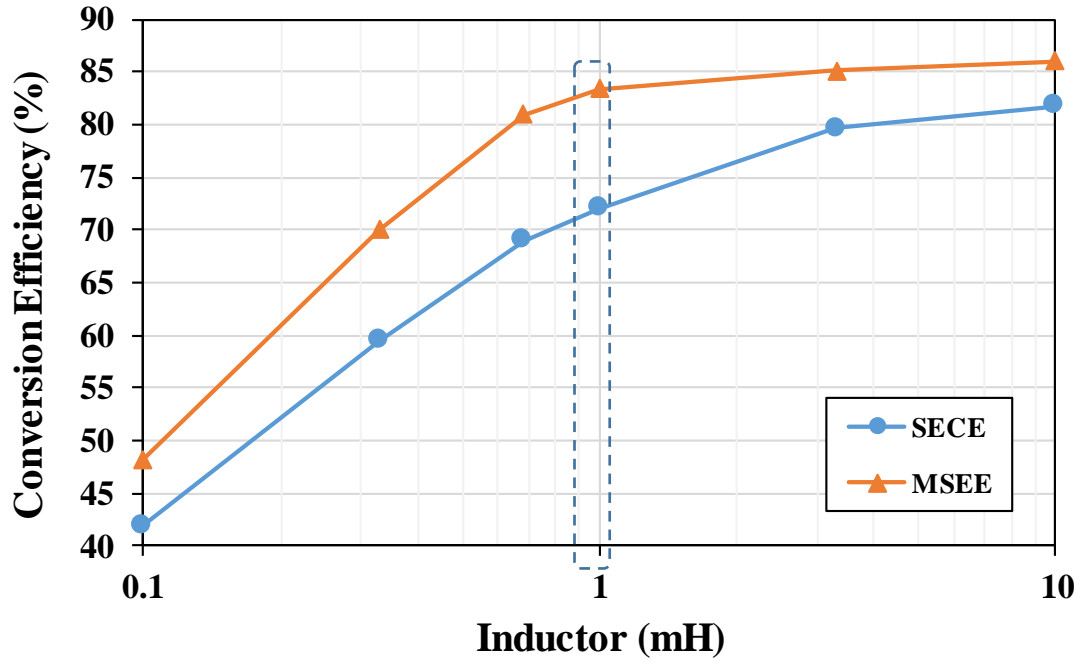


Figure 2.25. Measured conversion efficiency of the MSEE IC and the SECE vs. inductance.

2.5.3 PMC Performance

The overall autonomous IC for PEH, including the PMC and Output capacitance is measured at $V_{OC,pp}=3.5$ V. The harvesting system is tested for charging $C_{OUT}=47$ μ F with $C_{Stor}=1$ μ F. Fig. 9 shows charging the C_{OUT} with no initial charge. As storage voltage reaches to $V_{TH2}=2.4$ V, S_4 is deactivated, and scavenged energy is transferred to the C_{BAT} through switching S_5 . This state continues until V_{Stor} drops down to the $V_{TH1}=1.7$ V. Then, S_5 is turned off, and is charged up again back to the potential of $V_{TH2}=2.1$ V.

The charge performance of IC for $C_{OUT}=47$ μ F has been measured at the same condition with previous experiment where PMC is disabled. Outcomes of two experiments are shown in Figure 2.27. The IC with PMC fastens the charging process of the output capacitance considerably compared with standard SECE IC. The proposed system extract 2.6 time more charges, in other words, 7.5 times more energy respected to standard SECE at the end of 26 second.

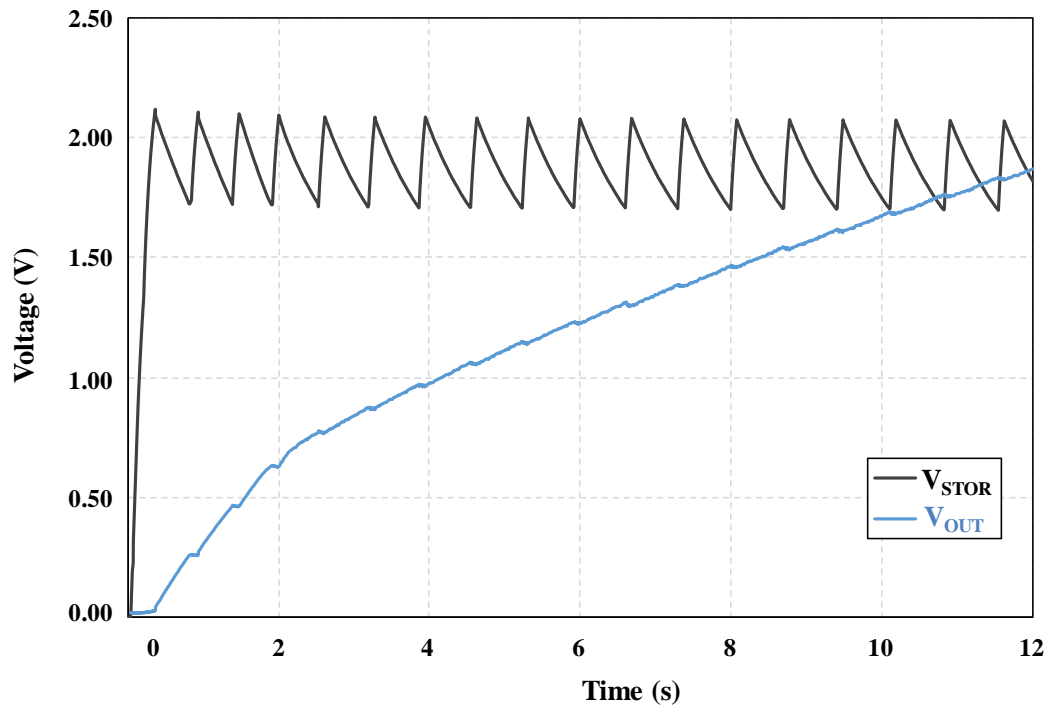


Figure 2.26. Measured storage and output voltages at $V_{OC,pp}=3.5$ V with PMC.

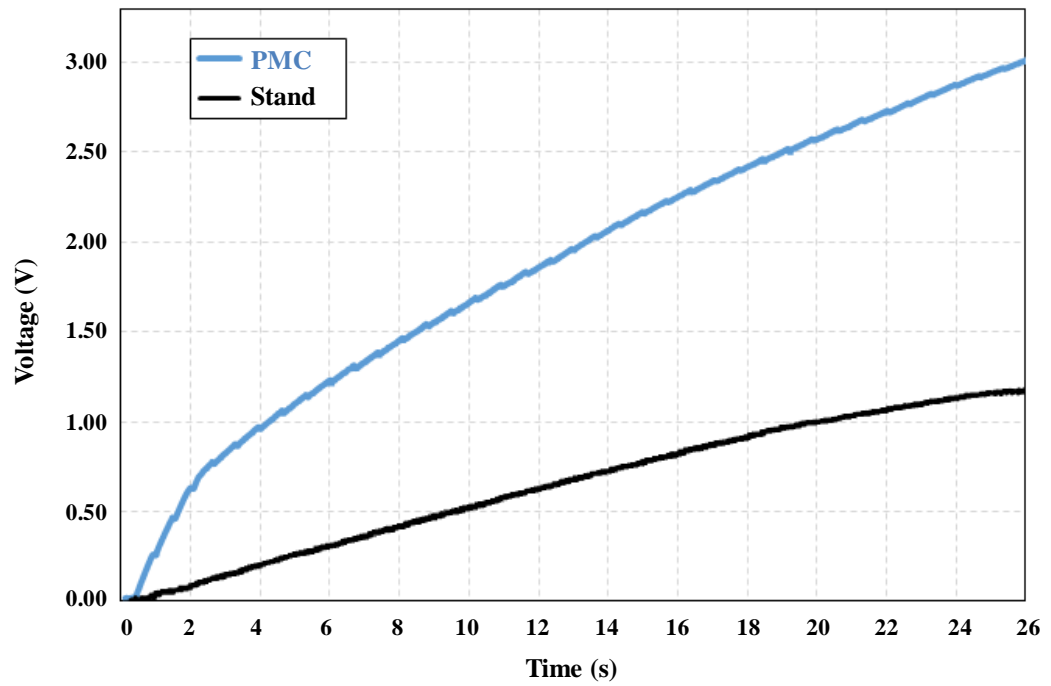


Figure 2.27. Experimentally comparison of charging of output capacitance $C_{OUT}=47 \mu F$ with PMC and standard SECE operation excited with $V_{OC,pp}=3.5$ V.

2.5.4 Frequency Limitation

For analyzing frequency operation range, the PEH is replaced with a sinusoidal voltage source series with 4 nF capacitance, thevenin equivalent of the PEH model discussed in the previous chapter. This way, the excitation frequency can be easily swept for a wide frequency range.

2.5.4.1 Peak detector performance

The maximum operation frequency of the MSEE is determined by the peak detector. A delay in detecting peak instant may cause significant energy loss as the energy transfer is initiated at lower piezoelectric voltage. The accuracy of implemented peak detector has thus been experimentally evaluated as a function of the input frequency. Figure 2.28 shows piezoelectric and peak detector output waveforms for three different excitation frequencies. The accuracy of the peak detector is obtained as $|V_{\text{meas}}|/V_{\text{max}}$, which has been illustrated in Figure 2.29 up to 4,000 Hz, which is the maximum design frequency of the MSEE circuit. Peak point is detected with more than 98% accuracy for excitation frequency range of 20 to 4,000 Hz with $I_{\text{pull-up}}=30$ nA. High accuracy of the peak detector alleviates degradation of the power efficiency due to peak detection latency. The peak point can be detected with higher precision and operation frequency range can be extended by increasing the reference current.

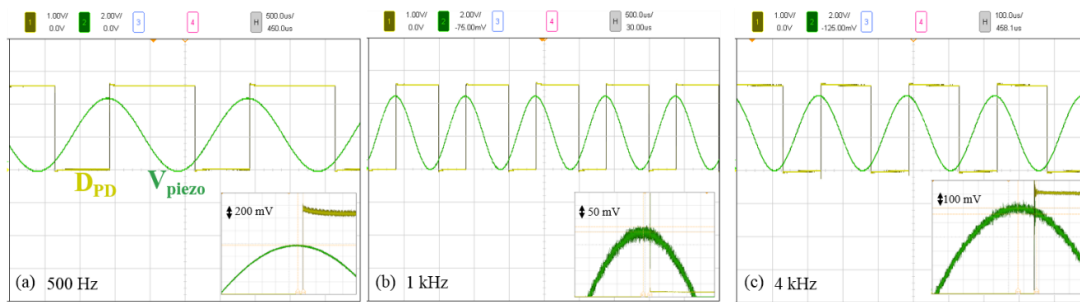


Figure 2.28. Measured input and output waveforms of the peak detector for (a) 500 Hz, (b) 1 kHz, and (c) 4 KHz input frequencies.

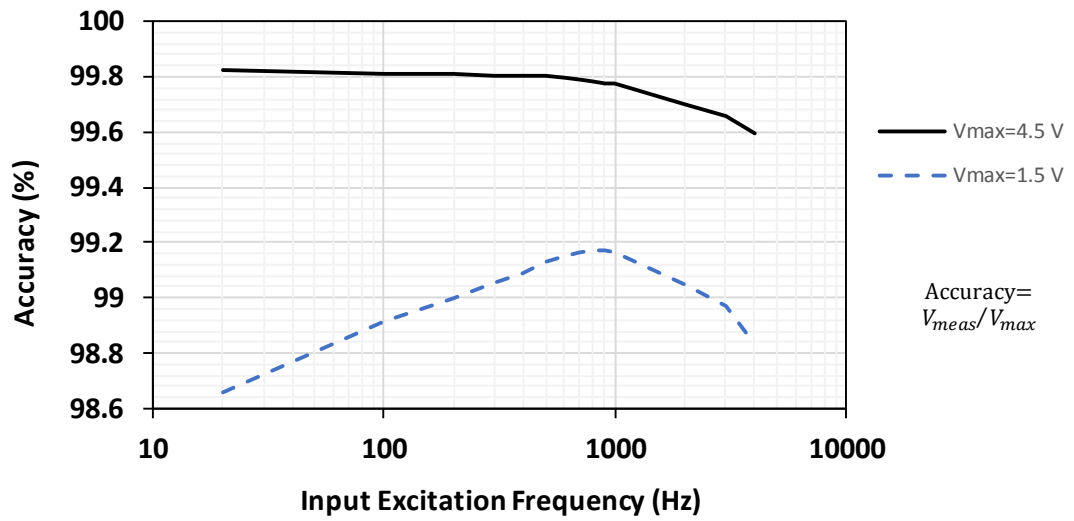


Figure 2.29. The measured accuracy of the peak detector vs. input excitation frequency with 1.5 V and 4.5 V input peak voltages.

2.5.4.2 MSEE performance

The efficiency of the MSEE chip has been measured as a function of the input frequency while peak-to-peak O.C piezoelectric voltage is set to 4V. It is better to notice that voltage amplitude was slightly varying during the sweep of the excitation frequency. The chip efficiency depicted in Figure 2.30 illustrates proper operation for wide range of 20 Hz to 4 kHz. However, the higher efficiencies are achieved for frequencies between 200 Hz and 3 kHz. For frequencies higher than 3 kHz, the performance of the NVC degrades and amplitude of open-circuit voltage decreases. Meanwhile, deactivation of the detectors in extraction period is not more beneficial as the excitation period get closer to the extraction period. For frequencies below 100 Hz, the quiescent current becomes dominant loss and consequently reduces chip efficiency.

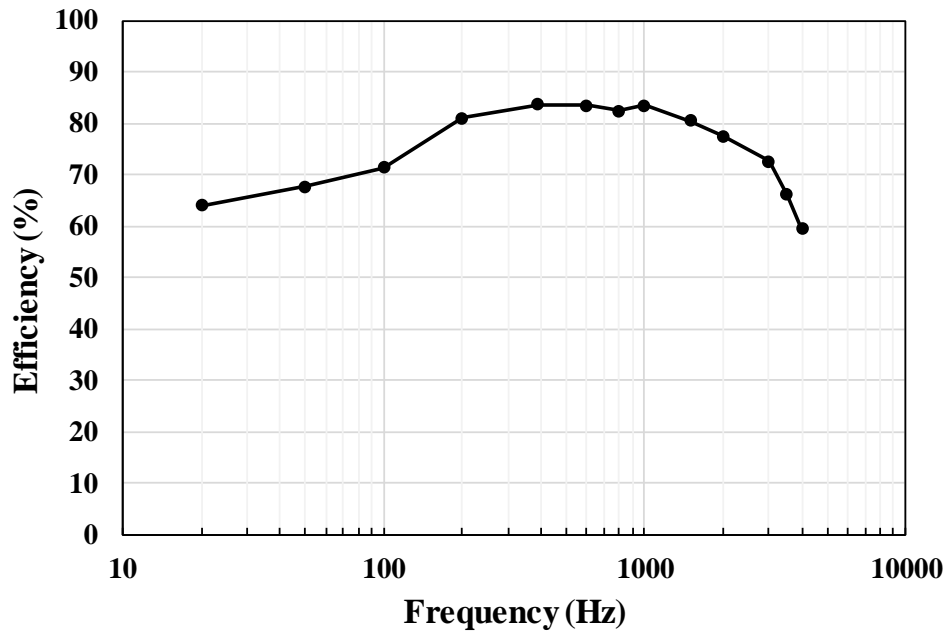


Figure 2.30. Chip efficiency vs. excitation frequency at $V_{OC,pp}=4$ V.

2.5.5 Discussion

Table 2.2 compares the experimental results of the implemented interface circuit with recent integrated SECE converters. The maximum operation frequency of the previous studies has been limited to achieve high conversion efficiency for harvester energy. This has resulted in the use of large piezoelectric harvesters with low resonance frequency, which is not practical in integrated and implantable electronic devices. Additional volume restriction follows from the size of the external inductor. Hehn [62] utilized 10 mH inductor with large package (630 mm^3) to constrain the oscillation current. Dini [63] utilized a $560 \text{ }\mu\text{H}$ inductor in addition to 10 mH to remove residual charge effect. Gasnier [48] used two off-chip MOSFETs in addition to small sized inductor (125 mm^3), however high series resistances of the inductor ($72 \text{ }\Omega$) adversely affected the power conversion efficiency. Our system benefits from both wide frequency operation range that is capable of harvesting energy from MEMS piezoelectric harvesters, and small size inductor (66.8 mm^3). As a result of optimization, minimum dynamic power loss has reduced below $1 \text{ }\mu\text{W}$. The multi-stage extraction circuit has limited oscillation current, while improving the power efficiency to 84.4%.

Table 2.2. Comparison of implemented IC with Other SECE Circuits.

Parameters	Hehn, 2012 [62]	Gasnier, 2014 [48]	Dini, 2016 [63]	This work
Technology	0.35 μm	0.35 μm (off-chip MOSFETS)	0.32 μm	180 nm HV
Static Power loss	< 4 μW	< 1 μW	> 0.4 μW^*	<0.7 μW
Max. input voltage	< 20 V	> 200 V	< 5 V	<12 V
Operation Frequency range	<600 Hz**	<100 Hz**	<100 Hz**	<4 kHz
Excited Frequency	174 Hz	100 Hz	60 Hz	390 Hz
Inductor (Volume)	10mH (630mm ³)	10mH/25uH (125mm ³)	10mH/560uH (-)	1 mH (67mm³)
Max. Efficiency	85%	61%	85.3%	84.4%
Output. Power @Max. Eff.	@ $V_p=12.8\text{V}$ 477 μW	@ $V_p=40\text{V}$ 560 μW	@ $V_p=4.7\text{V}$ 51.33 μW	@ $V_p=4.75\text{V}$ 78 μW

* Equivalent Static power loss estimated from reported quiescent current.

** Frequency range estimated from reported efficiency limitations.

As a conclusion, the basic structure of the SECE converter was precisely analyzed. Then, a novel multi-stage energy extraction method was proposed to optimize implementation of the SECE converter. The circuit optimization allows reducing the value of the external inductor without affecting the power-conversion efficiency. Besides, a charge management approach was presented to fasten the charge speed of huge-size storage element. The advantage of this method is that accelerates the transition from passive mode to active mode. In the circuit level, several circuit techniques were implemented to enhance practicability of the IC: i) start up circuit to achieve autonomous system, ii) Active NVC and ultra-low power peak detector to extend operation frequency range, iii) self-adapting multi-shot generator that enhances power conversion efficiency for wide input power range.

The SECE converter is a proper candidate for implementation of energy harvesting electronic devices. Although presented MSEE circuit steps up the practicality of the SECE converter, there is room to investigate other switching techniques from the power aspect. The following chapter introduces new switching architecture looking into the power-extraction enhancement of low-coupled PEHs.

CHAPTER 3

IC FOR PEHS DESIGN II: SELF-ADAPTING OPTIMAL DSSH

Aside from MSEE IC, a novel synchronized switching technique is developed for low-coupled PEHs during this Ph.D. study. As discussed in Chapter 1, the main advantage of the SSHI is the power-extraction enhancement in comparison with standard rectifiers. However, the major drawback of the SSHI circuits is that power gain is achieved in the limited range of the excitation level and the connected load. On one hand, SECE provides load independent power extraction and is efficient for low-coupled PEHs such as MEMS PEHs. The aim of this framework is to integrate a load-independent IC to boost extracted power from low-coupled PEHs. The idea is to take advantage of the synchronized switching process of both the SECE and the SSHI techniques with a single inductor. The proposed topology called “double synchronized switch harvesting (DSSH)” which introduces new switching process on piezoelectric transducer. A novel MPP sensing approach is proposed to achieve optimal operation point of the proposed circuit regardless of input excitation level, for the first time in literature. Several sensing circuits presented in this chapter address challenges in tuning exact time of charge inversion and MPP for variable vibrations. Self-adapting DSSH fundamentals is introduced in the first section. Section 2 provides circuit implementation details. Design validation results follow in Section 3 from a fabricated test chip. Finally, achievements from this work are discussed.

3.1 Self-adapting DSSH IC

3.1.1 *Concept and Operation Principle*

Recycling or investing charge on piezoelectric material to increase damping force is essential to increase extracted power. Energy recycling can be realized through

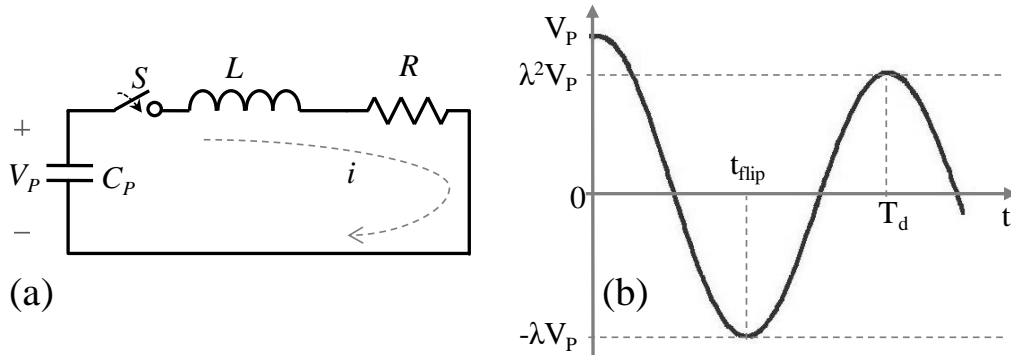


Figure 3.1. (a) RLC resonant circuit established in charge flipping, (b) capacitor voltage

flipping charge on piezoelectric capacitance, C_P , as a result of establishing a resonant circuit between C_P and an external inductor, L . The energy stored in C_P is transferred to the inductor, and back to the capacitor to flip the capacitor voltage to $-\lambda V_P$. The efficiency of charge flipping is mainly constrained by the quality factor (Q) of the RLC, and the topology of the harvesting circuit. Figure 3.1 shows an RLC resonant circuit, where R stands for the parasitic resistance along the loop comprising of the parasitic resistance of the inductor (L), and the switch. The Q factor and damped resonant frequency of the path are given as:

$$Q = \frac{1}{R} \sqrt{\frac{L}{C_P}} \quad (3.1)$$

$$\omega_d = \sqrt{\frac{1}{LC_P} - \frac{R_s^2}{4L^2}} \quad (3.2)$$

Let us consider that the initial value of the capacitor is V_P and the switch S is closed at $t = 0$. The fraction of voltage conserved on the capacitor of an RLC oscillator with quality factor Q is $\lambda = e^{-\frac{\pi}{2Q}}$ after half cycle of damped resonance period. Indeed, the capacitor voltage flips with λ factor within time $t_{flip} = \frac{\pi}{\omega_d}$. As Q rises, λ gets closer to one; and so does the efficiency of the SSHI circuits. The proposed circuit uses charge-flipping technique to recycle optimum charge into the piezoelectric capacitance, which enables significant improvement in energy extraction from the harvester.

Figure 3.2 shows a model for the proposed IC. The non-linear processing circuit is only composed of an inductor L in series with electronic switches S_1 , S_2 and in parallel with an energy transfer switch S_3 . The piezoelectric harvester is simply modeled by an alternating current source in parallel with a capacitance of the piezoelectric material (C_P) to illustrate piezoelectric behavior and circuit operation as shown in Figure 3.3. Figure 3.3(a) depicts the waveforms for mechanical displacement, piezoelectric voltage, V_{PZT} , and inductor current, I_{IND} . Figure 3.3(b) presents the operation phases of the switching circuit for an excitation cycle. (i) Initially, positive charge is generated on piezoelectric capacitance, as harvester current is positive, which represents upward strain on piezoelectric material. In this case, S_1 is ON to connect V_N node to ground, while S_2 is OFF to block current flow into the inductor. (ii) S_2 switch turns ON when the mechanical displacement reaches its peak value. At this time, an oscillating electrical circuit $L-C_P$ is established and S_2 switch is turned OFF after half an electrical period, resulting in the inversion of the peak voltage, $V_{PN}=-\lambda V_2$, called charge flipping. (iii) Turning S_1 OFF while S_2 is ON starts negative charge generation phase by pushing charge to the V_N node from the inductor, and harvester negative current starts to charge C_P in opposite direction. (iv) Energy extraction is realized at minimum mechanical displacement by turning S_1 and S_2 ON. (v) A portion of the generated energy is extracted into the inductor, after which point the circuit closes S_1 and opens

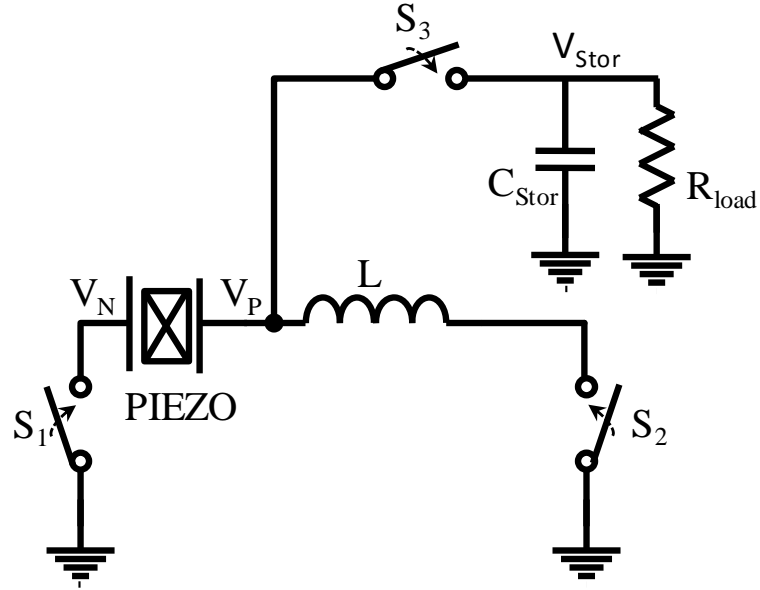
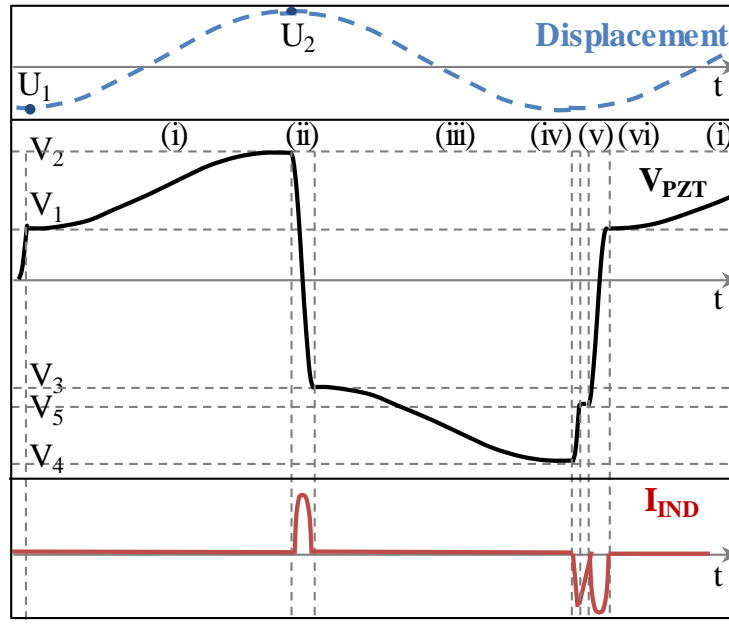
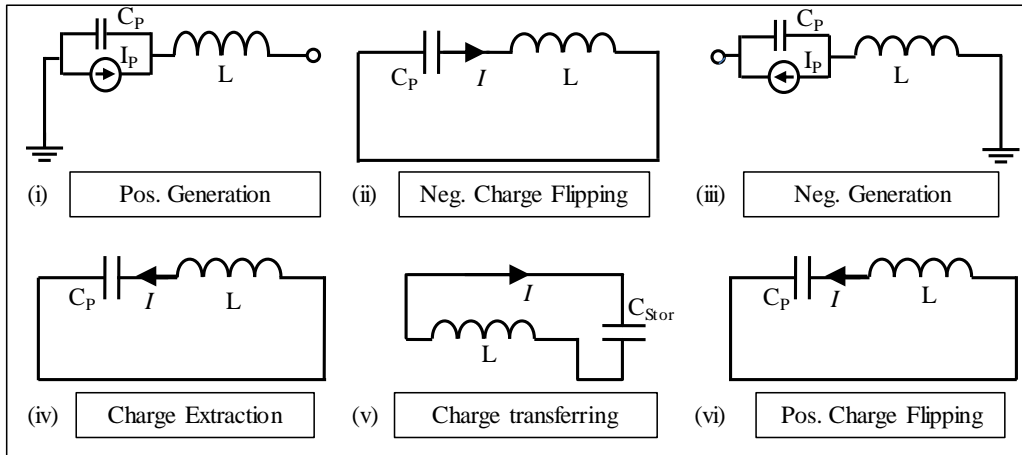


Figure 3.2. Schematic of proposed circuit.



(a)



(b)

Figure 3.3. (a) Representing voltage and current waveforms corresponding to (b) operation phases of the proposed switching circuits.

S_3 to deliver the energy to the output capacitor. As inductor current crosses the zero point, S_3 is turned OFF to block current flow back. (vi) The remaining generated energy is recycled into piezoelectric capacitor through positive charge flipping by turning both S_1 and S_2 ON. At the end of charge cycle, the circuit goes back to positive charge generation, and initiates the next cycle.

3.1.2 Optimal Energy Transfer with Constant Vibration Magnitude

Extraction charge ratio, α , is defined to determine the values of the charge extracted, $\alpha C_p V_4$, and recycling charge in each period, $(1-\alpha)C_p V_4$, where V_4 indicates the voltage accumulated at minimum mechanical displacement. The maximum energy extraction can be achieved by tuning α . The proportion of voltage left on the capacitor C_p after discharging is a control parameter adjusted by the S_1 and S_2 switches. The optimum point depends on the Q factor of charge flipping path, which in turn depends on piezoelectric capacitor, external inductor as well as inductor and path resistance.

Let V_1 be the voltage on C_p just after charge flipping has occurred, and harvester starts generating charge on C_p in positive direction. Since no current flow in generation phases, the amplitude of the piezoelectric voltage can be obtained through second equation of piezoelectric macroscopic equations (1.2) using $I=0$:

$$V_{oc} = \frac{\Gamma}{C_p} 2U_m \quad (3.3)$$

where $U_m=(U_2-U_1)/2$ is average of full swing of the beam at steady state condition. $V_2=V_1 + V_{oc}$ is the accumulated voltage before charge flipping to negative voltage. Previously, λ is defined as the fraction of the voltage magnitude left after the charge flipping takes place, so the magnitude of the voltage after the flipping is $V_3=-\lambda V_2$. V_4 is minimum voltage generated at negative generation phase, and V_5 is the voltage left on C_p after the discharge takes place, such that $V_5=\alpha V_4$. Then,

$$V_3=-\lambda(V_1+\frac{2\Gamma}{C_p}U_m) \quad (3.4)$$

$$V_4=V_3-\frac{2\Gamma}{C_p}U_m \quad (3.5)$$

$$V_5=\alpha V_4 \quad (3.6)$$

$$V_1=-\lambda V_5 \quad (3.7)$$

Substituting for V_5 from equation (3.6) into (3.7) and then for V_1 from equation (3.7) into (3.4) eliminate two variables. Lastly, steady-state value of V_4 is derived from solving equations (3.4-3.5) as:

$$V_4 = \frac{1+\lambda}{1-\alpha\lambda^2} \times \frac{\Gamma}{C_p} 2U_m \quad (3.8)$$

The extracted energy per cycle on the capacitor during discharge is:

$$E = (1 - \alpha^2) \frac{1}{2} C_p V_4^2 \quad (3.9)$$

The transferred energy to the storage is not affected by the extracted energy; thus efficiency of this step is ignored here. Substituting for V_4 from equation (3.8) into equation (3.9) gives the extracted energy as a function of excitation level.

$$E = 2(1 - \alpha^2) \left(\frac{1+\lambda}{1-\alpha\lambda^2} \right)^2 \times \frac{\Gamma^2 U_m^2}{C_p} \quad (3.10)$$

Differentiate E with respect to α to calculate the value of α that results in maximum E :

$$\frac{dE}{d\alpha} = 0 \quad (3.11)$$

The value of extraction ratio that optimizes charge extraction is $\alpha=\lambda^2$, giving the maximum extractable energy from the harvester as:

$$E_{max} = 2 \frac{(1+\lambda)^2}{1-\lambda^4} \times \frac{\Gamma^2 U_m^2}{C_p} \quad (3.12)$$

Compared to the ideal full-bridge rectifier, this is a significant gain of $\frac{E_{max}}{E_{ideal,FB}} = 2 \frac{(1+\lambda)^2}{1-\lambda^4}$. Therefore, even a moderate Q provides a significant extracted energy gain.

The problem is hence reduced to finding this optimum point in circuit implementation.

3.2 Circuit Implementation

Figure 3.4 shows the proposed circuit utilizing an external inductor, L , and a storage capacitor, C_{stor} . The power switches are implemented with thick-oxide 12 V MOSFETs to tolerate high voltage swing on their terminals. Minimizing conduction loss at power switches plays a significant role in achieving higher Q . Widths of the power switches are set to $W_{S1,2}=30$ mm and $W_{S3}=12$ mm, which represent compromise

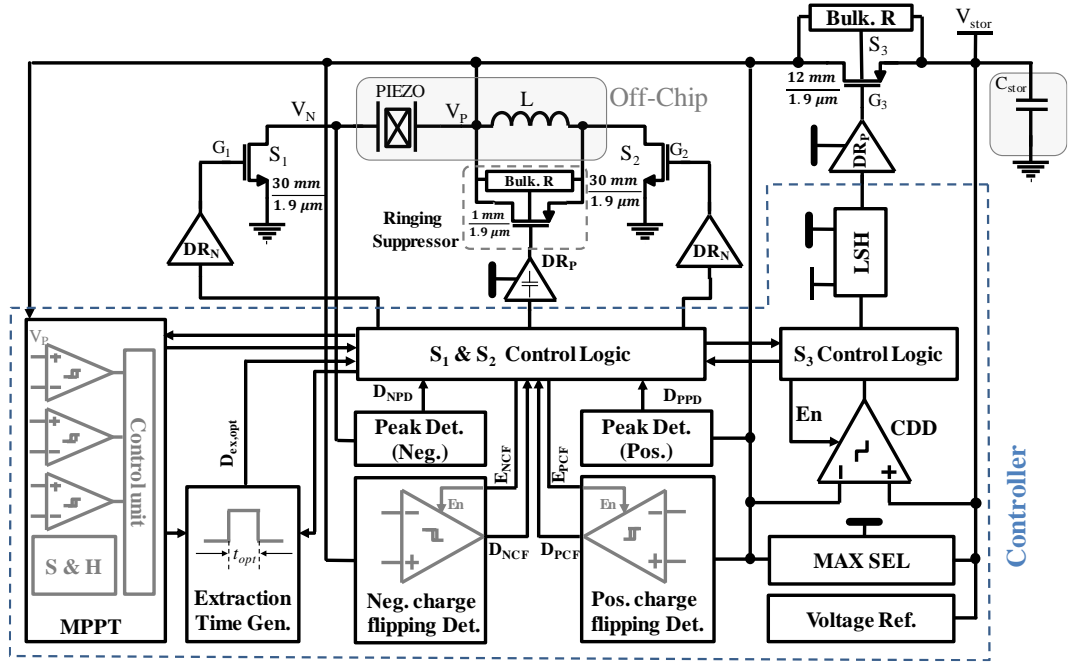


Figure 3.4. Implementation of proposed optimal SSHI-SE IC.

between switching losses due to gate-source capacitance and conduction losses due to ON resistance. Two major design objectives of the proposed circuit are accuracy and minimization of power dissipation, and the building blocks are designed towards these objectives.

3.2.1 Peak Detectors

Figure 3.5 shows configuration of the proposed peak detector utilized to sense both positive and negative peaks with corresponding connections in the core circuit. The circuit operates in current mode to accommodate PEH voltages higher than its supply voltage. The input voltage is converted to current by a series capacitor, C_{PK} , in conjunction with internal negative feedback. With increasing piezoelectric voltage, the sensed current, I_s charges node V_X up to M_{N0} threshold voltage. The feedback through M_{P0} prevents further increase at V_X . As PEH voltage peaks, I_s reaches zero, and charge dissipation at node V_X by M_{P0} turns M_{N0} OFF. Voltage at node V_Y increases due to mirroring of the bias current. Common source amplifier and digital inverter at the output stage deliver a high edge rate. The bias current and the series capacitor values

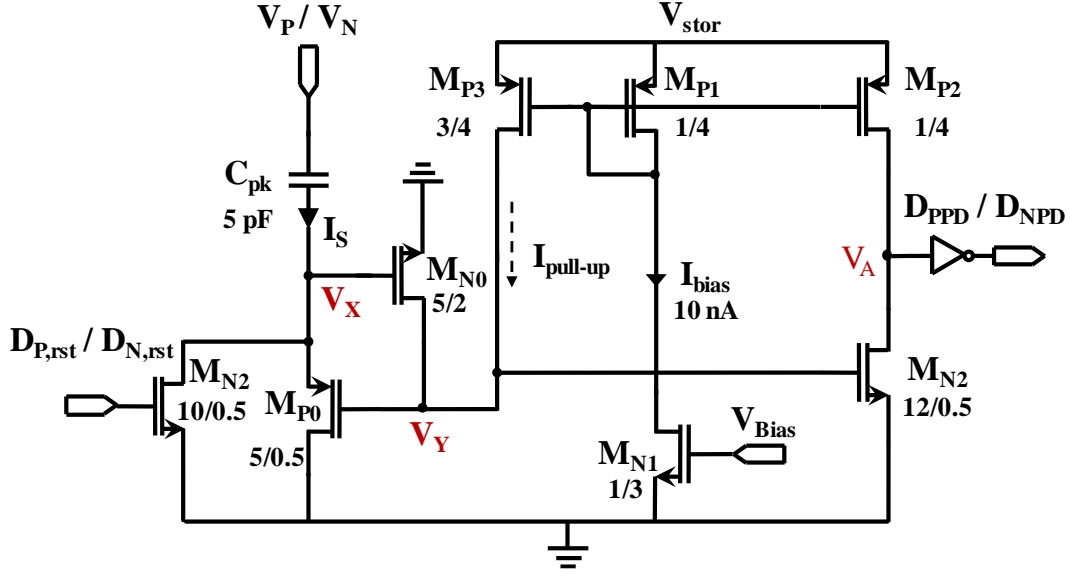


Figure 3.5. Schematic of the implemented Peak Detector.

determine the upper limit of the input frequency and the minimum detectable amplitude, respectively. Details of this peak detector circuit have been reported in [67] with simulation and experimental results.

3.2.2 Charge Flipping Sensor

The charge flipping action is accomplished when all charge transferred to the inductor flows back into the piezoelectric capacitance, C_P . The circuit presented in Figure 3.6(a) detects the depletion point by sensing the current that piezoelectric voltage induces on the C_{Sens} capacitor. The voltage-current conversion is realized using a flipped voltage follower (FVF) circuit that provides low input impedance and low input voltage requirements with the feedback connection of M_1 and M_3 at the drain of M_1 . This circuit retains a roughly constant voltage at V_C node. The sensed current, I_{sens} , plus bias current, I_{bias} , replicated at PMOS M_1 - M_3 through a current mirror, establish the sensed voltage V_S across resistor R_S in proportion to the sensed current. V_S is compared with offset voltage, V_{ref} , generated with mirrored bias current across the reference resistor, $R_{red}=R_S$. While the current on the external inductor flows into the piezoelectric capacitance C_P , higher voltage at the inverting input of the comparator keeps previous state of the comparator. Just as no energy remains to drain from the external inductor,

the current flowing into C_S becomes zero, and eventually the voltage established at R_S falls below V_{os} that changes the state of the comparator from low to high as shown in Figure 3.7. The positive charge flip is similarly detected with the circuit shown in Figure 3.6(b).

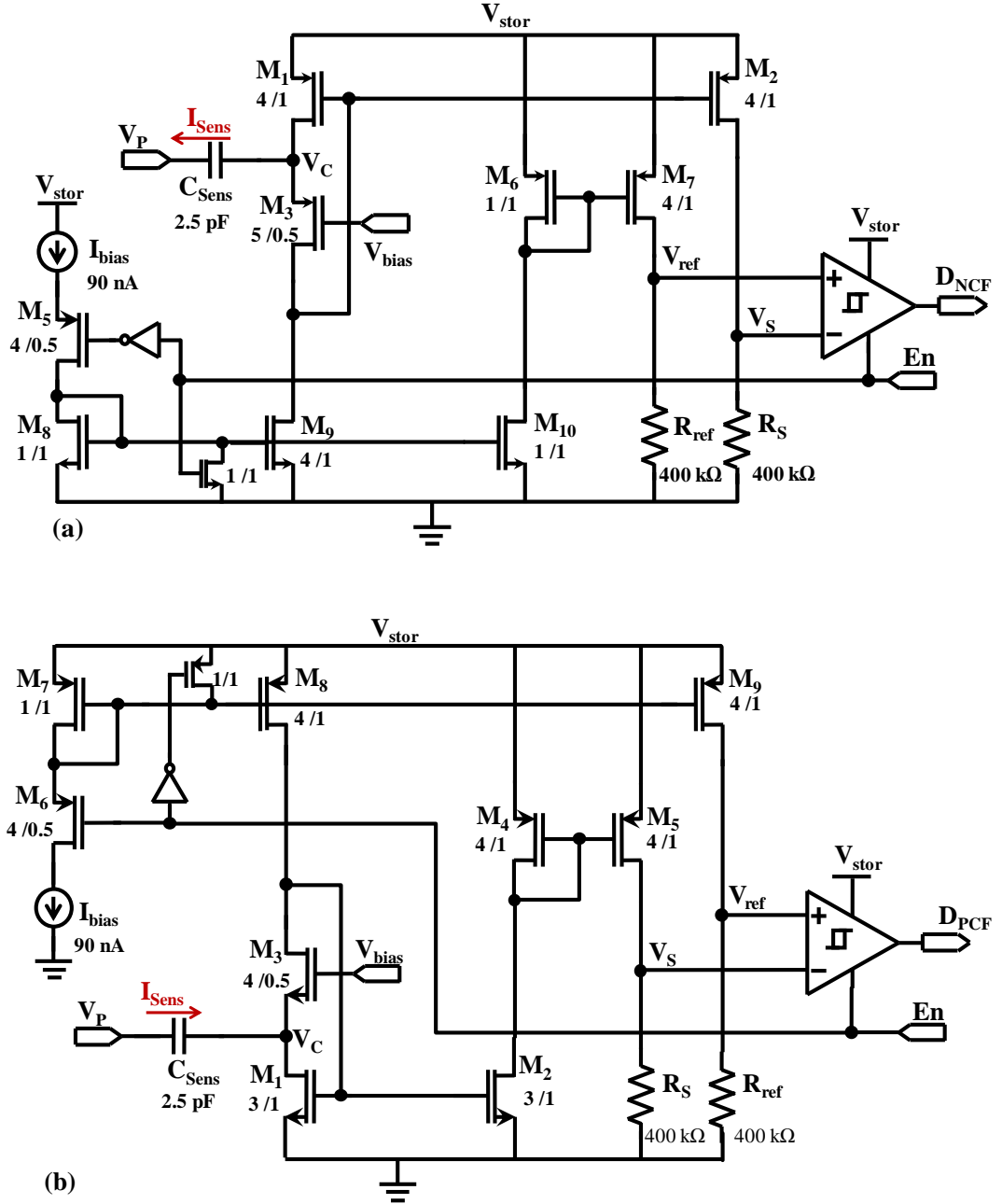


Figure 3.6. Schematic of (a) negative charge flipping sensor, and (b) positive charge flipping sensor.

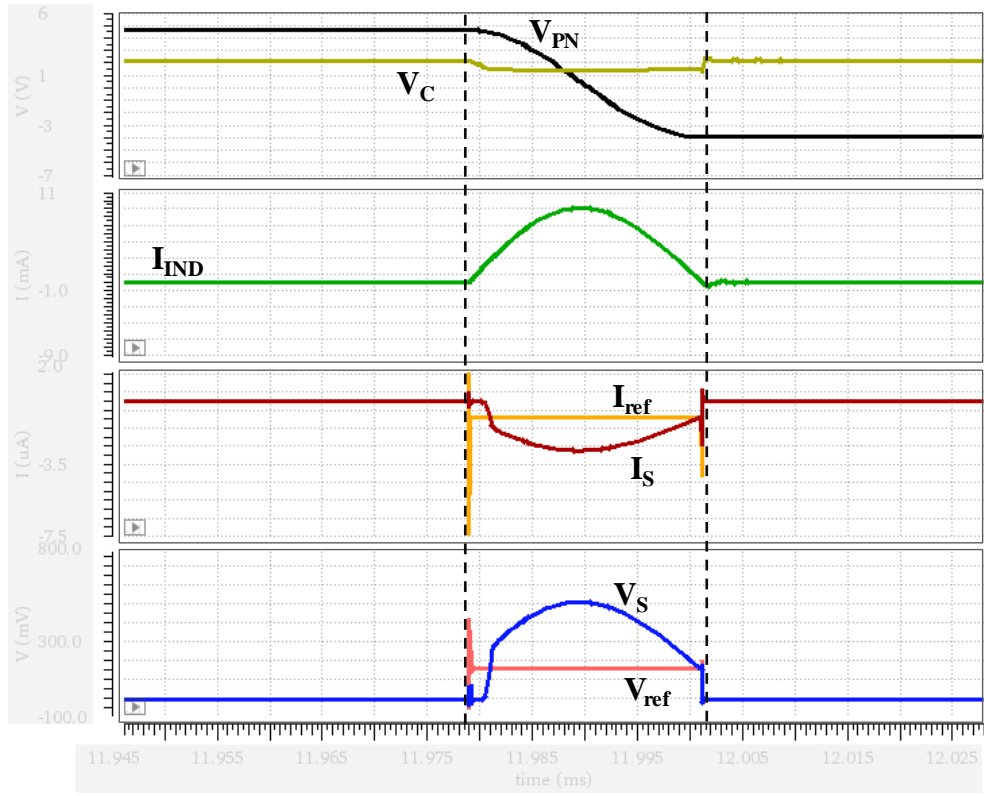


Figure 3.7. Simulated current and voltage waveforms of negative charge flipping sensor

3.2.3 Extraction Time Generator

Extraction time generator, implemented as shown in Figure 3.8, saves optimum extraction time in MPPT mode and regenerates it each cycle in operation mode. During MPPT mode, D_{OPT} turns M_{P1} switch ON to allow reference current flows through M_{P1} into C_{opt} to set the optimum extraction time as a reference voltage, V_{OPT} . In extraction mode, when negative peak detector's output goes high, control unit initiates rising edge of $D_{ex,opt}$ pulse and closes switch M_{P2} to steer reference current into C_{HARV} . The generated ramp voltage, V_{HARV} , is compared with V_{OPT} , corresponding to the optimum extraction time, to reset SR latch and generate falling edge of the extraction time signal. Then, C_{harv} is discharged through M_{N2} MOSFET to reset for the next cycle.

3.2.4 Charge Depletion Detector

Depletion of extracted energy from the inductor to the storage capacitance is controlled by a charge-depletion comparator with a relatively high bandwidth. A conventional

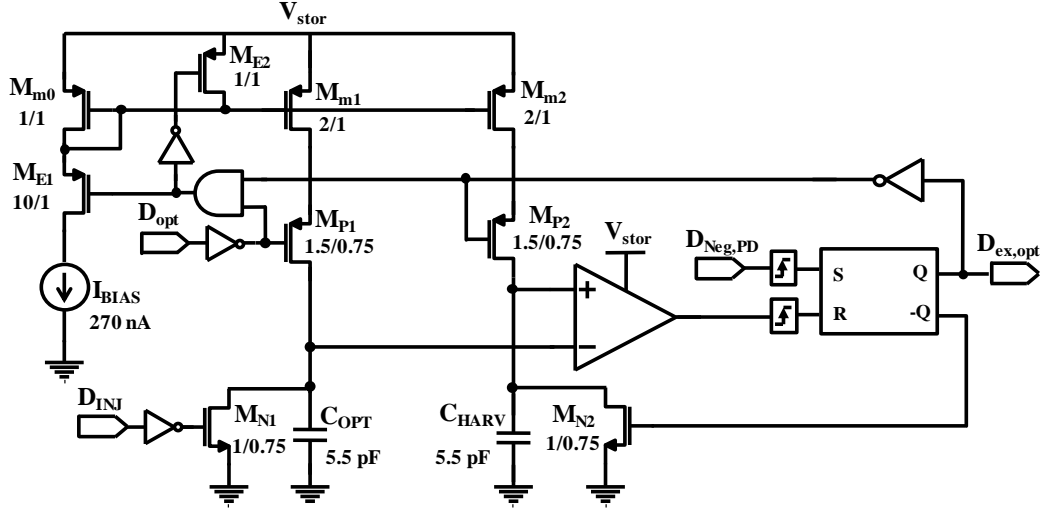


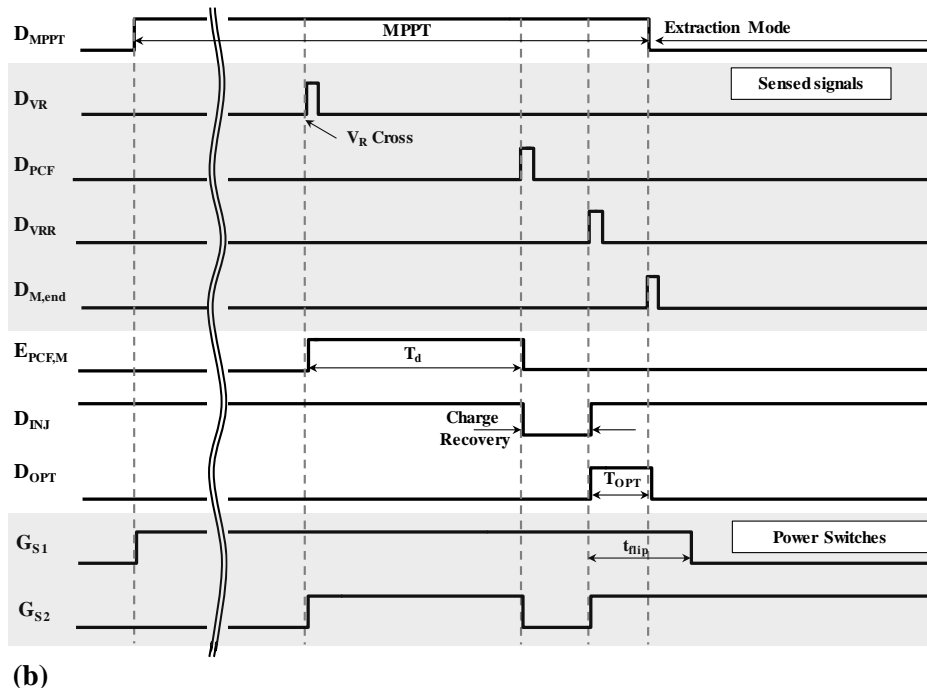
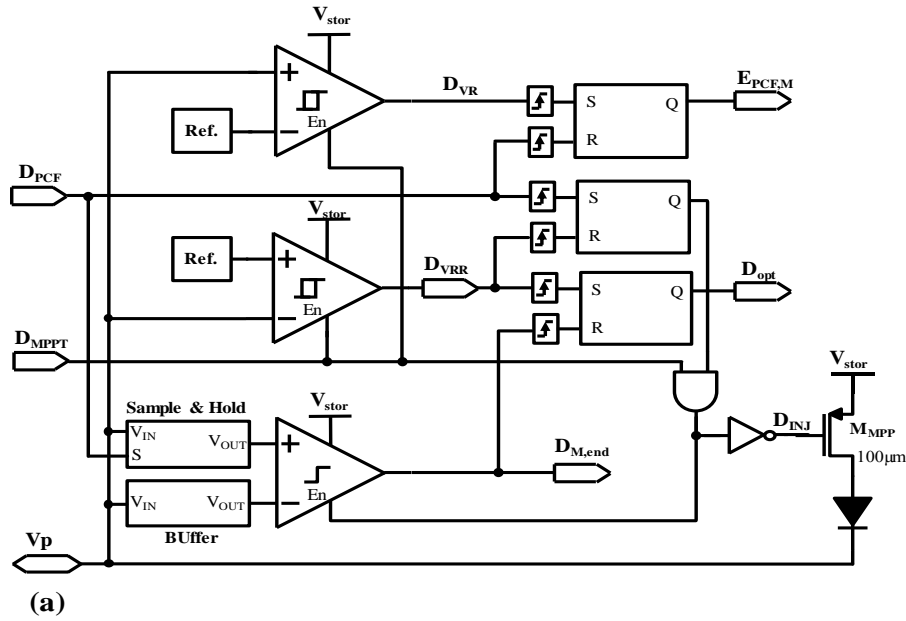
Figure 3.8. Schematic of implemented extraction time generator.

two-stage comparator monitors the voltage across S_3 switch to detect the end of inductor energy discharging. The control unit activates the CDD only in charge transferring phase to compromise between power consumption and comparator bandwidth. The output signal of the CCD ends the charge transferring and initiates charge-flipping phase as shown in Figure 3.3.

3.2.5 MPPT Circuit

The optimum extraction time is achieved as $t_{ex,opt} = \frac{1}{\omega_d} \cos^{-1}(\lambda^2)$, corresponding to optimum charge extraction ratio $\alpha = \lambda^2$ and C_p voltage during extraction phase, $V_5 = \lambda^2 V_4 = V_4 \cos(\omega_d t_{ex,opt})$. This leads to a method to identify the MPP by measuring optimum extraction time, $t_{ex,opt}$. Figure 3.9 illustrates the schematic of the MPPT circuit with corresponding signal waveforms. The proposed MPPT circuit enables the piezoelectric voltage to reach a reference voltage level, V_R . At this point, S_1 is ON and S_2 turns ON to establish the resonant circuit. After one cycle of resonance period, T_d , λ^2 of initial voltage, V_R , is conserved on C_p as a result of damping. This point is detected by positive charge flipping sensor, and piezoelectric voltage, $\lambda^2 \times V_R$, is sampled and held for comparison in the next step. Then, S_2 turns OFF. Charge is injected into C_p from storage devices through a control switch and a diode to recover

piezoelectric voltage to V_R . At this moment, S_2 closes to establish the resonant circuit once more with the same initial voltage on C_P . The transient piezoelectric voltage is compared with sampled voltage to determine optimum extraction time corresponding to λ^2 . The measured pulse, T_{opt} , is saved by time generator circuit to reproduce in operation mode.



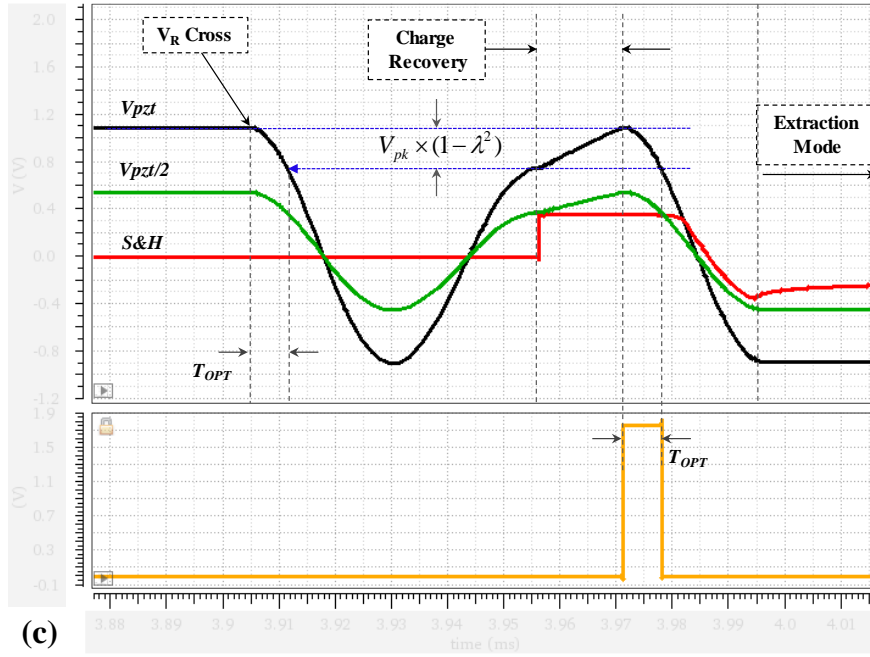


Figure 3.9. (a) MPPT circuit and corresponding (b) digital and (c) simulated analog signal waveforms.

After finding the MPP in a cycle, the system initiates harvesting operation mode and switching is executed as defined previously. All phases of sensing the MPP are completed over one cycle of the mechanical vibration. Besides, excitation level and frequency do not affect the MPP. As result, the IC provides maximum power extraction, independent of input vibration.

3.3 Design Validation

The SA-DSSH circuit is fabricated in 180 nm HV CMOS technology with $900 \mu\text{m} \times 600 \mu\text{m}$ active area. Experimental setup, evaluation board and microphotograph of the chip are depicted in Figure 3.10. An external $L=3.3 \text{ mH}$ inductor with 5Ω series parasitic resistance and a $1 \mu\text{F}$ storage capacitor are connected to the circuit. A 103YB cantilever PEH from Piezo System has been mounted on a shaker table for measurements, as shown in Figure 3.10(b). The cantilever PEH with

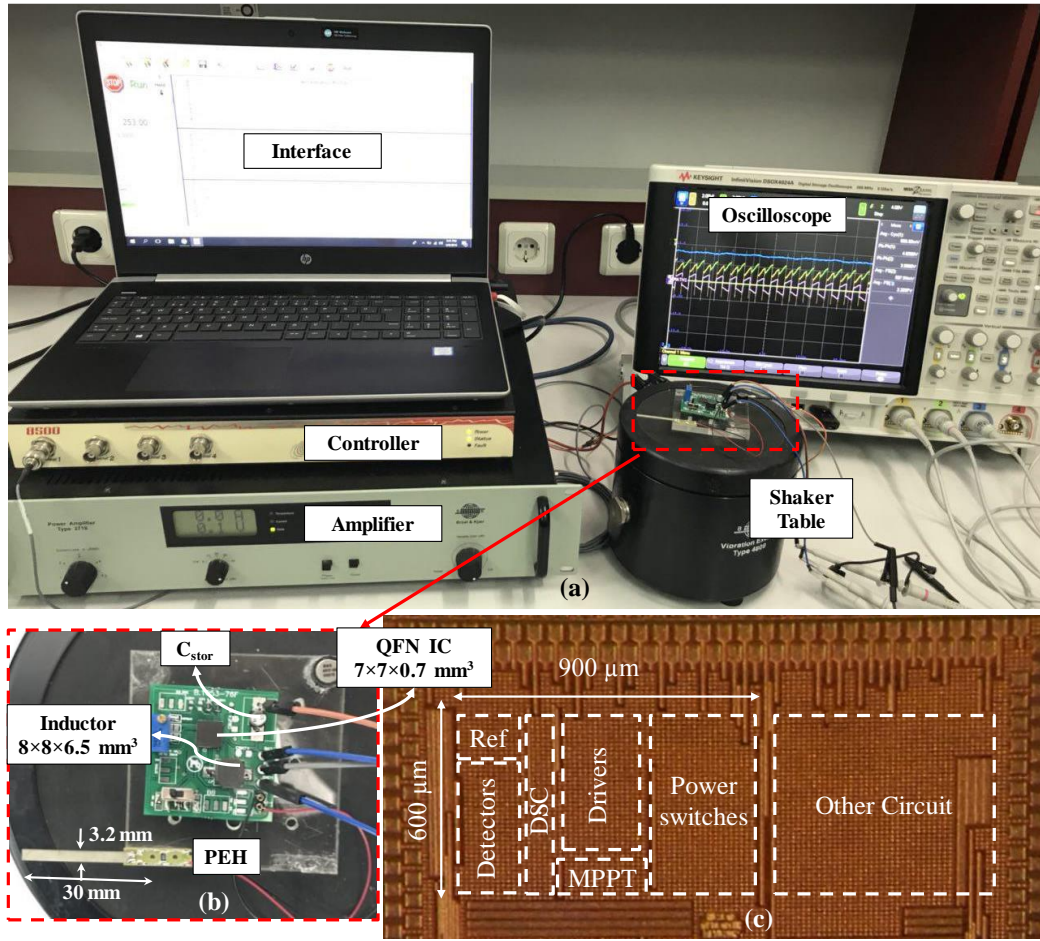


Figure 3.10. (a) Experimental setup, (b) evaluation board, and (c) die micrograph.

28.6 mm×3.2 mm dimensions has an output capacitance of 15 nF, and resonance frequency of 253 Hz.

The measured voltage and current waveforms with corresponding phases during operation mode are detailed in Figure 3.11, while PEH is excited at resonance frequency and $V_{OC}=1$ V. Figure 3.12 shows measured piezoelectric voltage and optimum extraction time in MPPT mode in starting point as illustrated in Figure 3.9.

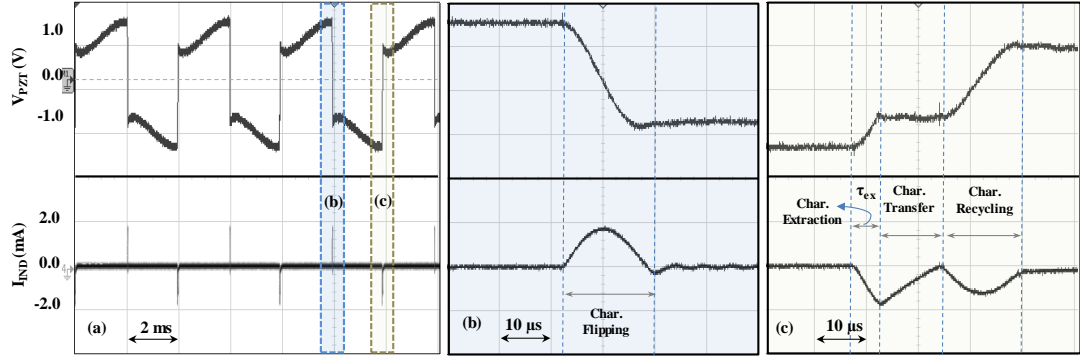


Figure 3.11. Measured piezoelectric voltage and inductor current waveforms for (a) steady state operation of SA_SSH IC (b) close up of charge flipping instants, (c) close up of charge extraction and recycling instants.

The optimal charge performance of the energy harvesting system is evaluated by manually tuning extraction time, τ_{ex} , as depicted in Figure 3.13 with $C_{stor}=1 \mu F$, for 253 Hz PEH stimulation and 1 V peak-to-peak amplitude. The initial value of the output buffer is set to 1.85 V for safe operation. The employed MPP yields the fastest charge performance in comparison with shorter and longer extraction times. Shortened extraction time, $\tau_{ex}=4.54 \mu s$, harvests smaller amount of the generated charge and reinjects more charge into C_p , which limits energy conversion due to power losses. On the other hand, raising τ_{ex} to 6.31 μs decreases recycling charge into piezoelectric capacitance, and consequently reduces the contribution of the damping force.

The power delivered to 1 μF storage capacitance in parallel with a variable load resistance has been measured for different excitation levels. The extracted and output powers as a dependence of the extracted output power on storage voltage is low, as expected, due to the fact that the applied technique decouples the PEH and storage device during energy extraction. Measured extracted power and stored power as a function of the storage voltage are shown in Figure 3.14 for $V_{OC,pp}=2.24 V$ and $V_{OC,pp}=5.9 V$.

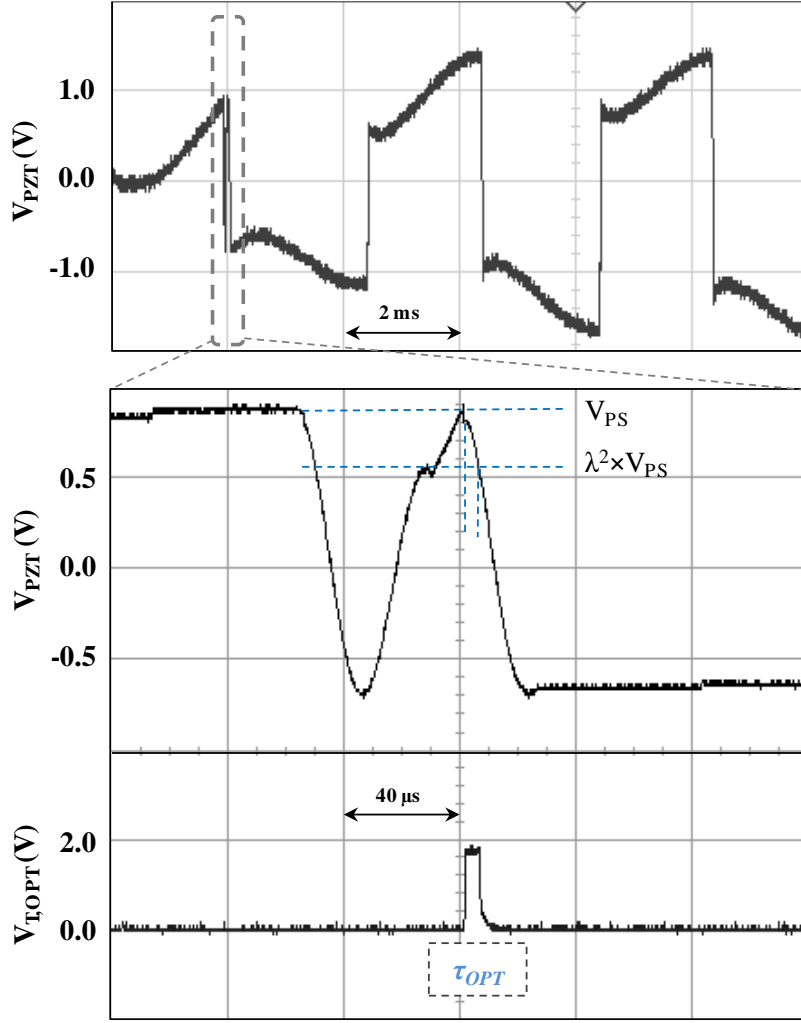


Figure 3.12. Measured waveforms of Optimum power point detection.

The extracted power is delivered to the output after conduction and switching losses. The power conversion efficiency, depicted in Figure 3.15, illustrates performance of the IC for $V_{oc,pp}$ range. The IC achieves maximum efficiency of 78.4% at $V_{oc,pp}=2.8$ V. Figure 4.16 shows the delivered power to storage element, P_{stor} , for different open circuit piezoelectric voltages, and the Figure of merit (FOM), which compares P_{stor} against the maximum extractable power by a lossless full bridge rectifier as in equation (3.13):

$$FOM = \frac{P_{stor}}{f_{exc} C_p V_{oc}^2} \quad (3.13)$$

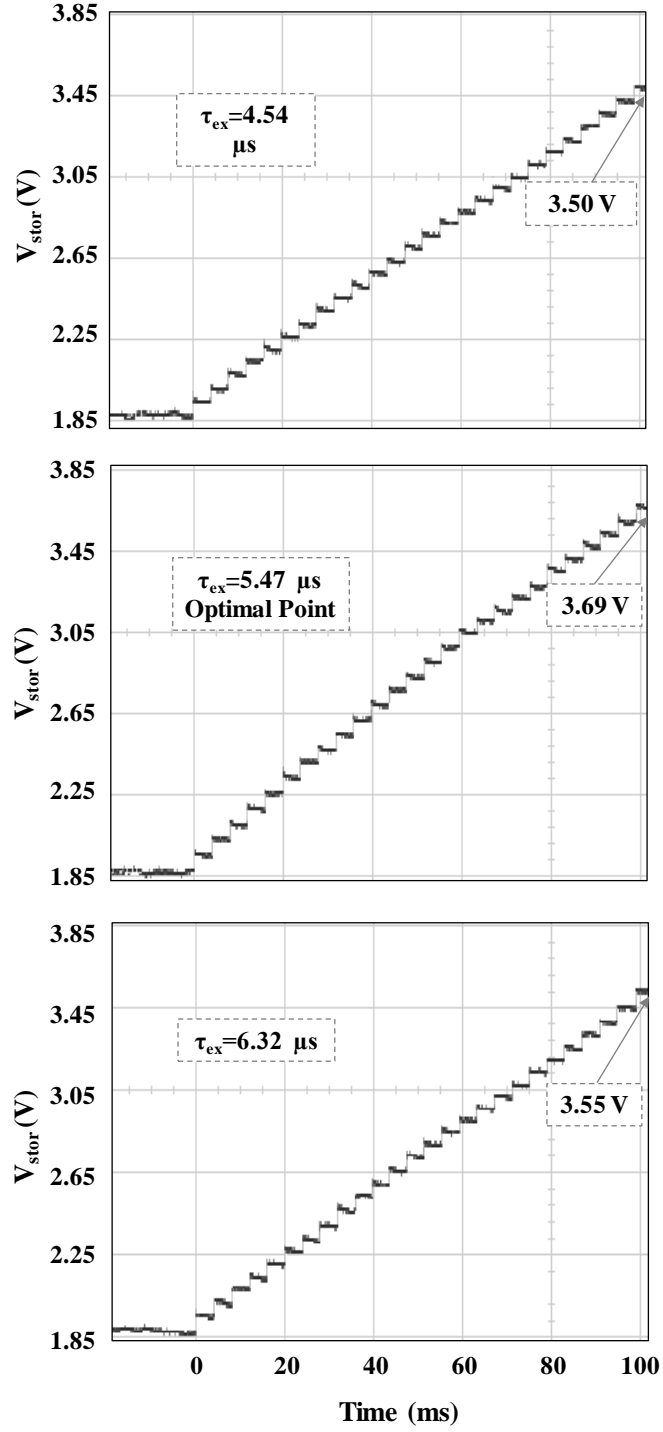


Figure 3.13. Measured charge of storage capacitance with $V_{OC,pp} = 2 V$ across charge extraction time (a) $\tau_{ex} = 4.54 \mu s$ (b) $\tau_{ex,opt} = 5.47 \mu s$ (c) $\tau_{ex} = 6.32 \mu s$ ($C_{stor} = 1 \mu F$, $R_L = 10 M\Omega$).

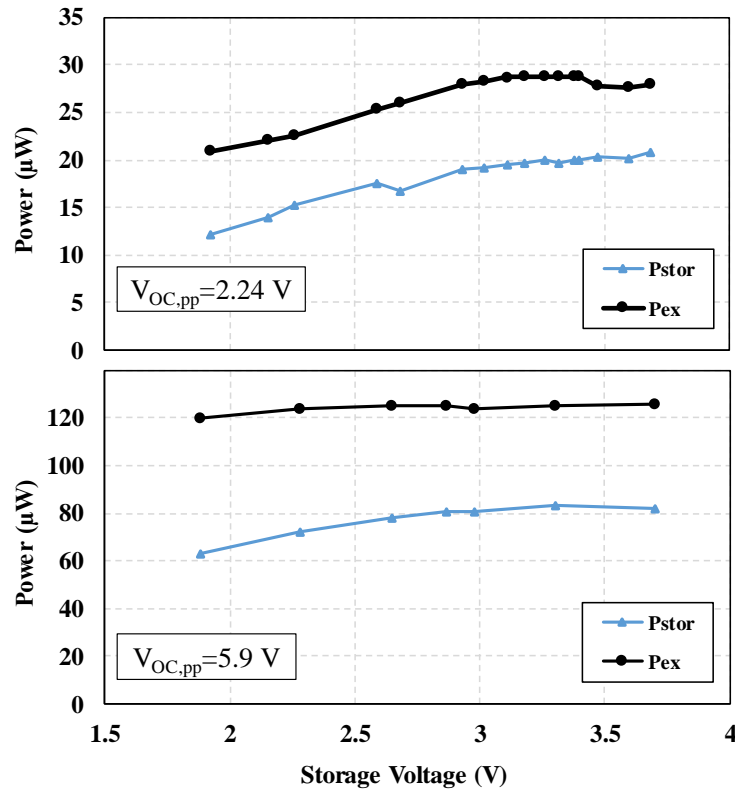


Figure 3.14. Measured output power vs. output DC storage voltage for $V_{OC,pp} = 2.24$ V and $V_{OC,pp} = 5.9$ V.

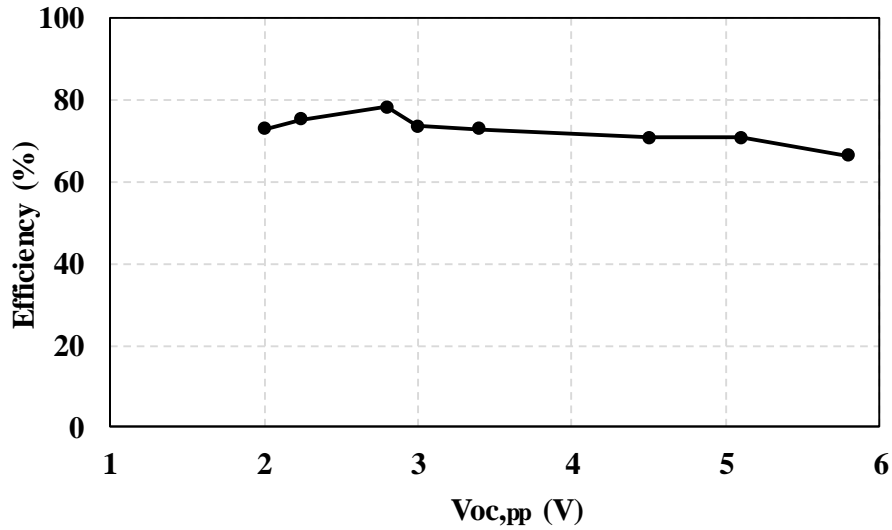


Figure 3.15. Measured end-to-end power conversion efficiency of proposed IC.

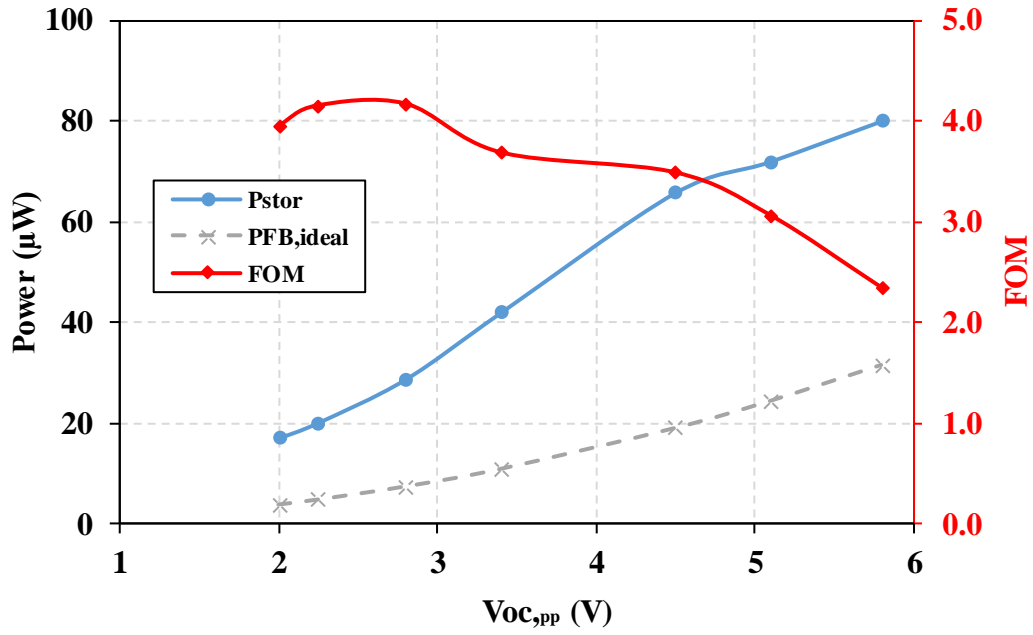


Figure 3.16. Measured harvested power by proposed IC compared from 103YB PEH to ideal full bridge rectifier at different excitation levels.

This FOM has been defined previously in [56][68][51]. The proposed IC harvests 19.9 μW from cantilever PEH at $V_{OC}=1.12$ V, and multiplies stored power 4.16 times compared to a lossless full-wave bridge rectifier, which delivers 3.74 μW onto optimum load resistance from the same vibration. The proposed system has reduced power gain as open circuit voltage of the PEH increases, due to the increase in power losses with excitation level.

While most applications encompass periodic and semi-periodic vibrations, shock vibration is an abundant energy source used to power up electronic devices. Nevertheless, randomness of such an energy source is a great challenge in energy harvesting devices. To evaluate performance of the proposed IC under shock vibration conditions, the harvesting platform is tapped manually and the outcomes are observed as shown in Figure 3.17. The energy harvesting system charges 1 μF storage capacitance from 2 V to 2.5 in response to the three shock excitations. The energy extraction is terminated for each tap as the peak detector is unable to sense damped vibration. The implemented energy harvesting system adapts to any variation of the

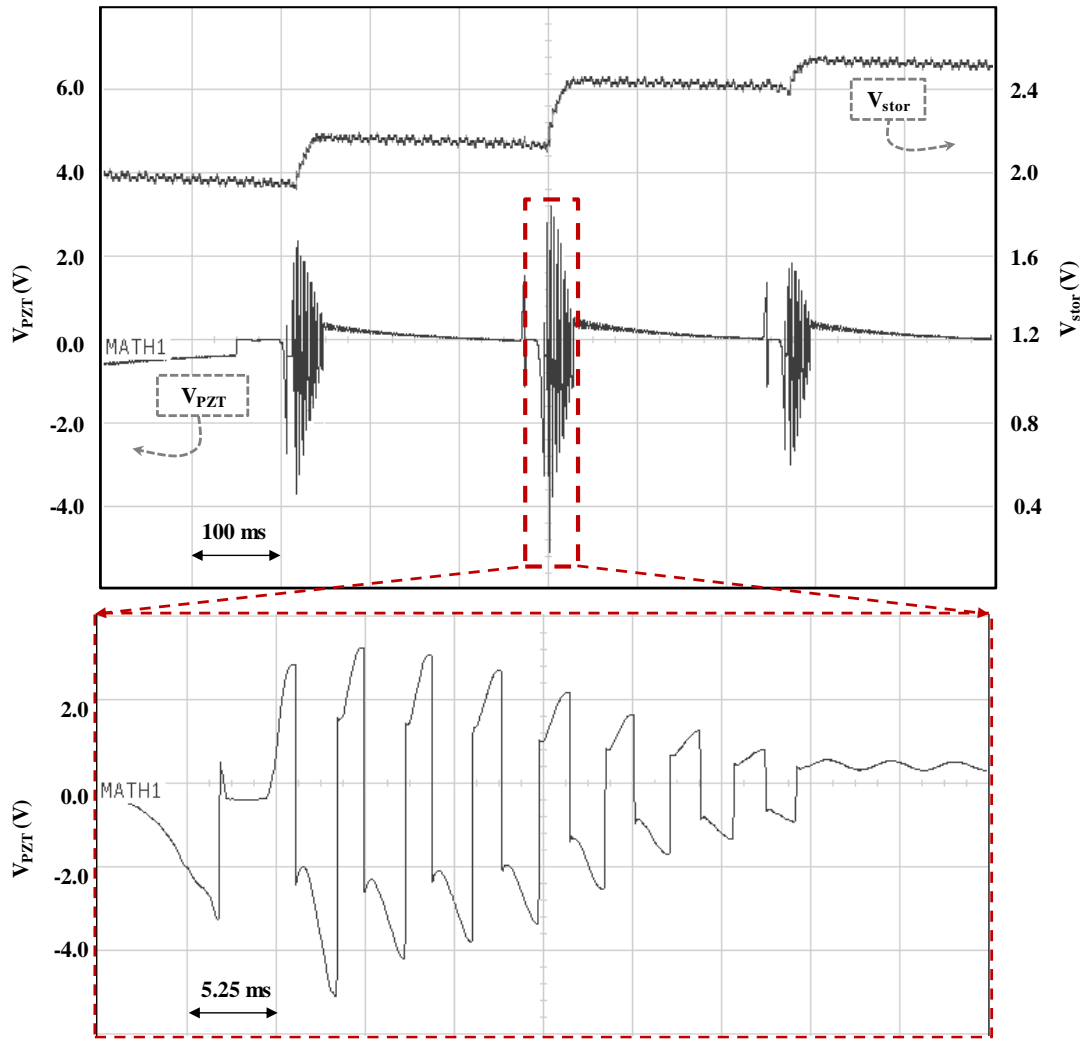


Figure 3.17. Measured waveforms of proposed IC in response to shock excitations.

input vibration, since it extracts and recycles the harvested energy automatically in each cycle in regards to previously measured extraction time.

3.4 Performance Comparison with MEMS Harvester

The power measurements is also conducted for custom-made MEMS PEH mounted on shaker table with output capacitance of 2 nF, and resonance frequency of 317 Hz. The harvested power, P_{stor} , and FOM as a function of open circuit piezoelectric voltages, V_{OC} , is depicted in Figure 3.18 for 1 mH and 3.3 mH external inductor. The power gain of 5 and 4.6 is achieved voltage with 1mH and 3.3 mH inductor,

respectively. This power gain is due to the lower coupling-factor of the MEMS PEH, where the performance of the full-wave rectifier is severely affected. For better overview, performances of the MSEE chip, presented in chapter 2, and on-chip FWR is also measured with the MEMS PEH at the same conditions as depicted in Figure 3.19.

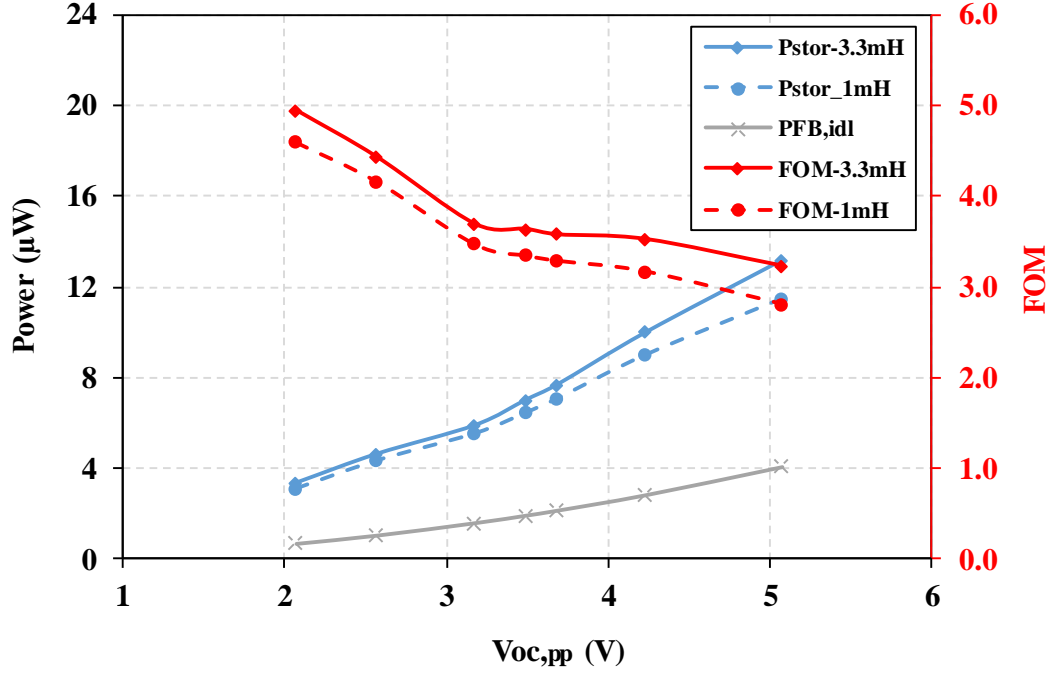


Figure 3.18. Measured harvested power by proposed IC from MEMS PEH compared to ideal full bridge rectifier at different excitation levels.

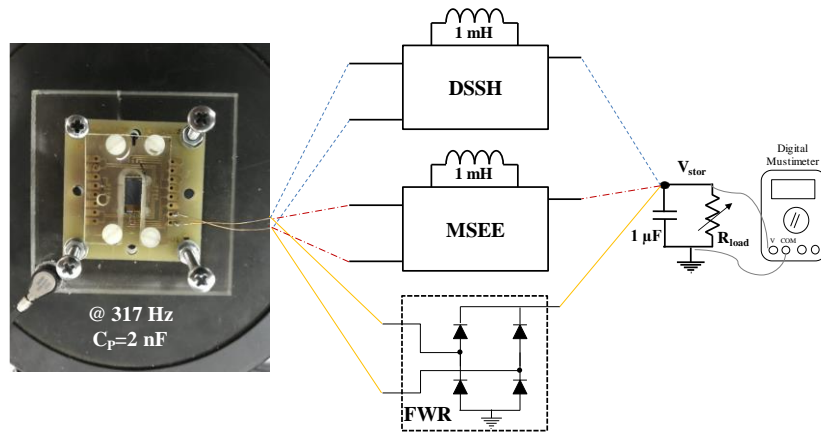


Figure 3.19. Setup to measure extracted power by the DSSH chip, MSEE chip, and on-chip FWR from MEMS PEH.

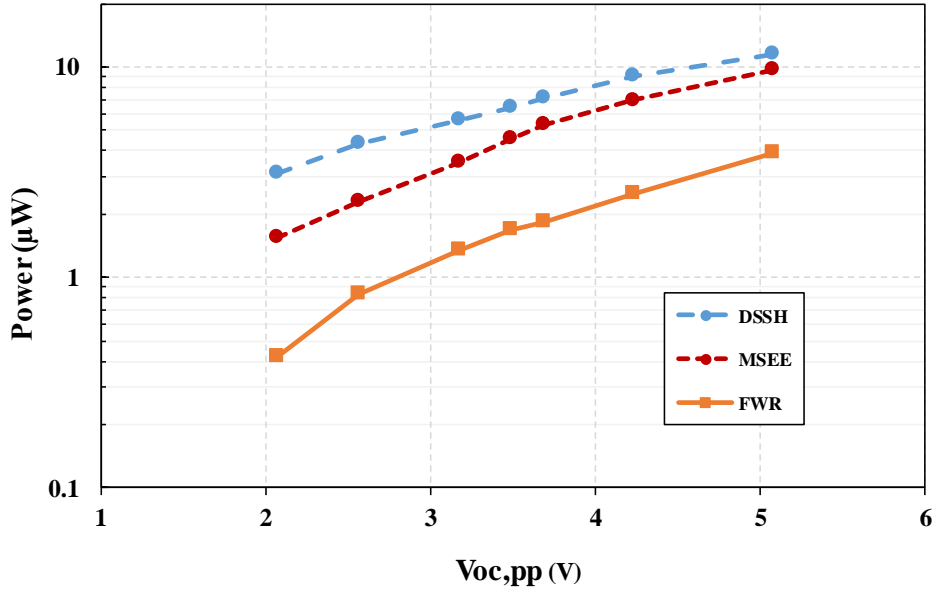


Figure 3.20. Measured power comparison of DSSH, MSEE, and full-wave rectifier at different open-circuit piezoelectric voltage.

Figure 3.20 compares the extracted power of DSSH IC, MSEE IC, and full-wave rectifier as a function of open-circuit voltage from MEMS PEH. The extracted powers at low excitation levels reveal that the DSSH can provide maximum power gain of 2 and 7.4 with regard to MSEE and FWR, respectively. However, as input power increases, the power gain weakens due to the decrease of the effect of increasing damping-force. For $V_{oc,pp}=5$ V, the power gain of 1.2 and 3 is achieved with respect to MSEE and FWR.

3.5 Discussion

Table 3.1 compares characteristics and performance of the proposed IC against recent piezoelectric energy harvesting ICs in the literature. The proposed SA-DSSH approach provides self-adjusting charge flipping system with above 78% flipping efficiency and 78.4% overall power conversion efficiency. Designs in [54] and [51] also don't require external adjustment, but the FOM is less than half of the one measured in the proposed IC. Kwon [56] used external tunable delay to invest from battery into piezoelectric harvester that should be adjusted exclusively for each vibration strength. The

investment technique loses its efficiency at weak and damped vibrations. Contrary to [56], proposed IC shows higher FOM, in weak vibrations and is highly efficient in response to damped vibration. The proposed circuit achieves a maximum FOM of 4.95 at resonance excitation. The IC automatically adjusts charge flipping time and optimal extraction point, and reduces dependence of power extraction to the output load, which make the proposed circuit more robust than [68]. The proposed MPPT circuit can estimate power losses associated with the system, and can manage charge on piezoelectric harvester to extract maximum energy.

Table 3.1 Comparison of DSSH IC with state-of-the-art.

Ref.	[19] SSHI	[56] Invest	[54] SSHI	[68] SSHI	[51] SSHI	Design I SECE	This work SA_DSSH	
Process CMOS	0.35 μm	0.35 μm	180 nm	0.35 μm	0.32 μm	180 nm	180 nm	
Chip area (mm^2)	4.25	1.8 \times 1.3	0.9 \times 1	1.2	0.98 \times 0.76	0.9 \times 0.7	0.9\times0.6	
Inductor (μH) (Volume (mm^3))	820 (-)	330 (416)	470 (-)	3300 (29650)	220 (29650)	1 mH (67)	3300 (416)	1000 (67)
C_p (nF)	12	15	8.5	9	19	4	15	2
f_{exc} (Hz)	225	143	419	229	144	390	253	317
V_{OC} (V)	2.4	2.6	3.39	0.95	4.9	4.5	1.12	1.07
$P_{\text{FB,idl}}$ (μW)	15.67	14.48	41.05	1.86	65.7	8.3	4.475	0.678
P_{stor} (μW)	47	52	55	8.19	136	26.5	20	3.1
FOM ($P_{\text{stor}}/P_{\text{FB,idl}}$)	3	3.59	1.34	4.4	2.07	3.2	4.2	4.6
OPP Flip timing	- Ext. Adj.	- Ext. Adj.	- Self. Adj.	Ext. Adj. Ext. adj.	- Self. Adj.	- -	MPPT Self-Adj.	
Load Indep.	NO	-	NO	NO	NO	YES	YES	

To sum up, presented novel synchronized switching configuration in this chapter aims to boost extracted energy from low coupling factor PEHs, and provides load-independent energy extraction with a single inductor. The implemented circuit benefits from self-adjustment charge-inversion process and MPPT circuit that secure optimal operation point. The operation and performance of the IC is validated through macro-scale and custom-made MEMS PEHs. The IC achieves maximum power gain of 4.2 at output power of $20\text{ }\mu\text{W}$ compared with ideal full bridge rectifier that harnesses $4.75\text{ }\mu\text{W}$ for the same vibration strength. The IC can harvest energy efficiently from shocks, as system adjusts optimum operation point automatically regardless of the variation in the available energy on PEH. The presented IC delivers the utmost extractable energy to storage element, which is a significant contribution for the realization of the energy harvesting micro-devices.

After extensive study on ICs for PEHs, it is intended to examine harvesting energy from both low and high frequency vibrations in the purpose of enhancement of power capacity. The next chapter investigates the hybridization of the PEH with electromagnetic harvester through SECE converter for this task.

CHAPTER 4

HYBRID IC FOR PEHS AND ELECTROMAGNETIC HARVESTERS

In this Chapter, a hybrid system is proposed to combine piezoelectric energy harvesters with electromagnetic energy harvesters to enhance energy extraction from vibrations. Scavenging of environmental vibrations is a promising approach to power up WSNs through piezoelectric and electromagnetic energy harvesters. In the literature, there are different electronic systems for harnessing low frequency vibrations through electromagnetic harvesters [64], and high frequency vibrations through piezoelectric harvesters [65], [51]. Harvesting energy from both low and high frequencies are beneficial in terms of increased power capacity, which in turns improves lifetime and system reliability. A vibration-based harvesting system presented in [69] combines electromagnetic and piezoelectric energy to achieve a hybrid structure . The main concern in this system is that it can harvest only from a single vibration source; otherwise, the system operation fails. The triple hybrid power generator proposed in [70] has inputs from three different sources, and can extract power from each one at the same time to supply a DC voltage. Nevertheless, the system can only provide output voltage level around 1 V in an extremely narrow range. Moreover, power conversion efficiency of the system is relatively low in this design.

The main motivation of this framework is to build a hybrid system to scavenge energy from both (EMH) and PEH, as available vibration sources exist at low and high frequencies in the environment, and enhance the extracted output power. Both EMH and PEH produce AC outputs, and need rectification and power management circuits to accumulate extracted charge on a single storage element. Thus, a novel hybrid IC is implemented and its operation is validated through a compact and wearable platform that includes custom designed electromagnetic harvester (EMH) and PEH for scavenging energy from human motion. This chapter is organized as follows: Section 4.1 describes hybrid system operation in detail. Section 4.2 discusses experimental

results from the fabricated IC for high piezoelectric excitation frequencies. Section 4.3 presents the wearable energy harvesting system with measurements in an application like environment. Finally, Section 4.5 discusses the results.

4.1 Hybrid System Architecture

4.1.1 Proposed System and Operation Principle

The proposed hybrid IC, composed of three building blocks, is presented in Figure 4.1. The system utilizes power from EMH to invest energy to PEH in order to increase the damping force. The harvested energy from EMH is then transferred to the storage element concurrently with the energy extracted from the PEH. Electromagnetic IC rectifies AC voltage through a self-powered voltage doubler with active diodes. PEH IC is designed based on Synchronous Electric Charge Extraction (SECE) technique due to the fact that this topology provides a load independent structure for fast-charging the storage element with a wide range of output voltage. The circuit manages timing to share the charge on buffer capacitance, $C_{BUF,EM}$ with PEH capacitor, C_{PZT} . This leads to an improvement in the electromechanical coupling factor of piezoelectric harvester, and hence in the total power extraction compared to sum of output power from two harvesters. The maximum extractable energy from the piezoelectric harvester is:

$$E_{PZT1} = \frac{1}{2} C_{PZT} V_{PP}^2 \quad (4.1)$$

where V_{PP} is the voltage between two terminals of the PEH harvester. In the proposed system, the circuit invests charge into C_{PZT} from $C_{BUF,EM}$ at minimum or maximum displacement of the harvester. Assume ΔV is added up on C_{PZT} . After the full swing of the PEH harvester, $V_2 = V_{PP} + \Delta V$ accumulates on C_{PZT} , resulting in extractable energy from harvester as:

$$E_{PZT2} = \frac{1}{2} C_{PZT} V_2^2 = \frac{1}{2} C_{PZT} (V_{PP} + \Delta V)^2 = \frac{1}{2} C_{PZT} V_{PP}^2 + \frac{1}{2} C_{PZT} \Delta V^2 + C_{PZT} V_{PP} \Delta V \quad (4.2)$$

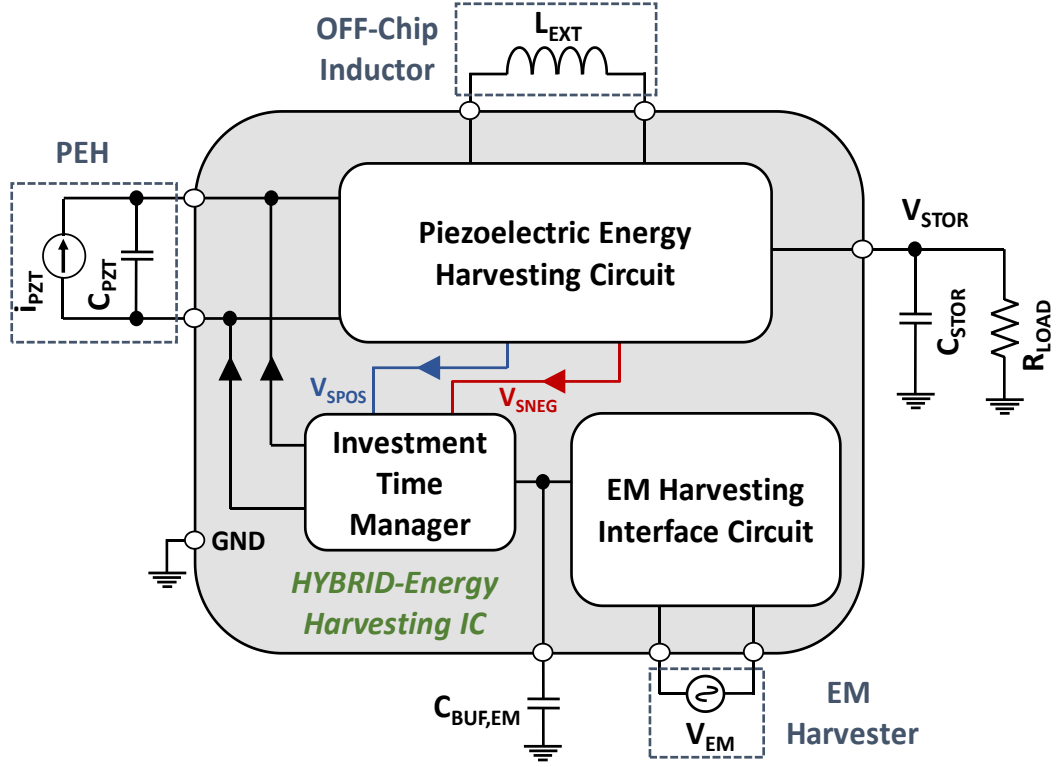


Figure 4.1. System architecture of the vibration-based hybrid harvester interface.

where $1/2C_{PZT}V_{PP}^2 = E_{PZT1}$ is the energy generated on C_{PZT} without any investment, $1/2C_{PZT}\Delta V^2 = E_{INV}$ is the invested energy from EM harvester output, and $C_{PZT}V_{PP}\Delta V = E_{GAIN}$ is the augmenting energy extracted due to the squared relation of generated energy to the voltage. It can be seen from equation (4.2) that apart from the individual outputs of each harvester, augmenting energy, E_{GAIN} can be generated on C_{PZT} , which improves the output power of the hybrid system. As a result, proposed hybrid architecture can simultaneously extract more power from two different harvesters compared to voltage adding [71], [72] and inductor sharing techniques [73], [74].

4.1.2 Electromagnetic Harvesting IC

Environmental vibrations can occur both at low and high frequency domains. Inertial mass of EMHs enables capturing of low frequency and low profile ambient vibrations with limited output voltage amplitude, which requires efficient rectifier circuits to minimize losses. The AC voltage harvested from low frequency vibrations is efficiently converted into DC through an IC that both rectifies and boosts the input

voltage. The utilized electromagnetic harvesting IC depicted in Figure 4.2 is a modified version of the one presented in [64]. The rectification of the input signal is handled through an active diode that provide forward voltage-drop close to that of an ideal rectifier. The active diode utilizes a PMOS switch to pass or block the input voltage based on a comparator output, which is powered by passive AC/DC quadrupler structures. The passive components are also driven by the EMH to maintain self-powered operation. The positive quadrupler delivers high enough voltage to turn off the switch with low leakage current, while the negative quadrupler reduces path resistance to drive current through high source-to-gate voltage. For negative input voltages with $V_x < \text{GND}$, switch M_{P9} is turned on by the corresponding comparator and charges the external capacitor until the negative input peak. When $V_x > \text{GND}$, the M_{P9} switch is turned off and the charge is stored on the capacitor. For positive input voltages with $V_x > V_{\text{BUF,EM}}$, the M_{P10} switch is turned ON, and the output capacitor ($C_{\text{BUF,EM}}$) is charged until two times the input peak voltage. When V_x goes below $V_{\text{BUF,EM}}$, the switch M_{P10} is turned off to preserve the maximum charge at the output. The utilized comparators are designed to obtain single-ended output with high gain and sensitivity, and minimize forward voltage drop between source and drain of the active switches.

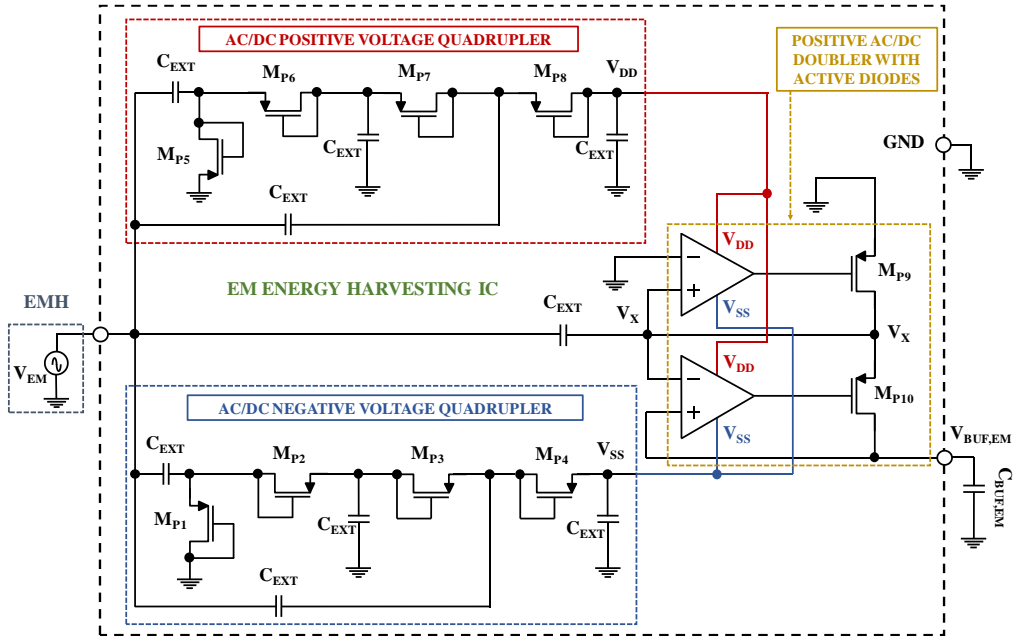


Figure 4.2. Self-powered electromagnetic harvesting IC for low frequency vibrations.

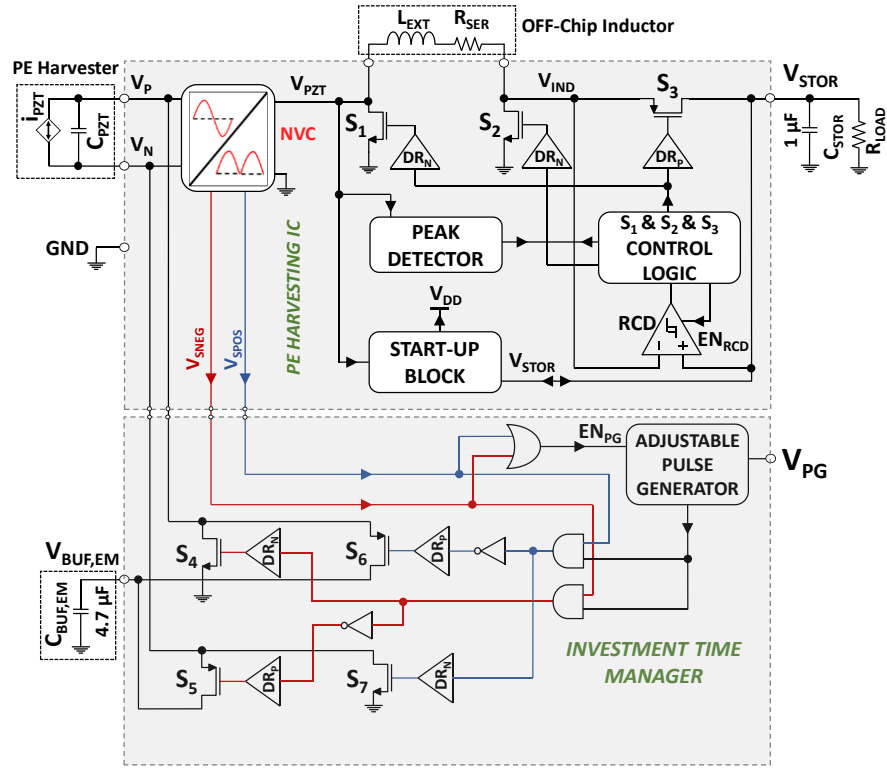


Figure 4.3. Schematic of PEH IC and investment time manager.

4.1.3 Piezoelectric Harvesting IC and Investment Time Manager

Piezoelectric harvesting IC operates in synchrony with investment time manager to facilitate charge transfer from buffer capacitance. Piezoelectric harvesting IC consists of a negative voltage converter (NVC), start-up block, three detectors, and switch control logic similar to our previous work [75], as shown in Figure 4.3.

4.1.3.1 Negative Voltage Converter

NVC generates a peak-to-peak open circuit voltage in each half cycle. Two switches controlled by two comparators and two cross-coupled PMOS switches driven by piezoelectric harvester determine the charge-flow path to provide positive voltage. A current-follower input stage that monitors piezoelectric voltage following by a common-source stage form the comparator as shown in Figure 4.4. An offset is imposed by slightly mismatching the aspect ratio of M3 and M4 MOSFETs to avoid premature switching during transition. The rising edge of each comparator output indicates maximum and minimum displacement that shorts lower-potential terminal of the harvester to ground.

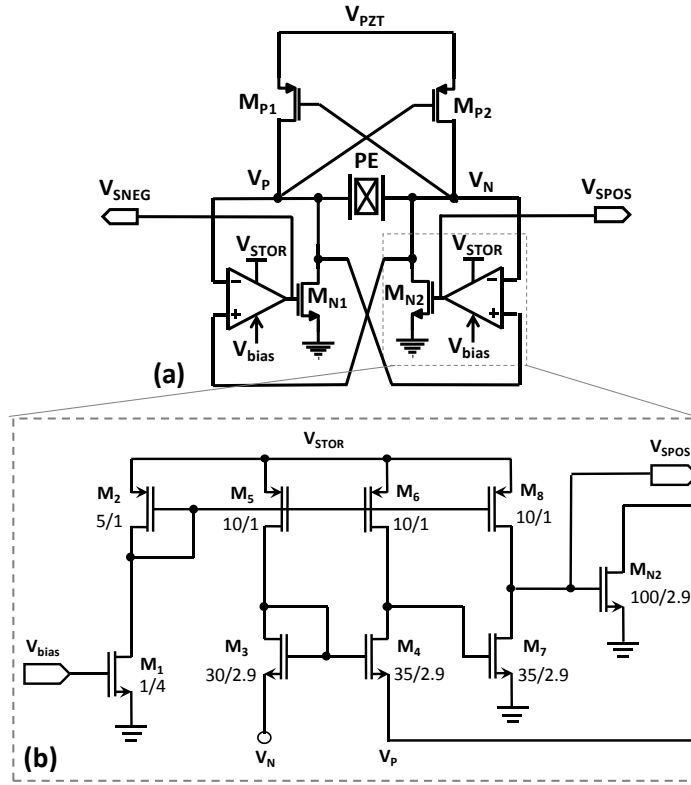


Figure 4.4. Schematic of (a) the proposed negative voltage converter (NVC), (b) the comparator utilized inside NVC structure.

The storage capacitance is initially charged via the NVC, a diode, and a switch controlled by the start-up circuit. The circuit continuously monitors the storage voltage and powers up the control unit when it exceeds the minimum required value of 1.1 V.

4.1.3.2 PZT Harvesting Phases

Energy extraction is realized through four phases of switching as shown in Figure 4.5. In phase I, all the switches are OFF, and voltage across piezoelectric capacitor is increasing due to charge generation on piezoelectric material. As peak instant is sensed by the peak detector (PD), the circuit initiates phase II by turning the switch S_2 ON. The operation of the PD was extensively analyzed in chapter 2. At this point, charge generated on C_{PZT} is transferred to the external inductor due to the establishment of LC resonance circuit. Zero-crossing detector (ZCD) outputs a signal when V_{PZT} drops below zero to terminate charge extraction. In phase III, extracted charge is transferred from inductor to the storage capacitance C_{STOR} by turning S_2 OFF

and S_1 & S_3 ON. Charging of C_{STOR} is completed as stored charge starts flowing back from C_{STOR} to the inductor. A standard two-stage comparator monitors voltage drop on M_3 to signal end of phase III. Charge investment is performed during Phase IV. The rising edge of V_{SPOS}/V_{SNEG} of NVC initiates charge investment by triggering an adjustable pulse generator. Investment time manager applies a pulse to invest charge into piezoelectric capacitance with controlling switch network corresponding to downward or upward displacement.

4.1.3.3 Adjustable Pulse Generator

Adjustable pulse generator circuit is implemented as shown in Figure 4.6 to control the time interval of charge investment. The circuit uses inverters and R-C components to set delay time. A current-controlled inverter is also utilized for fine-tuning. As the input transitions high, M_7 and M_5 trip and M_4 is still ON so that V_x is discharged through M_4 and M_5 to generate rising-edge of a pulse. M_4 and M_6 start to trip within the delay time and M_7 pulls V_x up. As result, output falls to generate the output pulse width. All components, including the resistor and the capacitor, are embedded into the chip.

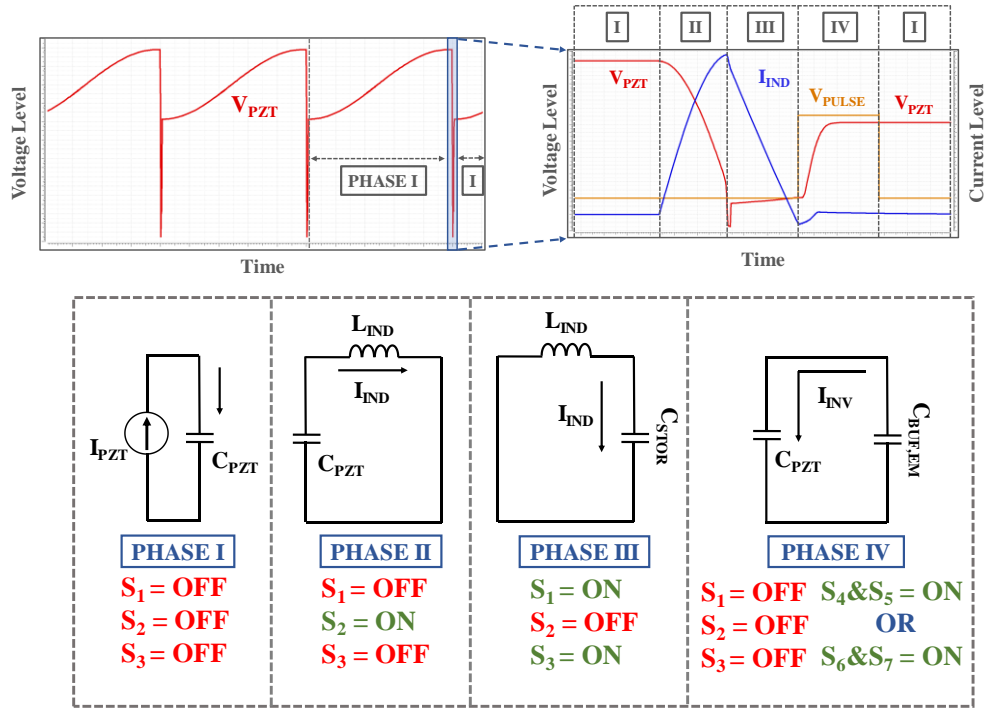


Figure 4.5. Summary of operation phases for piezoelectric energy harvesting IC and investment time manager.

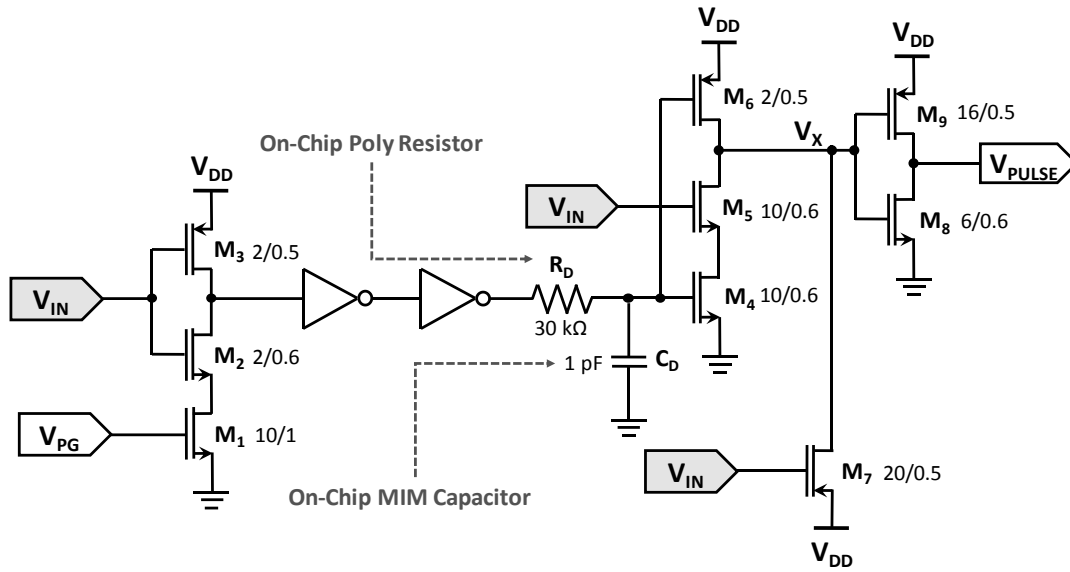


Figure 4.6. Schematic of the adjustable pulse generator.

4.2 Design Validation

Figure 4.7 presents the die micrograph of electromagnetic and piezoelectric harvesting ICs fabricated in 0.18 μm HV CMOS technology. The first experiment verifies operation of the proposed system with the assumption that two independent vibration sources are available at lower and higher frequency bands. A PEH (Mide V22) with a 4.7 nF capacitor is excited with shaker table and EMH is emulated by an AC voltage source with a 72 Ω series resistor. An inductor with $L=3.3$ mH and parasitic resistance $R=8.97$ Ω , and a storage capacitor with $C_{\text{stor}}=1$ μF are externally connected to the circuit as shown in Figure 4.8.

Figure 4.9 shows measured waveforms of the hybrid interface operation while PEH and EMH are excited at 500 Hz and 10 Hz, respectively. The piezoelectric open circuit voltage is set to 3.45 V_{PP} . The hybrid IC invests harvested energy from 4.7 μF buffer capacitance to $C_{\text{PZT}}=4.7$ nF, and transfers available charge on PEH to 1 μF storage capacitor. Figure 4.10 depicts the charging profile of a 1 μF capacitor in parallel with 150 k Ω load resistor for different outputs of electromagnetic harvesting system. Initially, the storage voltage is observed to be stabilized for PEH excitation at 500 Hz with PEH open circuit voltage $V_{\text{OC}}=4.4$ V_{PP} and without any charge investment from EM harvesting circuit. Then, hybrid operation is enabled to monitor the charging

performance of the proposed IC for different input power levels supplies from the EMH. The Hybrid IC transfers the stored charge from buffer capacitor to the storage capacitor, thus reinforcing power output.

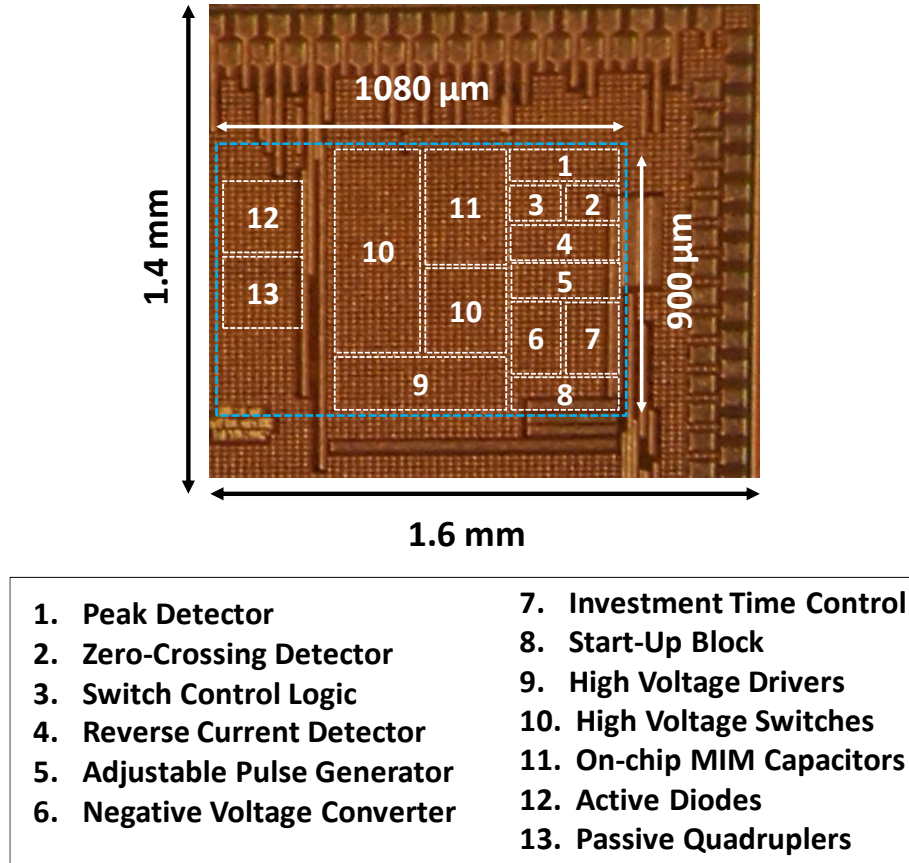


Figure 4.7. Die micrograph of the implemented hybrid IC fabricated in 0.18 μm HV CMOS technology.

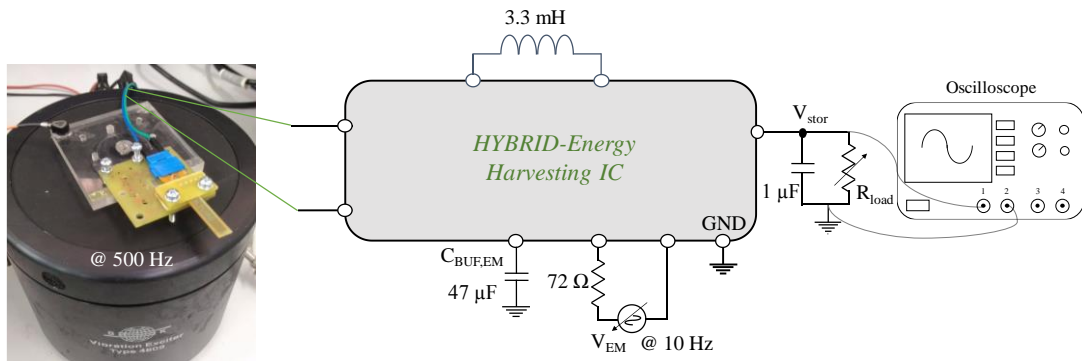


Figure 4.8. Test setup for hybrid energy harvesting IC.

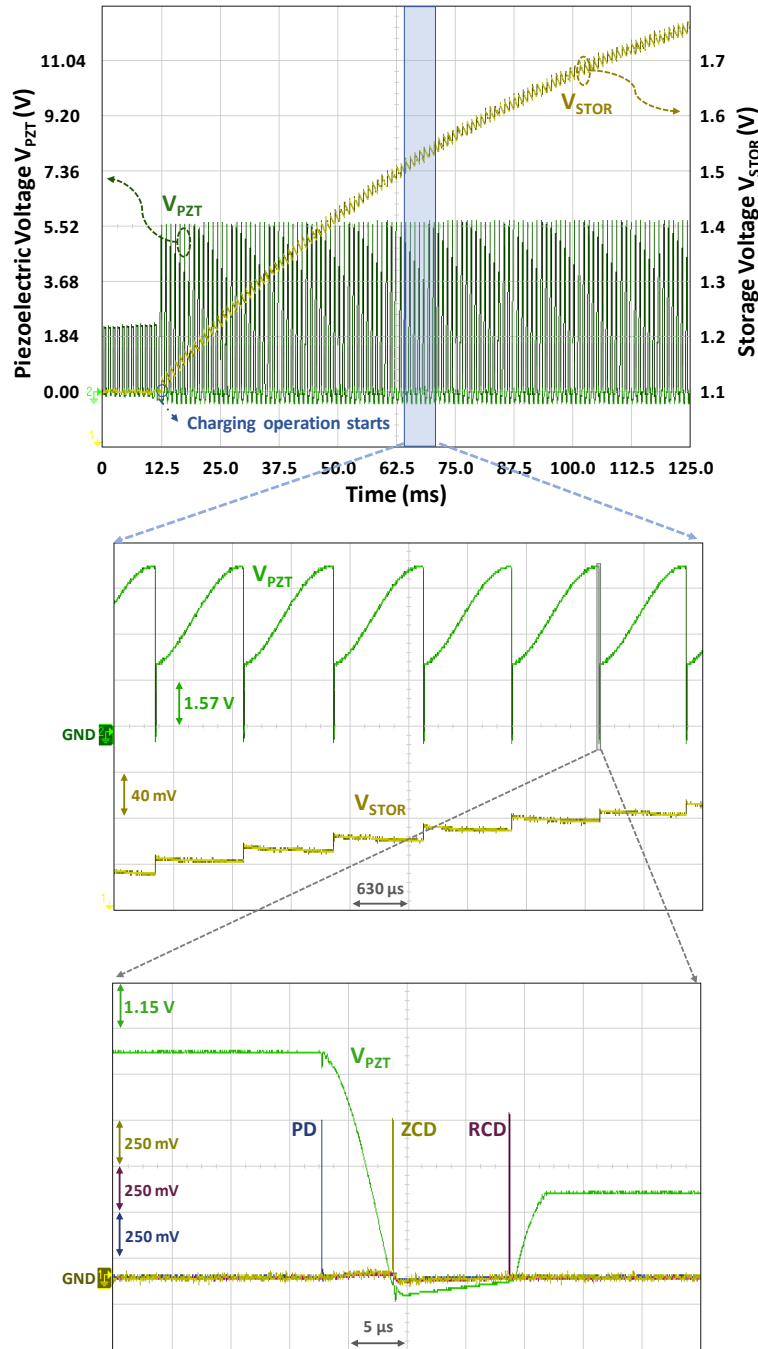


Figure 4.9. Measured waveforms of the hybrid harvesting interface operation with generated control signals PD, ZCD, and RCD.

Measured extracted power as a function of peak-to-peak PEH open circuit voltage for different power values at EMH IC input is depicted in Figure 4.11. Figure 4.12 shows measured power conversion efficiency ($\eta = P_{OUT}/P_{IN}$) for hybrid IC and stand-alone

ICs. As expected, power conversion efficiency increases with the charge investment from EMH based on the elevated damping of the PEH. Lower efficiency is observed at low V_{OC} , due to dominant static and conduction power losses. Maximum efficiency of 90.3% is observed for hybrid system at $V_{OC,PZT} = 5.5 V_{PP}$.

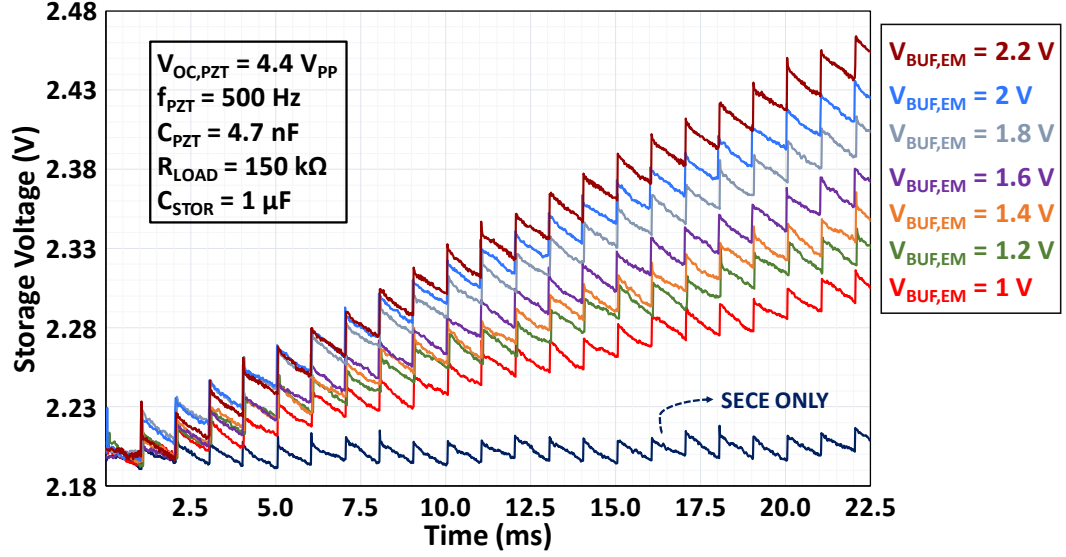


Figure 4.10. Measured charge profile of a $1 \mu F$ load capacitor for different outputs of electromagnetic harvesting IC.

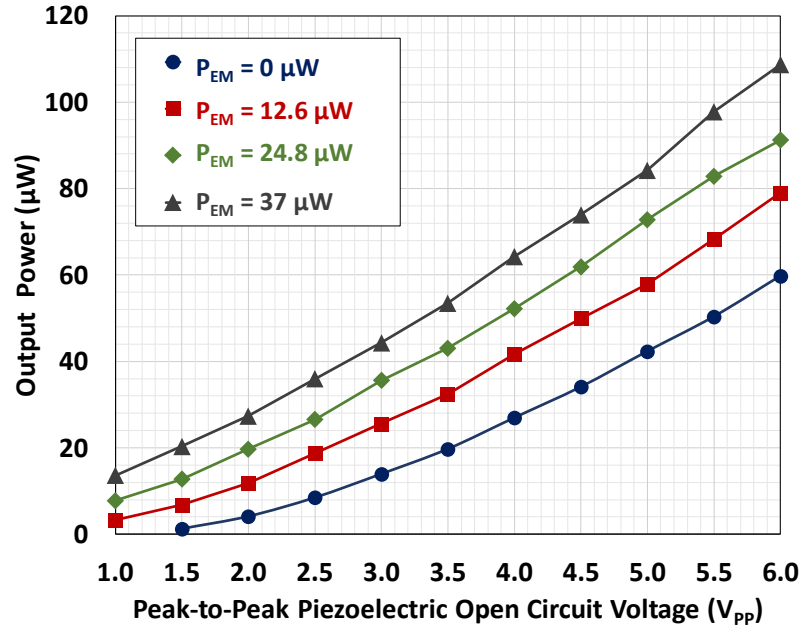


Figure 4.11. Extracted power vs. peak-to-peak piezoelectric open circuit voltage for high frequency excitations.

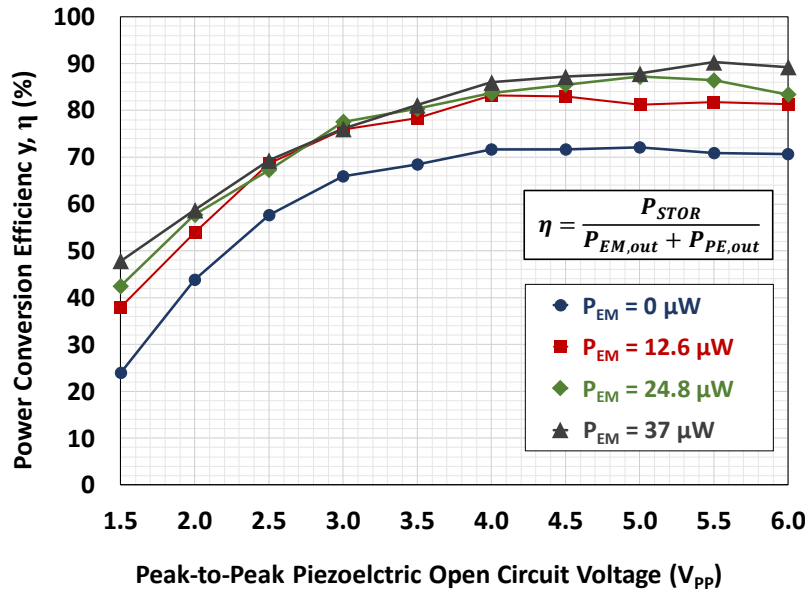


Figure 4.12. Experimental power conversion efficiency vs. peak-to-peak piezoelectric open circuit voltage for high frequency excitations.

4.3 Wearable Energy Harvesting System

In the second experiment, the hybrid harvester structure was built into a wearable prototype to extract power from body movements. The harvester is composed of a conventional PEH (V22BL) from MIDE Company and a custom-made EMH as shown in Figure 4.13. PEH V22BL has two identical piezoelectric layers with capacitance of $C_{PZT}=9$ nF on top and bottom of the cantilever beam, and only one of them is utilized in the hybrid system. In the proposed system, base structure of PEH is clamped to the lower cap of the EMH. A support beam with magnetic tip mass is attached to harvester cantilever beam to translate vertical motion. EMH, which can generate power from low frequency vibrations, has a similar structure as the one used in [70]. It contains a fixed magnet at the lower cap in opposite polarity with a free moving magnet inside the cylindrical tube. As the free moving magnet oscillates inside the pick-up coil due to external vibration, an alternating magnetic field induces voltage between two terminals of the pick-up coil according to Faraday's law. Moreover, when the free magnet gets closer to the lower cap, it pulls up magnetic tip attached to the support beam and consequently deflects cantilever beam. As the free magnet moves upward in the tube, magnetic tip is released and PEH starts oscillation at its damping resonance

frequency. This frequency up-conversion enables both harvester to generate energy concurrently.

Fabricated prototype of the hybrid system is presented in Figure 4.14. Electrical connection pins of harvesters are taken from top of the system in order not to disturb operation of harvesters. The wearable hybrid harvester system was located on the wrist of a jogger as shown in Figure 4.14(c). Throughout experiments, fundamental vibration frequencies between 2 and 3 Hz were observed for EMH placed on the wrist of a jogger as presented in [25]. PEH V22BL was clamped to the base structure, and operates around 20 Hz damping resonance frequency with the support beam and the tip mass.

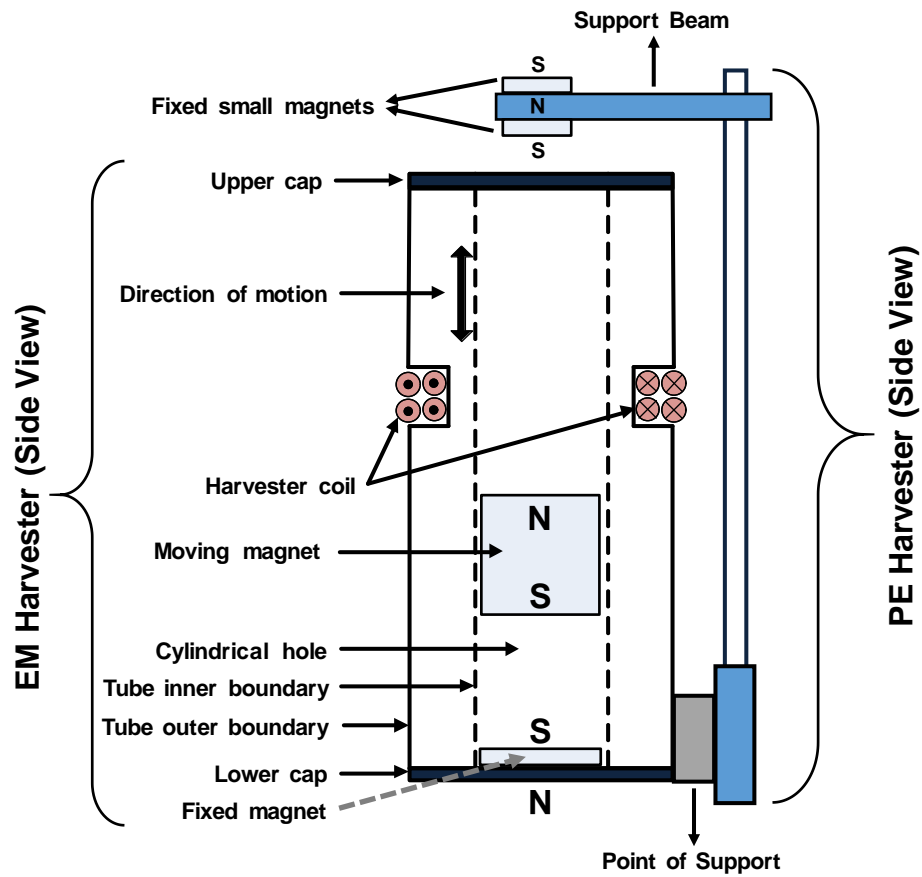


Figure 4.13. Schematic of hybrid energy harvester prototype consisting of a PEH (V22BL from MIDE Company) and custom-made EMH.

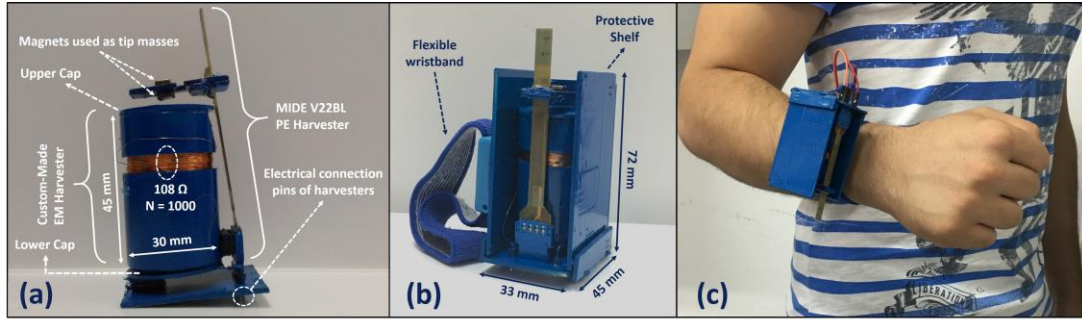


Figure 4.14. (a) Fabricated prototype of hybrid energy harvester, and (b) its protective shelf with flexible wristband adapted for daily usage of the system. (c) Hybrid energy harvester system placed on the wrist of a jogger.

The harvested energy from jogging charges the $C_{BUF,EM}$ as shown in Figure 4.15. Figure 4.16 presents the measured waveforms of V_{PZT} and V_{STOR} during jog when 800 k Ω load resistance is connected to storage capacitance. Waveforms of Figure 4.15 and Figure 4.16 were monitored at different time frames. Figure 4.16 demonstrates that piezoelectric tip mass is caught by EMH magnet before fluctuation of PEH beam dies out completely. As PEH displacement attenuates, most of the charge packet transferred to the storage capacitance belongs to the harvested energy by EMH. Measured extracted power of the hybrid system and standalone harvesting circuits for various loading conditions are presented in Figure 4.17. Hybrid system can deliver a power to the load close to the sum of PEH and EMH output powers. Moreover, the hybrid system can provide wide storage voltage range of 1V to 3.4 V while driving resistive load ranging from 100 k Ω to 1200 k Ω .

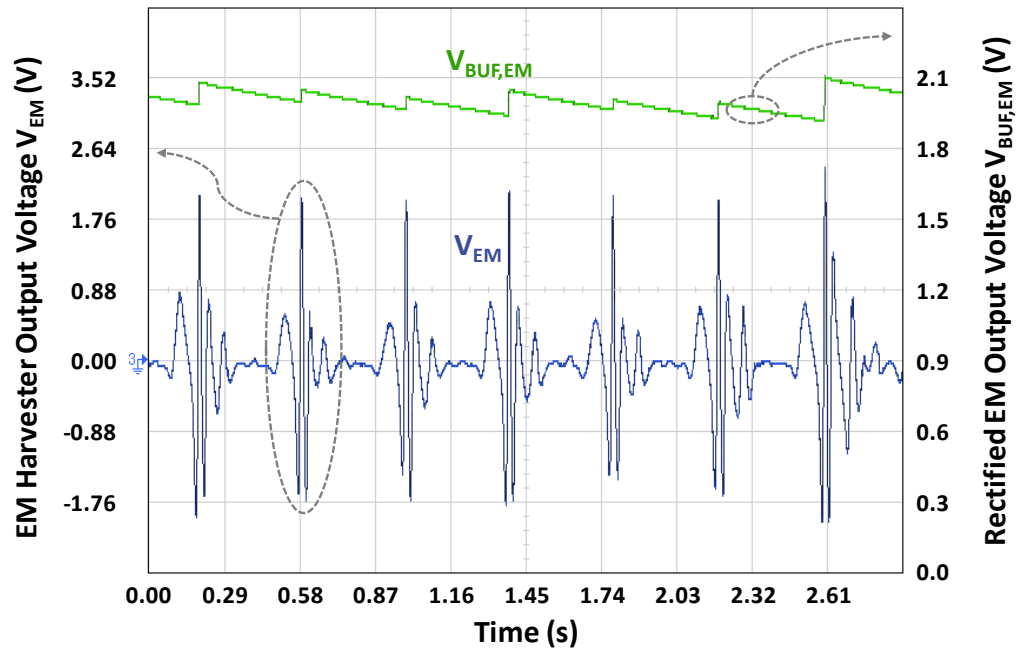


Figure 4.15. Measured waveforms of V_{EM} and $V_{BUF,EM}$ with hybrid system operation during jogging.

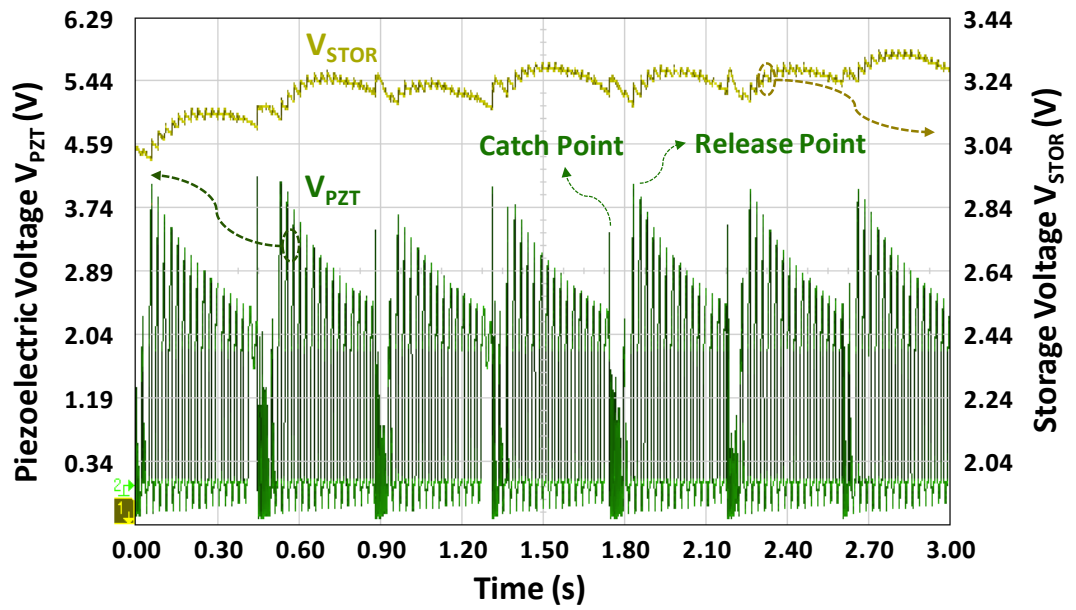


Figure 4.16. Measured waveforms of V_{PZT} and V_{STOR} with hybrid system operation during jogging.

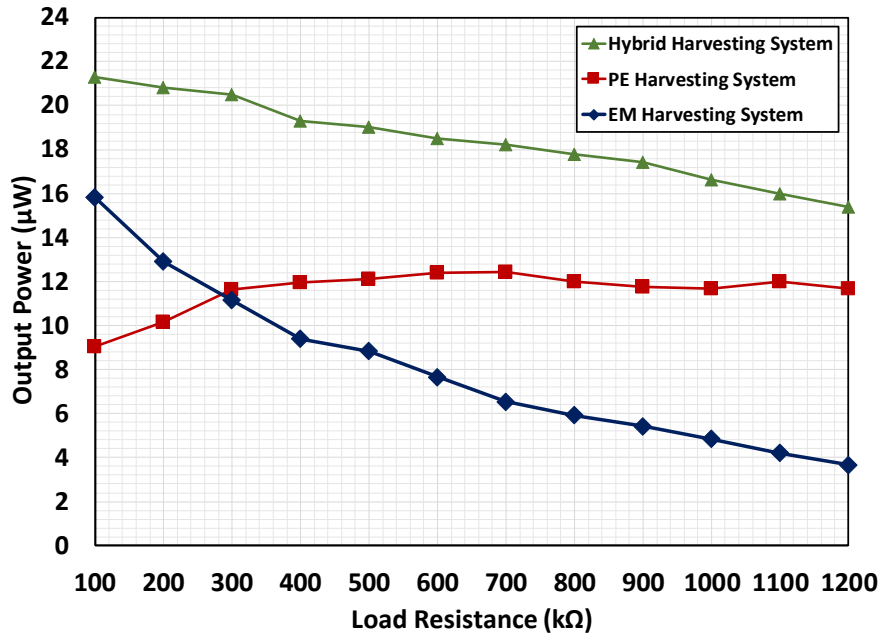


Figure 4.17. Experimental extracted power at various loading conditions for excitations during jogging.

More power could be generated if the resonance frequency of PEH is increased up and damping factor is diminished. Moreover, dimensions of EMH, which occupies most of the hybrid system volume, can be optimized to have a more compact device.

4.4 Discussion

Table 4.1 represents the performance of the proposed hybrid harvesting circuit compared with ICs in the state-of-the-art literature. The proposed IC for vibration-based harvesters can extract power in a wide vibration frequency range from 2 Hz to 500 Hz. The hybrid operation provides simultaneous extraction in a power range of 1 μW to 100 μW. Maximum power conversion efficiency of 90% is achieved, which is considerably higher than the state-of-the-art. The wearable harvesting system can provide up to 20 μW under different loads during walk action. Due to its relatively small dimension, this system can be placed on mobile animals to sustain WSNs and tracking applications. Besides, the proposed circuit is also adaptable to various harvester types that provides DC output, such as thermoelectric generators, to generate power simultaneously with the PEH. Finally, the proposed hybrid system can

efficiently extract available ambient energy, and can increase reliability of autonomous micro-devices in WSNs.

Table 4.1 Comparison of hybrid IC with state-of-the-art.

Parameters	Bandyopadhyay, 2012 [74]	Uluşan, 2018 [70]	Katic, 2018 [73]	This Work
Technology	0.35 μm	0.18 μm	0.18 μm	0.18 μm HV
Harvesting Sources	Photovoltaic Thermoelectric Piezoelectric	Piezoelectric Electromagnetic Thermoelectric	Glucose Biofuel Cell Thermoelectric	Piezoelectric Electromagnetic
Excitation Frequencies of Harvesters	PV: DC TEG: DC PEH: NA	PEH: 282 Hz EMH: 2-3Hz TEG: DC	GBFC: DC TEG: DC	PEH: 20-500 Hz EMH: 2-10 Hz
Minimum Input Power	PV: 150 μW TEG: 90 μW PEH: 45 μW	PEH: 4.2 μW EMH: 1 μW TEG: NA	GBFC: 0.5 μW TEG: 0.5 μW	PEH: < 0.7 μW EMH: 1 μW
Output Voltage	1.9 V	0.8-1.25 V	1.9 V	1.1-3.41 V
Peak Efficiency	NA	29% @ 68 μW	85 % @ 66 μW^*	90% @ 100 μW

* It is only for DC-DC circuit.

CHAPTER 5

CONCLUSION AND FUTURE WORK

In this Ph.D research, three different energy harvesting ICs have been developed: *i)* Adaptive MSEE IC *ii)* Optimal DSSH IC, and *iii)* Hybrid IC. Design and implementation of each IC, were demonstrated in details in the content of the relative chapter. Extensive experiments merged with custom-made MEMS PEH and commercial PEHs have been conducted for adaptive MSEE and optimal DSSH chips. The performance of each chip has been evaluated in terms of extracted power, power-conversion efficiency and operating range. Contribution of each chip and comparison with state-of-art were thoroughly discussed as well. Overview and major achievements are summarized in this chapter based on studies outlined in the research. Finally, we highlight points for further improvement as future works.

5.1 Overview and Major Achievements

5.1.1 MSEE IC

A fully self-powered IC has been implemented to enhance practicability of MEMS PEHs to can be used in implantable or micro devices. The major achievements with regard to the criteria discussed previously are as follows

- The proposed MSEE on buck-boost SECE architecture allows shrinking the external inductor without affecting power conversion efficiency. The multistage extraction can efficiently transfer the harvested energy over a relatively low-profile inductor (100 μ H-1 mH).
- The MSEE chip is adaptable to minimize power losses with the help of the multistage technique that does not require explicit calculation of extraction

time duration. Automatic Multistage generator provides maximum efficiency for wide range of input power.

- The circuit enhancements, which include a high accuracy peak detector and ultra-low power control, reduced minimum required input power that is significant improvement to extract power more efficiently from MEMS PEH with few microwatts of capacity and high excitation frequency compared to previous approaches.
- Implementation of the multistage generator with energy sensing method eliminates efficiency and cost limitations arising from high mechanical frequency, additional digital inputs and timing problems.
- Implementation of proposed power management circuit fastens the charging time of 47 μF output capacitance 2.5 times in comparison with only MSEE operation.

5.1.2 Optimal DSSH IC

A synchronized switching configuration, called “double synchronized switch harvesting”, with a MPPT circuit has been proposed and implemented to harvest maximal energy from ambient vibrations. The fabricated chip has following properties.

- The proposed synchronized switching configuration boosts extracted energy from PEHs, and provide load-independent energy extraction with a single inductor.
- Theoretical analysis indicates that optimum operation point of the proposed circuit is a function of Q factor of the charge inversion path. A novel MPP sensing approach is proposed, and implemented that achieves optimal point regardless of input excitation level for the first time in literature to the best of author’s knowledge.

- Implementation of robust charge flipping circuit secures optimal charge flipping time. Moreover, the low power design of building blocks provides efficient operation with wider range of excitation frequency and output voltage.
- The transferred power from the PEH is increased by up to 600% for the full storage voltage range of 1.8-3.7 V. The piezoelectric harvesting system harnesses 460% more power compared to an ideal full-bridge rectifier as PEH is excited at resonant frequency.
- DSSH IC can harvest energy efficiently from shock vibration, as system adjusts optimum operation point automatically regardless of the variation in the available energy on PEH. This property is valuable as shock vibrations are the most available energy source in real applications.

5.1.3 Hybrid Energy Harvesting System

A hybrid energy harvesting system has been presented to extract low and high frequency vibrations simultaneously through electromagnetic and piezoelectric harvesters. The aim of this study was to elaborate power capacity of energy harvesting system and evaluate it in real harvesting condition.

- Implementation of novel power management circuit based on charge investment approach boosts effective damping force of PEH and extracted power as well.
- The Hybrid IC provides a load independent structure for fast-charging single storage element with a wide range of output voltage from 1 V to 3.4 V.
- The circuit can handle minimum input power of 1 μ W. The system has a broad operation range between few μ Ws available from body motion to more than 100 μ W generated from high frequency excitations.
- The total harvested power from both harvesters is greater than the power obtained from each independently. The hybrid IC achieves with high power conversion efficiency from two energy sources at the same time.

- A wearable harvester prototype consisting of custom-made EM harvester, off-the-shelf PEH, and the Hybrid IC has been built for extracting energy from body movement. The harvesting system mounted on the wrist of a jogger can extract up to 20 μW for different output voltages.

5.2 Future Work

Although the presented ICs and related achievements further the development of energy harvesting systems and meanwhile are comparable with state-of-art, modifications and more studies could be done as well as presenting new topologies.

- The output voltage of MSEE IC is not regulated to specific value and is determined by the input power. Any buck-boost converter can be applied to put in desired voltage range for related application.
- DSSH IC is the most promising part in this research. The utilized power MOSFET switches have a large threshold voltage that leads to higher conduction losses in lower storage voltage. Therefore, the circuit can be designed and optimized within voltage and power range of the MEMS piezoelectric harvester to achieve higher performance. A similar PMC, used for the MSEE, can be also implemented for this method to fasten huge storage capacitance. Alternatively, an intermittent capacitance could be used to transfer harvested charge.
- The hybrid system can be enhanced to triple hybrid system by adding thermoelectric energy harvester. In this case, the investment process from both EMH and thermoelectric harvester will require an inductor to accumulate the harvested charges on piezoelectric capacitance efficiently. The inductor of the SECE can be shared to minimize volume and costs.
- **Proposing new topology:** MSEE and optimal DSSH techniques can provide load independent operation, and their performances in term of extracted power levels are superior to other SECE and SSHI techniques. Nevertheless, to obtain

higher efficiencies and high power extraction gains, these methods require external inductors in the range of 100 μH to 1mH. Therefore, we have proposed Synchronized Switch Harvesting on Capacitor Inductor (SSH-CI) technique to extract energy from MEMS PEHs. It benefits from two-step charge-inversion process over series of an inductor and a capacitor as well as similar structure to conventional SSHI method. The proposed circuit can achieve high power conversion efficiencies and power extraction enhancements with small inductance values in the range of a few tens of μH 's associated with a capacitor.

REFERENCES

- [1] R. J. M. Vullers, R. Schaijk, H. Visser, J. Penders, and C. Hoof, "Energy Harvesting for Autonomous Wireless Sensor Networks," *IEEE Solid-State Circuits Mag.*, vol. 2, no. 2, pp. 29–38, 2010.
- [2] M. K. Cosetti and S. B. Waltzman, "Cochlear implants: current status and future potential.," *Expert Rev. Med. Devices*, vol. 8, pp. 389–401, 2011.
- [3] J. Georgiou and C. Toumazou, "A 126 uW cochlear chip for a totally implantable system," *IEEE Journal of Solid-State Circuits*, vol. 40. pp. 430–443, 2005.
- [4] F. G. Zeng, S. Rebscher, W. Harrison, X. Sun, and H. Feng, "Cochlear implants: system design, integration, and evaluation.," *IEEE Rev. Biomed. Eng.*, vol. 1, pp. 115–142, 2008.
- [5] E. Gelenbe and C. Morfopoulou, "A framework for energy-aware routing in packet networks," *Comput. J.*, vol. 54, no. 6, pp. 850–859, 2011.
- [6] S. Roundy, P. Wright, J. Rabaey, and 2004, *Energy scavenging for wireless sensor networks: with special focus on vibrations*. 2004.
- [7] M. Stordeur and I. Stark, "Low Power Thermoelectric Generator - self-sufficient energy supply for micro systems," in *16th International Conference on Thermoelectrics*, 1997, pp. 575–577.
- [8] C. Alippi and C. Galperti, "An Adaptive System for Optimal Solar Energy Harvesting in Wireless Sensor Network Nodes," *IEEE Trans. Circuits Syst. I Regul. Pap.*, vol. 55, pp. 1742–1750, 2008.
- [9] M. Minami and T. Morito, "Solar biscuit: A battery-less wireless sensor network system for environmental monitoring applications," in *The 2nd*

International Workshop on Networked Sensing Systems, 2005.

- [10] R. E. Barnett, J. Liu, and S. Lazar, "A RF to DC Voltage Conversion Model for Multi-Stage Rectifiers in UHF RFID Transponders," *IEEE J. Solid-State Circuits*, vol. 44, no. 2, pp. 354–370, Feb. 2009.
- [11] S. Scorcioni, L. Larcher, A. Bertacchini, L. Vincetti, and M. Maini, "An integrated RF energy harvester for UHF wireless powering applications," in *2013 IEEE Wireless Power Transfer, WPT 2013*, 2013, pp. 92–95.
- [12] T. Sterken, P. Fiorini, K. Baert, R. Puers, and G. Borghs, "An electret-based electrostatic μ -generator," *TRANSDUCERS 2003 - 12th Int. Conf. Solid-State Sensors, Actuators Microsystems, Dig. Tech. Pap.*, vol. 2, no. July, pp. 1291–1294, 2003.
- [13] S. Roundy and P. K. Wright, "A piezoelectric vibration based generator for wireless electronics," *Smart Mater. Struct.*, vol. 13, pp. 1131–1142, 2004.
- [14] S. Roundy, P. K. Wright, and J. Rabaey, "A study of low level vibrations as a power source for wireless sensor nodes," *Comput. Commun.*, vol. 26, pp. 1131–1144, 2003.
- [15] K. Zhou, F. Xie, and Y. Tao, "Piezoelectric Energy Harvester for Wireless Sensors," Catholic University of Leuven, 2013.
- [16] A. Erturk and D. J. Inman, "*Piezoelectric energy harvesting*." Wiley, 2011.
- [17] S. Roundy, "On the Effectiveness of Vibration-based Energy Harvesting," *J. Intell. Mater. Syst. Struct.*, vol. 16, pp. 809–823, 2005.
- [18] E. E. Aktakka, "Integration of Bulk Piezoelectric Materials into Microsystems," *Ph.D Thesis*, University of Michigan, 2012.
- [19] J. Yick, B. Mukherjee, and D. Ghosal, "Wireless sensor network survey," *Comput. Networks*, vol. 52, no. 12, pp. 2292–2330, 2008.

- [20] A. Ghaffari, "An energy efficient routing protocol for wireless sensor networks using a-star algorithm," *J. Appl. Res. Technol.*, vol. 12, no. 4, pp. 815–822, 2014.
- [21] K. F. Navarro, E. Lawrence, and B. Lim, "Medical motecare: A distributed personal healthcare monitoring system," in *Proceedings - International Conference on eHealth, Telemedicine, and Social Medicine, eTELEMED 2009*, 2009, pp. 25–30.
- [22] Z. Zhong, T. Zhu, D. Wang, and T. He, "Tracking with unreliable node sequences," in *Proceedings - IEEE INFOCOM*, 2009, pp. 1215–1223.
- [23] F. Viani, P. Rocca, L. Lizzi, M. Rocca, G. Benedetti, and A. Massa, "WSN-based early alert system for preventing wildlife-vehicle collisions in Alps regions," in *Proceedings - 2011 IEEE-APS Topical Conference on Antennas and Propagation in Wireless Communications, APWC'11*, 2011, pp. 106–109.
- [24] S. Baghaee, S. Zubeyde Gurbuz, and E. Uysal-Biyikoglu, "Implementation of an enhanced target localization and identification algorithm on a magnetic WSN," *IEICE Trans. Commun.*, vol. E98B, no. 10, pp. 2022–2032, 2015.
- [25] S. Chamanian, H. Uluşan, Ö. Zorlu, S. Baghaee, E. Uysal-Biyikoglu, and H. Külah, "Wearable battery-less wireless sensor network with electromagnetic energy harvesting system," *Sensors Actuators A Phys.*, vol. 249, pp. 77–84, 2016.
- [26] S. Roundy, P. K. Wright, and J. Rabaey, "A study of low level vibrations as a power source for wireless sensor nodes," *Comput. Commun.*, vol. 26, no. 11, pp. 1131–1144, Jul. 2003.
- [27] P. P. Mercier, A. C. Lysaght, S. Bandyopadhyay, A. P. Chandrakasan, and K. M. Stankovic, "Energy extraction from the biologic battery in the inner ear," *Nat. Biotechnol.*, vol. 30, pp. 1240–3, 2012.
- [28] N. Mukherjee, R. D. Roseman, and J. P. Willging, "The piezoelectric cochlear

- implant: Concept, feasibility, challenges, and issues,” *J. Biomed. Mater. Res.*, vol. 53, pp. 181–187, 2000.
- [29] T. Inaoka *et al.*, “Piezoelectric materials mimic the function of the cochlear sensory epithelium,” *Proc. Natl. Acad. Sci.*, vol. 108, pp. 18390–18395, 2011.
 - [30] D. J. Young, M. a. Zurcher, W. H. Ko, M. Semaan, and C. a. Megerian, “Implantable MEMS Accelerometer Microphone for Cochlear Prosthesis,” *2007 IEEE Int. Symp. Circuits Syst.*, pp. 3119–3122, 2007.
 - [31] D. J. Young, M. a. Zurcher, M. Semaan, C. a. Megerian, and W. H. Ko, “MEMS capacitive accelerometer-based middle ear microphone,” *IEEE Trans. Biomed. Eng.*, vol. 59, pp. 3283–3292, 2012.
 - [32] L. Beker, O. Zorlu, N. Goksu, and H. Kulah, “Stimulating auditory nerve with MEMS harvesters for fully implantable and self-powered cochlear implants,” *2013 Transducers Eurosensors XXVII 17th Int. Conf. Solid-State Sensors, Actuators Microsystems, TRANSDUCERS EUROSENSORS 2013*, pp. 1663–1666, 2013.
 - [33] M. Yip, R. Jin, S. Member, H. H. Nakajima, K. M. Stankovic, and A. P. Chandrakasan, “A Fully-Implantable Cochlear Implant SoC With Piezoelectric Middle-Ear Sensor and Arbitrary Waveform Neural Stimulation,” *Solid-State Circuits*, vol. 50, no. 1, pp. 1–16, 2015.
 - [34] A. M. Flynn and S. R. Sanders, “Fundamental limits on energy transfer and circuit considerations for piezoelectric transformers,” *IEEE Trans. Power Electron.*, vol. 17, pp. 8–14, 2002.
 - [35] M. Renaud, “Piezoelectric energy harvesters for wireless sensors networks,” *Ph.D. Thesis*, Catholic University of Leuven, 2009.
 - [36] T. T. Le, J. Han, A. Von Jouanne, K. Mayaram, and T. S. Fiez, “Piezoelectric micro-power generation interface circuits,” *IEEE J. Solid-State Circuits*, vol. 41, pp. 1411–1419, 2006.

- [37] Y. Kushino and K. Koizumi, "Piezoelectric Energy Harvesting Circuit Using Full-Wave Voltage Doubler Rectifier and Switched Inductor," in *Energy Conversion Congress and Exposition (ECCE), 2014 IEEE*, 2014, pp. 2310–2315.
- [38] Y. Lam, W. Ki, and C. Tsui, "Integrated Low-Loss CMOS Active Rectifier for Wirelessly Powered Devices," *Simulation*, vol. 53, no. 12, pp. 1378–1382, 2006.
- [39] W. Jingmin, Y. Zheng, Z. Zhangming, and Y. Yintang, "An ultra-low-voltage rectifier for PE energy harvesting applications," *J. Semicond.*, vol. 37, no. 2, pp. 25004-1-25004-5, 2016.
- [40] N. Kong and D. S. Ha, "Low-power design of a self-powered piezoelectric energy harvesting system with maximum power point tracking," *IEEE Trans. Power Electron.*, vol. 27, no. 5, pp. 2298–2308, 2012.
- [41] M. Shim, S. Member, J. Kim, and S. Member, "Self-Powered 30 μ W to 10 mW Piezoelectric Energy Harvesting System With 9 . 09 ms / V Maximum Power Point Tracking Time," vol. 50, no. 10, pp. 2367–2379, 2015.
- [42] D. Guyomar, A. Badel, E. Lefeuvre, and C. Richard, "Toward energy harvesting using active materials and conversion improvement by nonlinear processing," *IEEE Trans. Ultrason. Ferroelectr. Freq. Control*, vol. 52, pp. 584–594, 2005.
- [43] S. Xu, K. D. T. Ngo, T. Nishida, G. B. Chung, and A. Sharma, "Low frequency pulsed resonant converter for energy harvesting," *IEEE Trans. Power Electron.*, vol. 22, pp. 63–68, 2007.
- [44] T. Hehn *et al.*, "A fully autonomous pulsed synchronous charge extractor for high-voltage piezoelectric harvesters," *Eur. Solid-State Circuits Conf.*, pp. 371–374, 2011.
- [45] A. Badel, D. Guyomar, E. Lefeuvre, and C. Richard, "Efficiency enhancement of a piezoelectric energy harvesting device in pulsed operation by synchronous

- charge inversion,” *J. Intell. Mater. Syst. Struct.*, vol. 16, no. 10, pp. 889–901, 2005.
- [46] E. Lefeuvre, “Piezoelectric Energy Harvesting Device Optimization by Synchronous Electric Charge Extraction,” *J. Intell. Mater. Syst. Struct.*, vol. 16, pp. 865–876, 2005.
- [47] E. Lefeuvre, a. Badel, C. Richard, L. Petit, and D. Guyomar, “A comparison between several vibration-powered piezoelectric generators for standalone systems,” *Sensors Actuators A Phys.*, vol. 126, no. 2, pp. 405–416, Feb. 2006.
- [48] P. Gasnier *et al.*, “An Autonomous Piezoelectric Energy Harvesting IC Based on a Synchronous Multi-Shot Technique,” *Solid-State Circuits*, vol. 49, no. 7, pp. 1561–1570, 2014.
- [49] L. Garbuio, M. Lallart, D. Guyomar, C. Richard, and D. Audigier, “Mechanical energy harvester with ultralow threshold rectification based on SSHI nonlinear technique,” *IEEE Trans. Ind. Electron.*, vol. 56, no. 4, pp. 1048–1056, 2009.
- [50] H. Shen, J. Qiu, H. Ji, K. Zhu, and M. Balsi, “Enhanced synchronized switch harvesting: A new energy harvesting scheme for efficient energy extraction,” *Smart Mater. Struct.*, vol. 19, no. 11, 2010.
- [51] L. Wu, X. D. Do, S. G. Lee, and D. S. Ha, “A Self-Powered and Optimal SSHI Circuit Integrated with an Active Rectifier for Piezoelectric Energy Harvesting,” *IEEE Trans. Circuits Syst. I Regul. Pap.*, vol. 64, no. 3, pp. 537–549, 2017.
- [52] M. Lallart, C. Richard, L. Garbuio, L. Petit, and D. Guyomar, “High efficiency, wide load bandwidth piezoelectric energy scavenging by a hybrid nonlinear approach,” *Sensors Actuators, A Phys.*, vol. 165, no. 2, pp. 294–302, 2011.
- [53] Y. K. Ramadass and A. P. Chandrakasan, “An efficient piezoelectric energy harvesting interface circuit using a bias-flip rectifier and shared inductor,” *IEEE J. Solid-State Circuits*, vol. 45, no. 1, pp. 189–204, 2010.

- [54] E. E. Aktakka and K. Najafi, "A micro inertial energy harvesting platform with self-supplied power management circuit for autonomous wireless sensor nodes," *IEEE J. Solid-State Circuits*, vol. 49, no. 9, pp. 2017–2029, 2014.
- [55] J. Dicken, P. D. Mitcheson, I. Stoianov, and E. M. Yeatman, "Increased Power Output from Piezoelectric Energy Harvester by Pre-Biasing," *In Proc. PowerMEMS*, vol. Washington, no. USA, pp. 75–78, 2009.
- [56] D. Kwon and G. A. Rincon-Mora, "A single-inductor 0.35 μm CMOS energy-investing piezoelectric harvester," *IEEE J. Solid-State Circuits*, vol. 49, no. 10, pp. 2277–2291, 2014.
- [57] R. Elfrink *et al.*, "Vacuum-packaged piezoelectric vibration energy harvesters: damping contributions and autonomy for a wireless sensor system," *J. Micromechanics Microengineering*, vol. 20, no. 10, p. 104001, 2010.
- [58] M. J. Hucker and C. Warsop, "Integrating bulk piezoelectric materials into MEMS for high authority actuators," *J. Micromechanics Microengineering*, vol. 17, no. 8, p. 1549, 2007.
- [59] S.-G. Kim, S. Priya, and I. Kanno, "Piezoelectric MEMS for energy harvesting," *MRS Bull.*, vol. 37, no. 11, pp. 1039–1050, 2012.
- [60] G. T. Hwang, M. Byun, C. K. Jeong, and K. J. Lee, "Flexible piezoelectric Thin-Film energy harvesters and nanosensors for biomedical applications," *Adv. Healthc. Mater.*, vol. 4, no. 5, pp. 646–658, 2015.
- [61] H. JP, A. JP, and R. Novak, "An outcomes study of cochlear implants in deaf patients: Audiologic, economic, and quality-of-life changes," *Arch. Otolaryngol. Neck Surg.*, vol. 121, no. 4, pp. 398–404, Apr. 1995.
- [62] T. Hehn *et al.*, "A Fully Autonomous Integrated Interface Circuit for Piezoelectric Harvesters," *IEEE J. Solid-State Circuits*, vol. 47, pp. 2185–2198, 2012.

- [63] M. Dini, A. Romani, M. Filippi, and M. Tartagni, "A Nanopower Synchronous Charge Extractor IC for Low-Voltage Piezoelectric Energy Harvesting with Residual Charge Inversion," *IEEE Trans. Power Electron.*, vol. 31, no. 2, pp. 1263–1274, 2016.
- [64] H. Uluşan, Ö. Zorlu, A. Muhtaroglu, and H. Kulah, "Highly Integrated 3 V Supply Electronics for Electromagnetic Energy Harvesters with Minimum 0.4 V_{peak} Input," *IEEE Trans. Ind. Electron.*, vol. 64, no. 7, pp. 5460–5467, 2017.
- [65] C. Peters, J. Handwerker, D. Maurath, and Y. Manoli, "A Sub-500 mV Highly Efficient Active Rectifier for Energy Harvesting Applications," *IEEE Trans. Circuits Syst. I Regul. Pap.*, vol. 58, no. 7, pp. 1542–1550, 2011.
- [66] A. Koyuncuoğlu *et al.*, "Bulk PZT Cantilever Based MEMS Acoustic Transducer for Cochlear Implant Applications," in *Multidisciplinary Digital Publishing Institute Proceedings*, 2017, vol. 1, no. 4, p. 584.
- [67] S. Chamanian, H. Uluşan, A. Koyuncuoğlu, A. Muhtaroglu, and H. Kulah, "An Adaptable Interface Circuit with Multi-Stage Energy Extraction for Low Power Piezoelectric Energy Harvesting MEMS," *IEEE Trans. Power Electron.*, vol. 8993, no. c, pp. 1–9, 2018.
- [68] D. A. Sanchez, J. Leicht, E. Jodka, E. Fazel, and Y. Manoli, "A 4µW-to-1mW parallel-SSHI rectifier for piezoelectric energy harvesting of periodic and shock excitations with inductor sharing, cold start-up and up to 681% power extraction improvement," *Dig. Tech. Pap. - IEEE Int. Solid-State Circuits Conf.*, vol. 59, pp. 366–367, 2016.
- [69] Y. Sang, X. Huang, H. Liu, and P. Jin, "A Vibration-Based Hybrid Energy Harvester for Wireless Sensor Systems," *IEEE Trans. Magn.*, vol. 48, no. 11, pp. 4495–4498, 2012.
- [70] H. Uluşan, S. Chamanian, W. P. M. R. Pathirana, Ö. Zorlu, A. Muhtaroglu, and H. Kulah, "A triple hybrid micropower generator with simultaneous multi-mode energy harvesting," *Smart Mater. Struct.*, vol. 27, no. 1, 2018.

- [71] R. Ambrosio and R. Torrealba, "Energy Harvesting Combining Three Different Sources for Low Power Applications," *IEEE Int. Conf. Electr. Eng. Comput. Sci. Autom. Control*, pp. 12–17, 2015.
- [72] N. J. Guilar, R. Amirtharajah, P. J. Hurst, and S. H. Lewis, "An Energy-Aware Multiple-Input Power Supply with Charge Recovery for Energy Harvesting Applications," *IEEE Int. Solid-State Circuits Conf.*, pp. 298–300, 2009.
- [73] J. Katic, S. Rodriguez, and A. Rusu, "A High-Efficiency Energy Harvesting Interface for Implanted Biofuel Cell and Thermal Harvesters," *IEEE Trans. Power Electron.*, vol. 33, no. 5, pp. 4125–4134, 2018.
- [74] S. Bandyopadhyay and A. P. Chandrakasan, "Platform Architecture for Solar, Thermal, and Vibration Energy Combining with MPPT and Single Inductor," *IEEE J. Solid-State Circuits*, vol. 47, no. 9, pp. 2199–2215, 2012.
- [75] S. Chamanian, H. Ulasan, A. Koyuncuoğlu, A. Muhtaroglu, and H. Kùlah, "An Adaptable Interface Circuit with Multi-Stage Energy Extraction for Low Power Piezoelectric Energy Harvesting MEMS," *IEEE Trans. Power Electron.*, 2018.

CURRICULUM VITAE

PERSONAL INFORMATION

Surname, Name: Chamaian, Salar
Nationality: Iranian
Date and Place of Birth: 22 Jun 1987, Ardebil
Marital Status: Married
Phone: +90 312 210 6086
email: salar.chamanian@metu.edu.tr

EDUCATION

Degree	Institution	Year of Graduation
Ph.D.	METU Electrical and Electronics Engineering	2018
MS	University of Tabriz Electrical and Electronics Engineering	2012
BS	University of Tabriz Electrical and Electronics Engineering	2009

WORK EXPERIENCE

Year	Place	Enrollment
2015-Present	METU ERC FLAMENCO Project	Research Assistant & IC designer
2013-2016	METU ERC E-CROPS Project	Research Assistant
2013-2014	METU MER	Research Assistant

FOREIGN LANGUAGES

Fluent English, Fluent Turkey, Persion (native language)

PUBLICATIONS

JOURNAL:

1. S. Chamanian, H. Uluşan, A. Koyuncuoğlu, A. Muhtaroglu, H. Kulah, "An Adaptable Interface Circuit with Multi-Stage Energy Extraction for Low Power Piezoelectric Energy Harvesting MEMS" *IEEE Trans. on Power Electronics*, 2018, Early Access: 10.1109/TPEL.2018.2841510.
2. S. Chamanian, A. Muhtaroglu, H. Kulah, "A self-adaptive and optimal DSSH rectifier for piezoelectric energy harvesting with up to 420 % power extraction improvement" submitted to *IEEE Trans. on Power Electronics*.
3. S. Chamanian, H. Uluşan, Ö. Zorlu, S. Baghaee, E. Uysal-Biyikoglu, and H. Kulah, "Wearable battery-less wireless sensor network with electromagnetic energy harvesting system," *Sensors Actuators A Phys.*, vol. 249, pp. 77–84, 2016.
4. S. Chamanian, S. Baghaee, H. Uluşan, O. Zorlu, H. Kulah, and E. Uysal-Biyikoglu, "Powering-up wireless sensor nodes utilizing rechargeable batteries and an electromagnetic vibration energy harvesting system," *Energies*, vol. 7, no. 10, 2014.
5. H. Uluşan, S. Chamanian, W. P. M. R. Pathirana, Ö. Zorlu, A. Muhtaroglu, and H. Kulah, "A triple hybrid micropower generator with simultaneous multi-mode energy harvesting," *Smart Mater. Struct.*, vol. 27, no. 1, 2018.
6. H. Uluşan, S. Chamanian, B. Ilik, A. Muhtaroglu, H. Kulah "Fully-Implantable Cochlear Implant Interface Electronics with 51.2 μ W Front-End Circuit" submitted to *IEEE Sensors Journal*.
8. S. Chamanian, H. Kulah, "Implementation of Energy-Neutral Operation on Vibration Energy Harvesting WSN", submitted to *IEEE Sensors Journal*.

CONFERENCE:

1. S. Chamanian, H. Uluşan, Ö. Zorlu, A. Muhtaroglu, and H. Kulah, "An Adaptable Interface Circuit for Low Power MEMS Piezoelectric Energy Harvesters with Multi- Stage Energy Extraction," in *Biomedical Circuits and Systems (BIOCAS)*, IEEE.
2. H. Uluşan, S. Chamanian, Ö. Zorlu, A. Muhtaroglu, and H. Kulah, "Neural Stimulation Interface with Ultra-Low Power Signal Conditioning Circuit for Fully-Implantable Cochlear Implants," *BioCAS 2017*, pp. 6–9, 2017.
3. S. Chamanian, Ö. Zorlu, H. Kulah, and A. Muhtaroglu, "An adaptive piezoelectric energy harvesting interface circuit with a novel peak detector," in *Energy Aware Computing Systems & Applications (ICEAC)*, 2015, 2015, pp. 1–4.
4. S. Chamanian, Ö. Zorlu, H. Kulah, and A. Muhtaroglu, "A self-powered integrated interface circuit for low power piezoelectric energy harvesters," in *2013 4th Annual International Conference on Energy Aware Computing Systems and Applications (ICEAC)*, 2013, pp. 45–49.
5. S.Chamanian, M.Bahrami, R.Pakdaman" Wideband capacitive Energy Harvester Based On Mechanical Frequency-Up Conversion" *2012 IEEE Sensors Applications Symposium*, Brescia, Italy, Feb 7-9, 2012, pp.6-9.
6. H. Uluşan, S. Chamanian, W. M. P. R. Pathirana, Ö. Zorlu, A. Muhtaroglu, and H. Kulah, "Triple Hybrid Energy Harvesting Interface Electronics," *J. Phys. Conf. Ser.*, vol. 773, no. 1, 2016.
7. S. Baghaee, S. Chamanian, H. Uluşan, O. Zorlu, E. Uysal-Biyikoglu, and H. Kulah, "Demonstration of energy-neutral operation on a WSN testbed using vibration energy harvesting," in *20th European Wireless Conference, EW 2014*, 2014.
8. A. Koyuncuoğlu, B.Ilik, S. Chamanian, "Bulk PZT Cantilever Based MEMS Acoustic Transducer for Cochlear Implant Applications," *Proceedings*, vol. 1, no. 4, p. 584, Aug. 2017.
9. B.Ilik, A. Koyuncuoğlu, H.Uluşan, S. Chamanian, D.Isik, O.S. Sukas and H. Kulah, "Bulk PZT Cantilever Based MEMS Acoustic Transducer for Cochlear Implant Applications," *Proceedings*, vol. 1, no. 4, p. 366, Aug. 2017.
10. M. R. Mousavi, S. Chamanian, I. Ahadzadeh, M. Bahrami, and M. G. Hosseini, "Fabrication and Simulation of Implantable Glucose Fuel Cell," *2011 21st Int. Conf. Syst. Eng.*, pp. 315–318, 2011.